ELECTRON TRANSPORT IN MICRO TO NANOSCALE SOLID STATE

NETWORKS

by

MATTHEW STETSON FAIRBANKS

A DISSERTATION

Presented to the Department of Physics
and the Graduate School of the University of Oregon
in partial fulfillment of the requirements
for the degree of
Doctor of Philosophy

March 2010

University of Oregon Graduate School

Confirmation of Approval and Acceptance of Dissertation prepared by:

Matthew Fairbanks

Title:

"Electron Transport in Micro to Nanoscale Solid State Networks"

This dissertation has been accepted and approved in partial fulfillment of the requirements for the degree in the Department of Physics by:

Jens Noeckel, Chairperson, Physics
Richard Taylor, Member, Physics
Heiner Linke, Member, Physics
David Strom, Member, Physics
James Hutchison, Outside Member, Chemistry

and Richard Linton, Vice President for Research and Graduate Studies/Dean of the Graduate School for the University of Oregon.

March 20, 2010

Original approval signatures are on file with the Graduate School and the University of Oregon Libraries.

An Abstract of the Dissertation of

Matthew Stetson Fairbanks   for the degree of   Doctor of Philosophy

in the Department of Physics   to be taken   March 2010

Title: ELECTRON TRANSPORT IN MICRO TO NANOSCALE SOLID

STATE NETWORKS

Approved: _____

Dr. Richard P. Taylor

This dissertation focuses on low-dimensional electron transport phenomena in devices ranging from semiconductor electron 'billiards' to semimetal atomic clusters to gold nanoparticles. In each material system, the goal of this research is to understand how carrier transport occurs when many elements act in concert. In the semiconductor electron billiards, magnetoconductance fluctuations, the result of electron quantum interference within the device, are used as a probe of electron transport through arrays of one, two, and three connected billiards. By combining two established analysis techniques, this research demonstrates a novel method for determining the quantum energy level spacing in each of the arrays. That information in turn shows the extent (and limits) of the phase-coherent electron wavefunction in each of the devices. The use of the following two material systems, the semimetal atomic clusters and the gold

nanoparticles, is inspired by the electron billiard results. First, the *output* of the simple, rectangular electron billiards, the magnetoconductance fluctuations, is quite generally found to be fractal. This research addresses the question of what output one might expect from a device with manifestly *fractal* geometry by simulating the electrical response of fractal resistor networks and by outlining a method to implement such devices in fractal aggregates of semimetal atomic clusters. Second, in gold nanoparticle arrays, the number of array elements can increase by orders of magnitude over the billiard arrays, all with the potential to stay in a similar, phase-coherent transport regime. The last portion of this dissertation details the fabrication of these nanoparticle-based devices and their electrical characteristics, which exhibit strong evidence for electron transport in the Coulomb-blockade regime. A sketch for further 'off-blockade' experiments to realize magnetoconductance fluctuations, i.e. phase-coherent electron phenomena, is presented.

CURRICULUM VITAE

NAME OF AUTHOR: Matthew Stetson Fairbanks

PLACE OF BIRTH: Oberlin, Ohio

DATE OF BIRTH: July 9, 1981

GRADUATE AND UNDERGRADUATE SCHOOLS ATTENDED:

    University of Oregon, Eugene, Oregon
    Oberlin College, Oberlin, Ohio

DEGREES AWARDED:

    Doctor of Philosophy in Physics, 2010, University of Oregon
    Master of Science in Physics, 2007, University of Oregon
    Bachelor of Arts in Physics, 2003, Oberlin College

AREAS OF SPECIAL INTEREST:

    Electron Transport in Solid State Devices
    Coherent Phenomena in Low Dimensional Electronics

PROFESSIONAL EXPERIENCE:

    Graduate Research Assistant, University of Oregon, 2005 – 2009
    Graduate Teaching Fellow, University of Oregon, 2003 – 2005

GRANTS, AWARDS AND HONORS:

    NSF Integrative Graduate Education and Research Traineeship, University of Oregon, 9/2009 to 12/2009

NSF Integrative Graduate Education and Research Traineeship, University of Oregon, 9/2008 to 8/2009

PUBLICATIONS:

M. S. Fairbanks and R. P. Taylor, "Measuring the scaling properties of temporal and spatial patterns: from the human eye to the wandering albatross," to be published in *Nonlinear Dynamical Systems Analysis for the Behavorial Sciences Using Real Data*, edited by R. Gregson and S. Guastello. Taylor & Francis, New York, 2010.

M. S. Fairbanks, T. P. Martin, B. C. Scannell, C. A. Marlow, H. Linke, and R. P. Taylor, "Measuring hybridization in GaInAs/InP electron billiards arrays," Proceedings of the 18th Conference on Electronic Properties of 2-D Systems (EP2DS-18), Physica E **42**, 1205 (2010).

T. P. Martin, M. S. Fairbanks, C. A. Marlow, B. C. Scannell, H. Linke, and R. P. Taylor, "Investigation of electron wave function hybridization in $Ga_{0.25}In_{0.75}As/InP$ arrays," Applied Physics Letters **95**, 182105 (2009).

M. S. Fairbanks, D. McCarthy, R. P. Taylor, and S. A. Brown, "Fractal electronic circuits assembled from nanoclusters," Proceedings of AMN-4 in the AIP Conference Proceedings Series **1151**, 63 - 66 (2009).

T. P. Martin, C. A. Marlow, B. C. Scannell, M. S. Fairbanks, H. Linke, S. A. Brown, and R. P. Taylor, "Chaotic scattering in nano-electronic systems: from billiards to clusters," International Journal of Nanotechnology **6**, 408 (2009).

M. S. Fairbanks, C. A. Marlow, R. P. Taylor, and H. Linke, "Nonlinear characteristics in the magnetoconductance of electron billiards," Proceedings of AMN-3 in Current Applied Physics **8**, 340-342 (2008).

B. C. Scannell, T. P. Martin, M. S. Fairbanks, H. Linke, C. A. Marlow, T. M. Fromhold, C. V. Brown, K. Ishibashi, and R. P. Taylor, "Quantum conductance fluctuations in semiconductor devices," Proceedings of AMN-3 in Current Applied Physics **8**, 332-335 (2008).

R. P. Taylor, R. Guzman, T. P. Martin, G. D. R. Hall, A. P. Micolich, D. Jonas, B. C. Scannell, M. S. Fairbanks, C. A. Marlow. "Authenticating Pollock paintings using fractal geometry," Pattern Recognition Letters **28**, 695 (2007).

C. A. Marlow, R. P. Taylor, T. P. Martin, B. C. Scannell, H. Linke, M. S. Fairbanks, G. D. R. Hall, I. Shorubalko, L. Samuelson, T. M. Fromhold, C. V. Brown, B. Hackens, S. Faniel, C. Gustin, V. Bayot, X. Wallart, S. Bollaert and A. Cappy. "Unified model of fractal conductance fluctuations for diffusive and ballistic semiconductor devices," Physical Review B **73**, 195318 (2006).

C. A. Marlow, R. P. Taylor, M. Fairbanks, I. Shorubalko, and H. Linke. "Experimental Investigation of the Breakdown of the Onsager-Casimir Relations," Physical Review Letters **96**, 116801 (2006).

ACKNOWLEDGEMENTS

Since beginning my graduate work a little more than six years hence, there have been many people who have helped me, directly or indirectly, complete the research contained in this dissertation. Primary among these is my advisor, Dr. Richard Taylor. His direction and expertise were integral to the research I conducted, and the breadth of his interests allowed me to learn a great deal more than I might have otherwise. For those things, and too many others to detail here, I will always owe him a debt of gratitude.

My labmates, former and current, have all helped me along the way. Ted and Colleen showed me early on what life in the Taylor Lab was like, set two very different yet equally good examples of how to conduct research as a graduate student, and taught me many of the techniques that helped me complete my research years after they were gone. My (near) contemporary, Billy, has been a good friend and an excellent research collaborator over the last few years. His off-color jokes and willingness to stick around late at night and curse the experiment into submission were much appreciated. Thanks to Eric (Linke Lab), who was always willing to share a Labview program, a bit of advice, and some time proofreading this dissertation. Thanks also to the other Linke Lab member who lived in the basement with us, Jason, for advice on lithography and the electron microscope.

Around the department(s), I'd first like to acknowledge my committee, Jens, Heiner, David, and Jim, for their questions, advice, and feedback both on this document and during my oral exam. Thanks in particular to Jim and members of his lab (Greg, Tatiana, and John) for working with me on the nanoparticle arrays research project. And though their practical contributions to this dissertation were in most cases small, my physicist friends around the department are the reason I've made it through six years and several months of graduate school. Many thanks to you, and I wish you all the best for the future.

My Mom and Dad deserve recognition for their support throughout my education: from the funding of my undergraduate degree, to not blinking an eye when I decided to wander off to the West Coast for graduate school, to not wondering aloud when I might be finishing this dissertation. For all of that and lots more, thank you. Thanks to Brianna, for your support through all the ups and downs of my physics education. Thanks also to Pat and Cherie, who have always been very supportive of their daughter's boyfriend/fiance/husband through my graduate experience. A fine pair of in-laws, you are.

Lastly, I'd like to recognize my grandparents for their advice, their perspective, and their example.

For my loving and very understanding wife, Brianna.

TABLE OF CONTENTS

LIST OF FIGURES

CHAPTER I

INTRODUCTION

Electronic devices have become very complex. This ranges from the staggering feats of engineering inherent in present day integrated circuits, to quantum computing with coherent carriers in quantum dots, to frustrated electron systems like single electron transistors. The breadth and depth of the field is fascinating and continues to expand. The goal, technologically speaking, of all this complexity is to either make individual devices smaller, thus packing more and more computing power into smaller and smaller footprints, or to make devices with more functions or novel functionality. This dissertation addresses these goals (in some small part) by focusing on low-dimensional electron transport phenomena in three different electronic device types: semiconductor electron 'billiard' arrays in high mobility heterostructures, fractal semimetal cluster aggregates, and gold nanoparticle-DNA complexes. In some ways these three systems are quite different, primarily in their appearance (see Figure 1.1). Each has a distinct fabrication process. The physical models for carrier transport in each system, though similar in basis, are also quite distinct. This dissertation details these differences, but it should become clear to the reader that, in fact, there is much that links these three systems, both thematically and physically.

At the broadest level, this research is united by the goal of understanding how
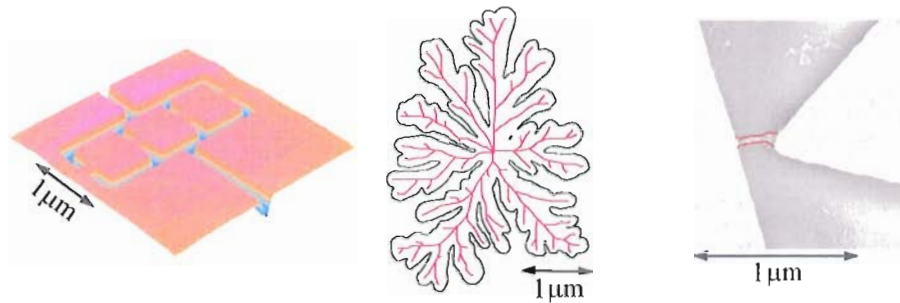
Figure 1.1. Examples of the three material systems studied in this dissertation: an atomic force microscope (AFM) image of an electron billiard array in a semiconductor heterostructure (a), the outline and backbone of a semimetal cluster aggregate (b), and a scanning electron microscope (SEM) image of a nanoparticle-DNA array (highlighted, c).

carrier transport occurs when multiple elements act in concert. This ranges from the few element limit, where device and material control is very precise (i.e. the electron billiard system), to the many element limit where the behaviors of individual elements are superceded by collective behavior (cluster aggregates and nanoparticles). More specifically, each of the latter variety was inspired by particular aspects of the electron billiard research. These connections are outlined along with the structure of this dissertation below.

Chapter II contains a brief overview of the apparatus used for the experiments described in Chapters III and V.

Chapter III details experiments on the semiconductor electron billiard devices. The goal of this research was to study and quantify changes in coherent electron

phenomena as the number of elements was changed in linear arrays of electron billiards. We study devices with one, two, and three electron billiards connected in series. Our probe in this study was magnetoconductance fluctuations (MCF), which are the result of electron quantum interference within the billiards, and are thus particularly sensitive to changes in the dynamics and coherence of electrons moving through the arrays. Combining two established techniques for analyzing the MCF, we were able to demonstrate a novel method for charting the quantum energy level spacing in each of the devices as the coupling between individual elements was changed. This in turn yields information about the extent and limits of the electron wavefunction as it hybridizes over multiple elements.

Chapter IV will explore the potential for novel, complex functionalities in electronic circuits that are *fractal* in their geometry. In short, a fractal is a structure that has an identical appearance (statistically or exactly) over a range of magnifications. They can be found in many places: mathematics, art, technology, and most widely in nature, a fact asserted by Mandelbrot's *The Fractal Geometry of Nature* [1] and titularly expanded upon (perhaps a bit enthusiastically) by Barnsley's *Fractals Everywhere* [2].

Research into the statistical qualities of electron billiards' MCF has come to the conclusion that they are indeed fractal over a wide range of experimental and material systems [3, 4]. Our current research has revealed a strong candidate for

the mechanism of this 'universal' behavior [5], namely the distribution of small-angle scatterers in the 2-dimensional electron gas (2DEG) induced by remote donor ion potentials. Repeated coherent deflections from these potentials produce the requisite mixed-phase-space carrier dynamics [6] for observing fractal conductance fluctuations. Having established fractal behavior in the output of a nominally Euclidean device, the electron billiard, an interesting question is: what functionality might we be able to produce when the device itself has a fractal geometry? To begin to answer that question, this chapter presents electrical simulations of fractal resistor networks along with a proposal for implementation of these devices in the form of diffusion-limited aggregates of semimetal atomic clusters.

Chapter V details the construction and measurement of Au nanoparticle arrays, a project done in collaboration with Professor Jim Hutchison's lab at the University of Oregon. This collaboration grew out of a proposal to extend our studies of electron billiard arrays to arrays of nanoparticles that can be close-packed along DNA molecules, creating arrays with tens, hundreds, or even thousands of elements depending on the size of the nanoparticles and the length of the DNA sections.

The expectation that these two systems are analogous is based largely on their shared geometric features (linear, connected arrays of conducting elements) and rough calculations indicating that the phase-coherence-length to length-of-array and Fermi-wavelength to array-element-size ratios were similar, i.e. we could expect coherent

electron transport across the nanoparticle array, and the energy level spacings of a single nanoparticle would be of similar magnitude to the billiard's in relation to $k_B T$, the so-called 'mesoscopic' transport regime. With these characteristics, MCF may be observable in the nanoparticle arrays at low temperatures and provide a great deal of information about how electrons move through this novel nanoscale system.

However, in practice there are a number of challenges that must be addressed before MCF can be used to probe carrier dynamics in these arrays. For instance, the electrical characteristics of our first generation devices exhibit strong evidence for Coulomb blockade transport, which is quite distinct from our normal mode of operation in the electron billiards (though very similar to a situation where the billiard entrance and exit are replaced with tunnel barriers). It is interesting in its own right, since Coulomb blockade in arrays is still a topic of active research interest [7–10]. Our electrical measurements in this regime, device fabrication details, and an outline for further 'off-blockade' experiments to possibly realize MCF in these novel devices are all presented in Chapter V.

CHAPTER II

MEASUREMENT APPARATUS AND TECHNIQUES

Introduction

This chapter provides a brief overview of the experimental apparatus used to study the electron billiard arrays and nanoparticle arrays detailed in Chapters III and V respectively. The material presented here does not delve into the many details of instrument operation that any subsequent user will need to understand for many hours of (relatively) trouble-free experimenting. For such information, the reader should refer to the manuals and instructions on file with the instrumentation.

Cryostat Operation and Characteristics

Overview

For measurements of both the electron billiard and nanoparticle arrays, it is important to maintain precise control of the device temperature *and* reach temperatures at or below that of liquid ^{4}He (4.2 K). Another fundamental requirement is the ability to tune the electromagnetic environment of the devices during measurements.

A standard solution to these requirements is the use of a liquid helium cryostat in combination with a superconducting solenoid. The Taylor/Linke lab possesses two of these systems, one from Oxford Instruments and another, newer system from Janis. The measurements performed in the course of this dissertation made use of the Oxford Instruments cryostat. This system consists of a ^{3}He Heliox-VL insert and a liquid nitrogen jacketed dewar with an 8 Tesla (9 T with the λ-plate system) superconducting solenoid mounted near its bottom. This instrument can access magnetic fields of ± 9 T with 0.1 mT resolution and temperatures down to 230 mK and upwards of 100 K. Given these capabilities, the ^{3}He cryostat can be a versatile and powerful tool for experimental investigations involving temperature or field dependent phenomena in solid state systems. The following two subsections offer operational details pertinent to this dissertation.

System Architecture

The system architecture for the Oxford insert and dewar is shown in Figure 2.1. The liquid helium dewar is liquid nitrogen-jacketed and contains an 8 T superconducting solenoid for tuning the magnetic field perpendicular to the plane of a device mounted parallel to the end of the cryostat insert. Electrical connections feed up through the interior of the inserts from the device mount, and can be connected to instrumentation exterior to the cryostat via a multi-pin interface at the top of the insert.
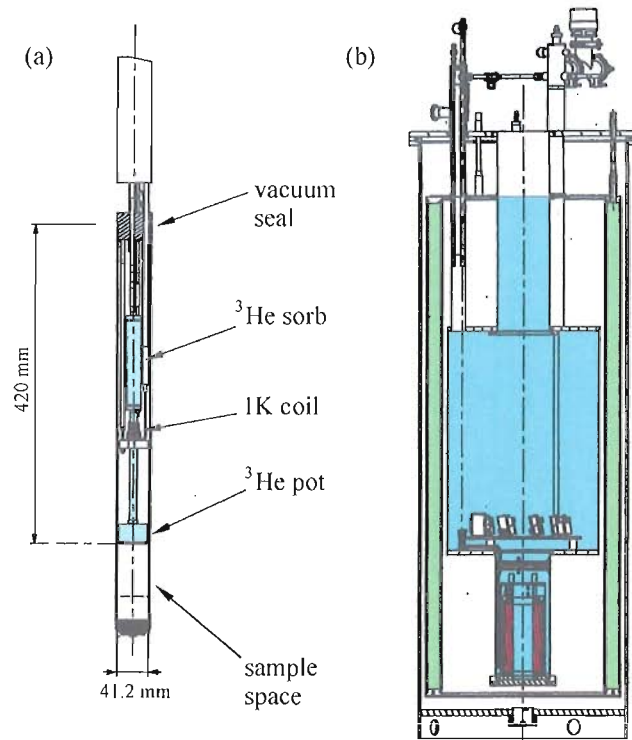
Figure 2.1. Manufacturer schematics for the end of the ^{3}He insert (a) and surrounding dewar (b). Shaded components in (a) indicate the sealed ^{3}He cell position. In (b), green, blue, and red shadings indicate the liquid nitrogen shielding, liquid helium tank, and the superconducting solenoid respectively.

The cryostat is 'sample in vacuum', which makes sample switching a relatively long (≈ 2 hour minimum) process, but allows a more inert sample environment and cooling below ≈ 1.6 K. Base temperature is achieved by cooling the liquid helium (^{4}He) drawn up into the 1 K coil by mechanical pumping and outgassing (by heating to ≈ 30 K) the sorption pump inside the ^{3}He cell, freeing ^{3}He gas. Pumped helium will drop the temperature inside the sealed cell to ^{3}He's condensation point. Once the ^{3}He gas is completely condensed to liquid, the sorption pump temperature is allowed to drop. The sorption pump will slowly reduce the pressure in the cell, thus lowering

the liquid's temperature. The ^{3}He pot and the attached sample will then drop to its base temperature value.

<p style="text-align:center">Temperature Control</p>

As stated previously, the base temperature for the Oxford cryostat is 230 mK. This temperature can be routinely achieved and stably maintained for long periods of time: several days for the Oxford cryostat. This limit stems from the need to recondense the ^{3}He inside the Oxford insert, which requires warming the sample to ≈ 2 K for a few hours. In the case of the electron billiard devices (Chapter III), the longest continuous period of static temperature needed is ≈ 8 hours (one full length data set). Also, the devices' electrical characteristics are the same before and after a cycle up to 2 K, so experiments can continue as long as needed.

For the experiments on nanoparticle-based devices (Chapter V),any single data set can be collected in as little as 15 minutes. Though some care must be taken to ensure thermal equilibrium between the location of the thermometer and the device prior to measurement, in practice temperature stability is still only required on the hour time scale. The temperatures for our experiments (from base to ≈ 80 K) are easy to achieve and maintain over that time scale. Higher temperatures (> 100 K) are achievable and still have a high degree of stability, but require increasingly long heating and cooling cycles. For the nanoparticle devices, where we were initially unsure regarding their stability over such times, these temperatures were largely

avoided. Future investigations of temperature dependent effects in the nanoparticle devices may take advantage of a newly commissioned Janis cryostat in the lab, which has a higher base temperature (≈ 1.6 K), but temperature control response times on the order of seconds and even higher temperature stabilities.

Electrical Measurement Tools and Techniques

Electron Billiard Measurement

The electron billiards discussed in Chapter III generally have resistances ~ 10 kΩ, and only small contributions to their impedance from capacitance and inductance. This relatively low electrical impedance allows 4 point device measurements using the circuit shown in Figure 2.2. A constant excitation current of 1 nA at 37 Hz is applied to the device via a lock-in amplifier output channel (Figure 2.2(c)). Typically this is accomplished with a 0.1 V signal at the output over the circuit resistance, which is maintained at 100 MΩ via a ballast resistor. This level of current maintains a relatively large signal-to-noise ratio ($\gtrsim 100 : 1$) while avoiding electron heating effects in the device ($eV_{bias} \leq k_B T$). The voltage drop across the 10 kΩ resistor monitors the current in the circuit, just to be certain. Two other lock-ins monitor the device (Figure 2.2(a)), and a portion of the empty Hall bar channel (Figure 2.2(c)). The latter measures the longitudinal resistance (R_{xx}) of the channel, which can be translated into a carrier density from its R_{xx} vs. magnetic field dependence [11]. An
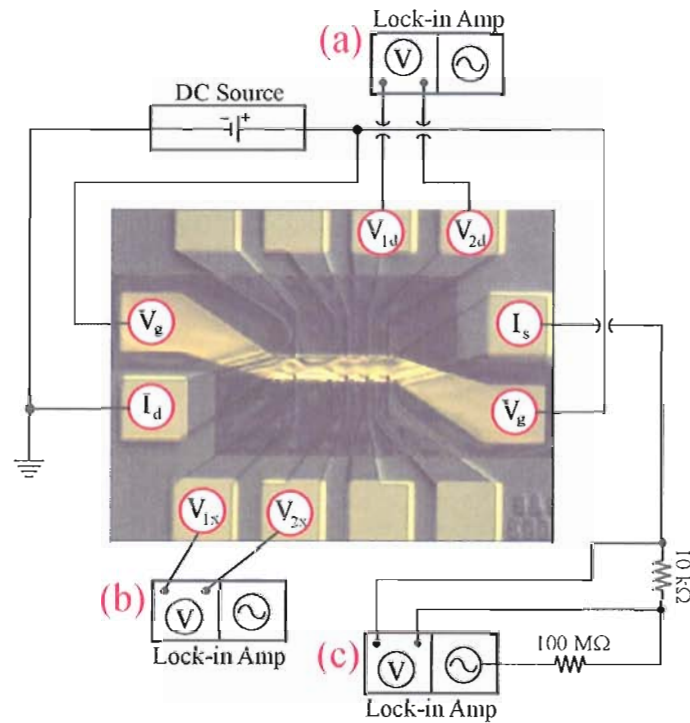
Figure 2.2. A schematic of the electrical measurement circuit for the electron billiard experiments. The labeling details the purpose of each instrument (see text). At the center is an optical microscope image of a Hall bar mesa.

alternate configuration for measuring carrier density might instead monitor the Hall resistance using leads directly across from one another in the channel [12].

For reference, the specific instruments used for the experiments detailed in Chapter III are: Stanford Research Systems (SRS) SR830 lock-in amplifiers and an IoTech DAC 488HR/4 digital-to-analog converter for the DC source.

Nanoparticle Array Measurement

The nanoparticle arrays discussed in Chapter V are measured using the DC circuit pictured in Figure 2.3. AC measurements like those applied to the electron billiard
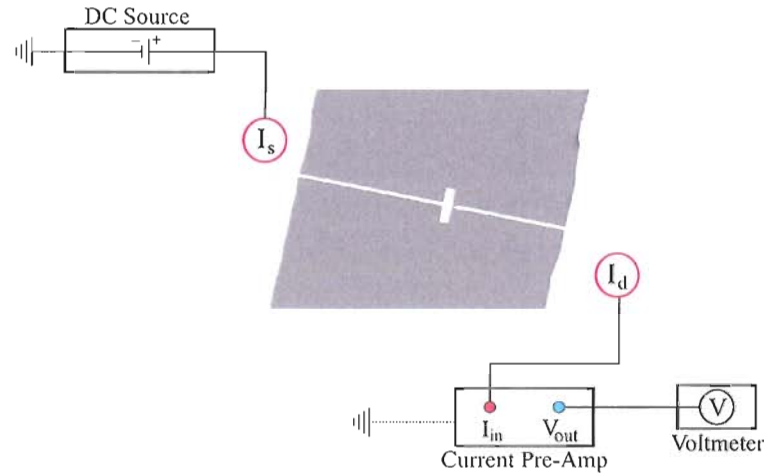
Figure 2.3. A schematic of the DC electrical measurement circuit for the nanoparticle-based devices. At the center is an SEM image of a single pair of the electrodes used to contact the nanoparticle array.

are made more difficult by the nanoparticle arrays' high impedances, typically at least on the order of 10 GΩ's. This makes 4 point voltage detection difficult (noting that SR830 lock-in amplifiers have 10 MΩ input impedances). Fortunately there is a great deal of information available using simple DC measurements of the nanoparticle arrays. Eliminating lead resistances, the advantage of 4 point detection, is also much less important given the massive resistance of the device. Sourcing voltage, current through the circuit is monitored via a high sensitivity voltmeter after passing through a current pre-amplifier. Despite the absence of lock-in detection, current noise is only ≈ 0.2 pA at the cryostat's base temperature.

For reference, the specific instruments used for the experiments detailed in Chapter V are a Yokogawa 7651 DC source, an SRS SR570 low noise current pre-amplifier, and a Keithley multimeter (2000 model).

CHAPTER III

COHERENT TRANSPORT IN ELECTRON BILLIARD ARRAYS

Introduction

The coupling of quantum electronic devices to form arrays is of considerable interest for both fundamental physics (e.g. quantum coherence [13, 14]) and applied physics (e.g. spintronics and quantum computing [14–17]). From an engineering viewpoint, understanding the interaction of individual devices represents the first step for developing circuits with sophisticated quantum functionality. The majority of previous coherent coupling research has focused on electron transport mediated by tunneling between 'closed' electron billiards or quantum dots [13, 14, 17–22]. The experiments detailed in this chapter focus on the 'open' transport regime where the devices are connected by conducting channels [23–25]. Our experiments and subsequent analyses have lead to a novel measurement technique for quantifying the evolution of the quantum energy level spectrum of the open electron billiard arrays as the coupling strength of the connecting channels is varied and the number of devices in the array, $N_{billiard}$, is increased. The technique employs magnetoconductance fluctuations to probe the decrease in the average spacing of the quantum energy levels as the electron wavefunctions hybridize between billiards in the array. Our

method is relatively flexible compared to previous spectroscopy techniques, in that it does not require microwave radiation [13, 18], nor is it restricted to probing dots $\lesssim 0.2$ $\mu\mathrm{m}^2$ in area [26]. To demonstrate the technique, we[1] investigate arrays of electron billiards etched into a modulation-doped GaInAs/InP heterostructure [27]. The $\mathrm{Ga}_x\mathrm{In}_{1-x}\mathrm{As}$ material system is increasingly employed for studies of quantum transport phenomena, such as quantum coherence [28] and engineered conductance asymmetry, [23] rather than the traditional $\mathrm{Al}_x\mathrm{Ga}_{1-x}\mathrm{As}/\mathrm{GaAs}$ heterostructures [24, 25].

This chapter will begin with a short review of the physics relevant to this experiment, give some fabrication details for these electron billiard arrays, and finish by detailing the results of our experiment and analyses.

Quantum Interference in Electron Billiards

This section will attempt the cover the requisite physics and material science background for our experiment. There is a great deal that could be included, but to retain focus, descriptions will remain brief. The reader is referred to a number of excellent reviews [29–31] and texts [32–34] on this subject for further information.

---

[1]The plural pronoun is used to reflect the contributions of other researchers in addition to the author of this dissertation. The project was completed primarily in collaboration with Dr. Theodore Martin (PhD, University of Oregon, 2006), currently of the Naval Research Laboratory. Other contributors are noted in the text.

Two-Dimensional Transport and Electron Billiards

Two-dimensional electron gases (2DEGs) in semiconducting materials combine a variety of properties that make them ideal for studying quantum electron transport phenomena. Carrier densities are relatively low ($\sim 1 \times 10^{11}/\text{cm}^2$) and are easily modulated by an electric field, because of the large screening length. The low density also results in a relatively large Fermi wavelength λ_F, (~ 40 nm), which is approximately the minimum size of the devices that can be fabricated in these materials. Additionally, the reduced dimensionality of the system simplifies the physics[2] of carrier motion and the Fermi surface, which becomes circular.

2DEGs can be formed in a variety of material systems, but conceptually the mechanism is the same in each case. Electrons are confined to a quantum well at the interface between two materials of differing bandgap. Transport parallel to the interface is unimpeded, however the confinement perpendicular to the interface quantizes the allowed energies of the electrons such that only a single level is populated, creating (ideally) a 2D plane of electrons.

Interestingly, some of the first 2DEG research was done on the surface of liquid helium [35]. However, numerous experiments on the 2DEGs formed in the inversion layer of Si MOSFETs [36] set the foundation of the field. More recently (since the advent of modulation doping [37]), the canonical research system for creating 2DEGs has been $Al_xGa_{1-x}As/GaAs$ on account of its superior electron mobility, which eases

---

[2]Said one way - enough for detailed theoretical treatment, but not so much that experiments are boring.
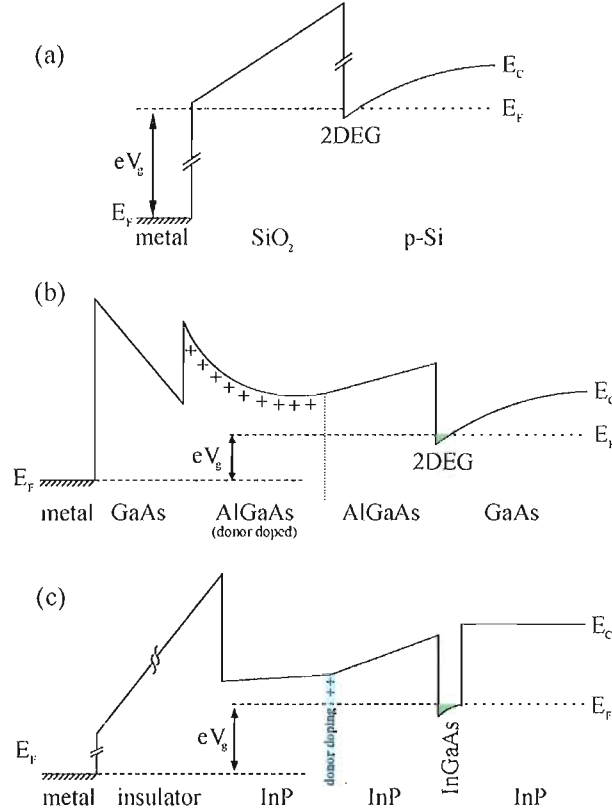
Figure 3.1. Schematic band structures of an Si inversion layer 2DEG (a), the $Al_xGa_{1-x}As/GaAs$ heterostructure (b), and the $In_{0.25}Ga_{0.75}As/InP$ heterostructure (c).

the observation of quantum coherent phenomena and has significant technological advantages as well. For comparison, the heterostructures that create 2DEGs in Si and $Al_xGa_{1-x}As/GaAs$ are shown in Figure 3.1(a,b).

The high mobility of $Al_xGa_{1-x}As/GaAs$ is the result of several factors: 1) epitaxial growth techniques (molecular beam epitaxy, metal-organic vapor phase epitaxy, etc) produce crystalline layers with very few defects, 2) $Al_xGa_{1-x}As$ and GaAs have well-matched lattice constants for most x, dramatically reducing boundary scattering, 3) GaAs has a direct bandgap with a single conduction band minimum, removing

intervalley scattering effects, 4) electrons in GaAs have a low effective mass ($0.067\,m_e$). The same factors are present in $In_{0.25}Ga_{0.75}As/InP$, the high mobility material system selected for the experiments performed in the course of this dissertation. Its band structure is shown in Figure 3.1(c). Further details about this heterostructure can be found in the "Fabrication" subsection below and in [38, 39].

Electron billiards are created by further confining the 2DEG using biased surface gates or etching[3]. Each method is shown schematically in Figure 3.2 (in cross-sections and top-down). Negatively biased surface gates electrostatically deplete the 2DEG beneath them, causing the device shape to roughly mirror that of the surface gates (Figure 3.2(a)). Etching physically removes portions of the 2DEG to create the desired device (Figure 3.2(b)). Though this technique sacrifices some flexibility (for instance, surface gates can be grounded to remove portions of the device design), it generally allows for more precision in defining device shape. Typically, the billiard is defined in a Hall bar, which allows 4 point electrical measurements of the billiard itself as well as measurements (using the Hall and Shubnikov - de Haas effects) to determine carrier mobility, effective mass, and other key material properties. A typical measurement configuration is shown in Figure 2.2.

The term electron 'billiard' comes from an analogy between the electrons moving through the device and balls moving across a table. This analogy works, because of

---

[3]Though dry etching techniques can be used, more common are chemical etching techniques that create smooth, relatively defect-free surfaces.
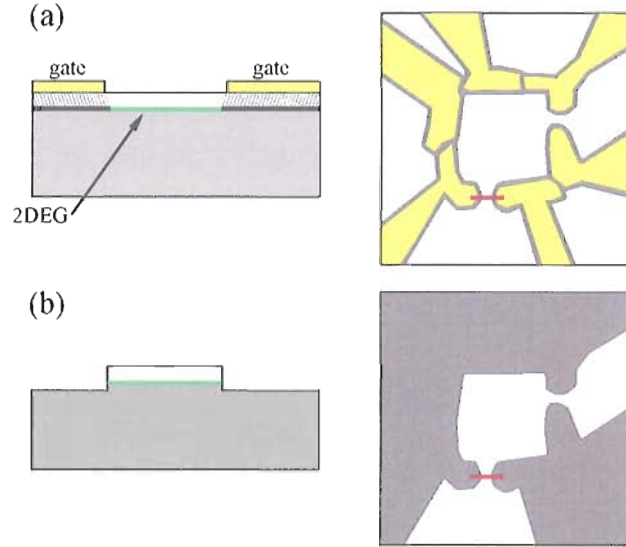
Figure 3.2. Schematics of the surface gate (a) and etching (b) methods for device definition. On the left are cross-sections of the heterostructures. On the right are top-down views for each method. The positions of the cross-sections are indicated in red.

the material's extremely low defect density in the 2DEG plane, such that electrons can be thought of as moving ballistically within the device. The term "ballistic" transport is traditionally applied to systems where the device dimensions $(W, L) < l$, the mean free path (see Figure 3.3(a)), which is in sharp contrast to the more familiar, Drude-type diffusive regime (Figure 3.3(b)) where $(W, L) \gg l$. It is important to note that the billiard model of the electron leaves out the quantum nature of the device. Since λ_F is comparable to the typical electron billiard's linear dimension (~ 40 nm compared to 1 μm), there is quantization of the electron energies in the device with spacings $\Delta E_S \sim 10$ μeV $\ll E_F$. For this reason, "electron billiard" is commonly replaced with "quantum dot", which implies a 0D quantum system. However, for our experiments, $\Delta E_S \sim k_B T$, so we retain the 2D picture.
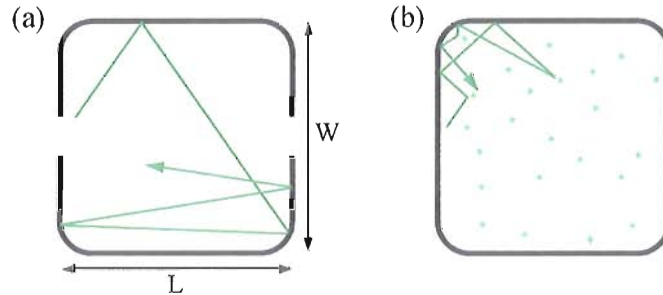
Figure 3.3. Schematics of the ballistic (a) and diffusive (b) carrier transport regimes. The asterisk-like objects in (b) represent crystalline defects.

Ballistic transport results in a wide variety of unique phenomena [29, 31], however there are two items of primary importance to the research presented in this chapter. First is the presence of a classically chaotic electron trajectory distribution in our electron billiards. The quantum manifestations of this classical behavior are well-described by *random matrix theory* [30, 40], whose predictions are key to our method. Second is the preservation of 'skipping' orbits in the high magnetic field regime. Analysis of the quantum interference between these special electron trajectories can quantify how long electrons will remain in the same quantum mechanical state, i.e. remain phase-coherent. Given that our research depends on charting quantum interference effects, the extent of electron phase coherence is a crucial parameter.

Magnetoconductance Fluctuations

Though there are many phase coherent phenomena in 2DEG devices, the primary tool for our electron billiard research is *magnetoconductance fluctuations*. In a time-varying magnetic field applied perpendicular to the 2DEG plane, the conductance
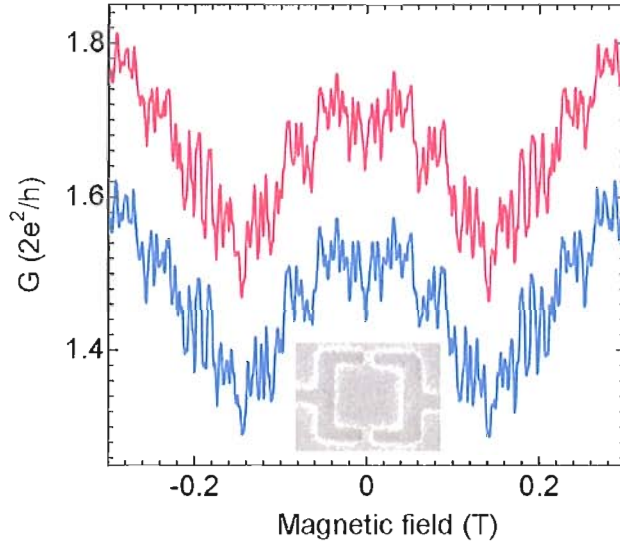
Figure 3.4. Two sets of MCF from a single square electron billiard (inset). The data sets have a resolution of 0.5 mT, and were taken several days apart during the same experiment.

of a ballistic device will change due to quantum interference between electron wavefunctions in the device. Example sets of these fluctuations are shown in Figure 3.4.

Note that the MCF are symmetric in field, which among other things demonstrates that they are not noise [41]. They are also repeatable - the two data sets are from the same device (Figure 3.4(inset)) under the same conditions, but collected days apart. The fact that they are the result of quantum interference is most readily seen by reducing the phase coherence time τ_ϕ of the electrons, for instance by raising its operating temperature. τ_ϕ is a measure of the average electron's quantum state lifetime, and increasing thermal energy raises the rate of phase coherence-breaking events in the billiard. As Figure 3.5 shows, raising the temperature gradually
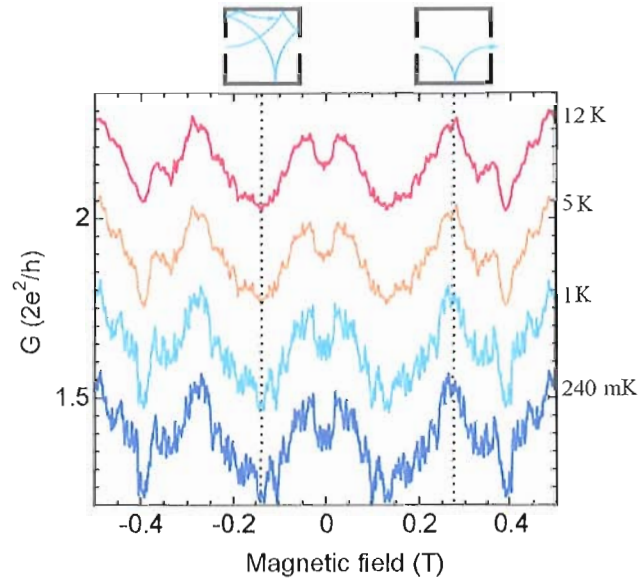
Figure 3.5. A series of MCF taken at the indicated temperatures (a), and an example of a classical magnetic focusing feature (dotted line). The dominant electron trajectory for the indicated feature is shown in schematic (inset). The traces are offset in $0.25 \times 2e^2/h$ increments for clarity.

suppresses the MCF amplitude. The remaining variations in conductance after the quantum MCF are completely suppressed can be correlated with a classical, ballistic effects like magnetic focusing. Ballistic electron trajectories are in effect 'focused' on to the narrow exit of the electron billiard by a magnetic field of the appropriate strength. An example is shown in Figure 3.5. This effect can also contribute to conductance suppression if the ballistic trajectories dictate very long (path length $\gg$ mean free path) or explicitly backscattering paths. The broadening in these features reflects in some part the spread of their velocities (direction and magnitude) upon injection from the billiard entrance.

To gain an understanding of the MCF's origin, it is helpful to first consider an
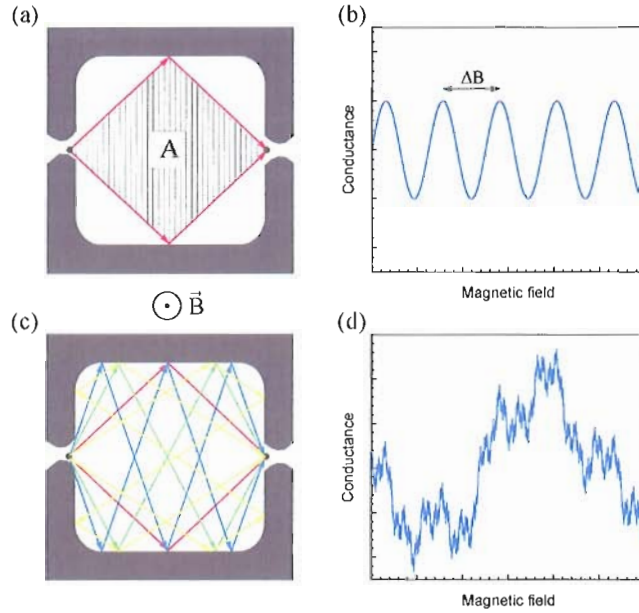
Figure 3.6. Schematics showing the origin of the MCF. A single trajectory loop encloses area A with penetrating field B (a), creating an Aharonov-Bohm oscillation with period ΔB as magnetic field is varied (b). Electron billiards actually support many trajectory loops (c), leading to a superposition of many oscillations (d).

electron trajectory loop like the one depicted in Figure 3.6(a). These two possible paths for the electron enclose some area A (shaded). Given their identical path lengths, they will constructively interfere upon meeting at the drain side of the electron billiard. However, a perpendicular applied field B has a vector potential $\vec{A}$ curling in the plane of the 2DEG, which induces a phase difference between the two paths, $\Delta\phi \approx eBA/\hbar$, from the Aharonov-Bohm effect [42]. As B is varied, the paths will alternately constructively and destructively interfere, creating an oscillation of period $\Delta B \approx h/eA$ (Figure 3.6(b)). Unlike the classic Aharonov-Bohm experiment wherein a very thin conducting ring supports only a single path (or very few, similar paths), the electron billiard hosts a wide variety of trajectory loops as illustrated

in Figure 3.6(c). Each of these loops will have differing amounts of magnetic flux penetrating it, and thus create a whole spectrum of oscillation periods as the field is varied. What is experimentally observed is a Feynman-style summation over all the possible loops for an electron, which result in aperiodic oscillations in the billiard conductance as a function of B (Figure 3.6(d)). Since MCF arise from these distributions of phase-coherent electron paths within the billiard, they make an excellent probe of electron dynamics and coherence.

For instance, our research into the statistics of MCF in electron billiards has come to the conclusion that they are *fractal*[4] over a wide range of billiard shapes and material systems [3, 4, 43, 44]. Furthermore, they can be universally characterized by an empirical parameter Q, which measures the ratio of average energy level spacing ΔE_S in the device and energy level broadening, i.e. the energy level 'resolution' within the device [3, 4, 44]. An example set of fractal conductance fluctuations, its power-law frequency spectrum, and the Q curve for electron billiards are shown in Figure 3.7. The mechanism for this interesting phenomenon is still the subject of current research [5], however a strong candidate appears to be the modulations in the billiard's potential landscape caused by the remote donor ions in the heterostructure (see Figure 3.1(c)). We hypothesize that these modulations act as soft-walled, circular,

---

[4]Briefly, a fractal is an object which has structure that repeats itself over many scales, leading to power-law behavior in its frequency spectrum. For more detailed information on fractals, the reader is referred to Chapter IV's background sections and the references therein.
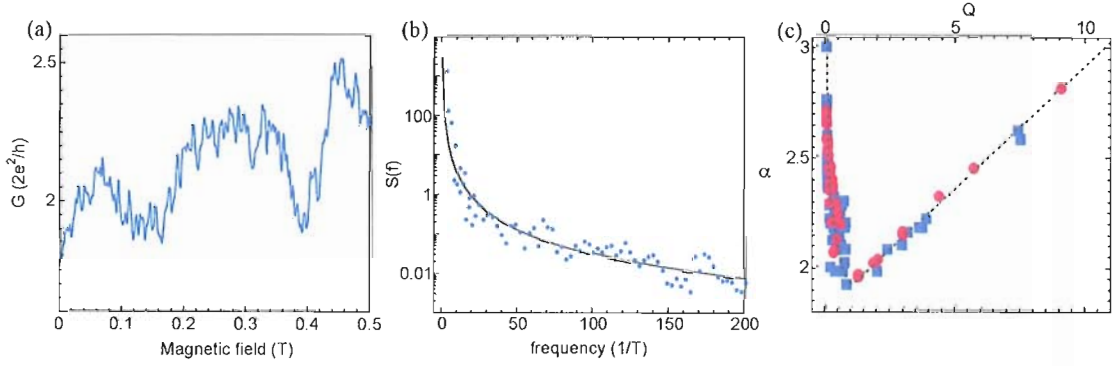
Figure 3.7. Fractal conductance fluctuations (a), their spectral analysis (b), and the Q curve for electron billiards (c). The results of the spectral analysis (b) show characteristic power-law scaling in the fluctuations. The fractal power-law scaling exponent α plotted vs. the parameter Q establishes a universal curve (c) for a variety of electron billiards in the $Al_xGa_{1-x}As/GaAs$ (red symbols) and $In_{0.25}Ga_{0.75}As/InP$ (blue symbols) heterostructures.

chaotic scatterers, which transform what would be a regular electron trajectory distribution (in a square billiard) to a mixed, regular/chaotic trajectory distribution, which is known to induce fractal conductance flucutuations [6].

Note that this behavior is well-established for a wide variety (shape, size, material) of *single* electron billiards, but has not been studied in multi-element devices. The measurement technique for ΔE_S presented in this chapter for billiard arrays will be use for these future investigations.

Electron Phase Coherence

Electron phase coherence is a prerequisite to observing quantum phenomena in electron billiards as well as many other 2DEG devices. In essence, it is an electron's retention of its quantum mechanical state, which is usually expressed in terms of

a 'phase-breaking' or dephasing time (τ_ϕ). τ_ϕ measures the average time before an electron undergoes a dephasing scattering event. There are a variety of physical mechanisms for dephasing in electron billiards: electron-phonon interactions, electron-electron scattering, or spin-orbit interactions to name a few[5]. The primary, low-temperature mechanism in semiconductor heterostructures like $Al_x Ga_{1-x} As/GaAs$ and $In_{0.25} Ga_{0.75} As/InP$ is (most probably) two electron-electron interactions, large energy transfer scattering ($\propto T^2$) and small energy transfer (Nyquist) scattering ($\propto T$) [45], which generally limit τ_ϕ to be ≤ 1 ns, though this can be exceeded using dilution fridge temperatures and ever-more-perfect materials.

One can quantitatively measure τ_ϕ by monitoring quantum phenomena that are sensitive to phase coherence. For electron billiards, this means either weak localization (i.e. phase coherent backscattering) or magnetoconductance fluctuations. Methods involving weak localization require a great deal of data averaging to reliably identify and measure the peak's magnitude [45]. In addition, at ^{3}He cryostat temperatures (~ 240 mK), the magnitude is quite small. For these reasons, we concentrate on two methods for determining τ_ϕ from MCF analysis.

The first method charts the correlation field (B_c) of the MCF in the high magnetic field regime to determine τ_ϕ [46, 47]. The specific region of magnetic field considered is

---

[5]Note that scattering from distributions of defects and device walls are not included here. These interactions are generally modeled as elastic and cause reproducible phase shifts in the incident electrons, thus preserving coherence.

the 'skipping orbit' regime, in which the cyclotron radius (r_c) of an electron trajectory fits entirely within the billiard. This causes the electrons to 'skip' along the walls of the billiard as depicted in Figure 3.8(a)(inset). When this occurs, the MCF's characteristic fluctuation period is no longer independent of magnetic field, which can be seen qualitatively by inspection (Figure 3.8(a)). The key to this analysis is drawing a relation between τ_ϕ and the field dependent characteristic field scale of the MCF, B_c. In the skipping-orbit regime, each trajectory has an average enclosed phase-coherent area,

$$A_\phi = \frac{l_\phi}{\pi r_c} \frac{\pi r_c^2}{2} = v_F \tau_\phi \frac{\hbar k_F}{2eB} \tag{3.1}$$

where v_F and k_F are the Fermi velocity and k-vector respectively. A_ϕ can be related to the MCF's characteristic field scale B_c via the Aharonov-Bohm effect [42, 46]:

$$B_c(B) = \frac{\Phi_0}{A_\phi} = \frac{8\pi^2 m^*}{h k_F^2 \tau_\phi} B \tag{3.2}$$

where $\Phi_0 = h/e$ is the magnetic flux quantum. The last link is the correlation function [48, 49], whose half width at half max is defined as B_c,

$$F(\Delta B) = \langle \delta g(B) \delta g(B + \Delta B) \rangle; F(B_c) = \frac{1}{2} F(0) \tag{3.3}$$

where $\delta g(B) = G(B) - \langle G \rangle$.

Thus to find τ_ϕ, three quantities must be experimentally determined: m^*, k_F, and B_c. The first two can be measured via the Shubnikov-de Haas effect [50], which is inherent to the material, not the device. The third requires evaluation of the correlation function $F(\Delta B)$. First, a low frequency, classical background
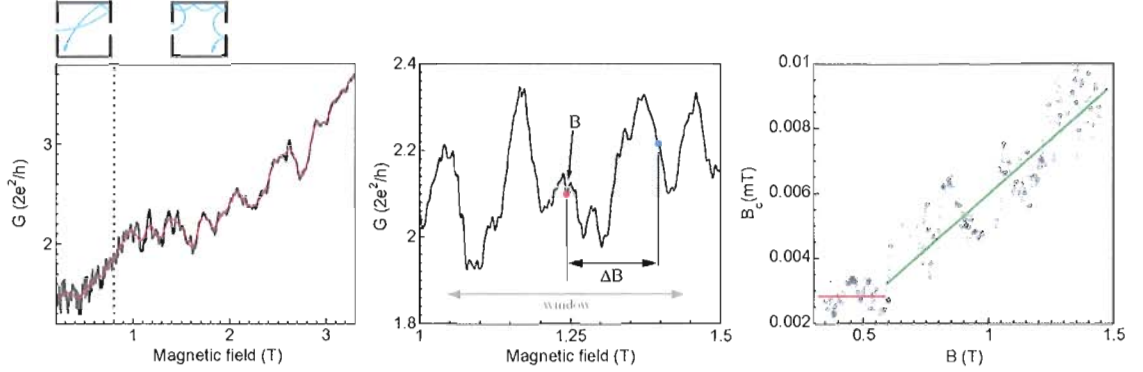
Figure 3.8. An example set of MCF going through the correlation field analysis. The MCF are plotted (a) over the universal and skipping-orbit field regimes (schematics above plot) with a low-frequency background fit (red line). A section of the skipping-orbit MCF during a single analysis step is shown in (b). The result (c) of the full analysis, B_c vs. B, is shown with linear fits to the low-field and skipping orbit field regimes.

(Figure 3.8(a), red line) is subtracted from the fluctuations to translate $G(B)$ to $\delta g(B)$. $F(\Delta B)$ is then computed for a ≈ 0.4 T window centered at magnetic field B (Figure 3.8(b)), producing an associated B_c. This process is repeated over many B values such that a plot of B_c vs. B (Figure 3.8(c)) can be produced and τ_ϕ extracted from Equation 3.2. Typically, the largest sources of error in this analysis come from the determination of the frequency cutoff used for the classical background subtraction and fitting to the linear trend in B_c vs. B. The error inherent in the latter is obvious considering the scatter in Figure 3.8(c). The former can be done systemically, for instance by comparing to the frequency content of the device's MCF at high temperatures where quantum effects are suppressed. The τ_ϕ results from a small spread of frequency cutoffs are factored into the measurement error.

The second method analyzes the statistics of MCF in the low-field regime to determine τ_ϕ. The derivation of the correlation field technique (shown above) relies on predicting the average coherent areas enclosed by classical orbits of single electrons. This second method is derived from a formulation of random matrix theory (RMT). Briefly, RMT is a method of determining the statistical properties of a physical system via correlation functions derived from ensembles of Hamiltonians or scattering matrices. It was originally applied to determine energy level distributions in heavy nuclei [51, 52]. More recently, the theory became popular for describing electron billiards, diffusive quantum wires, etc, after research showed that the Wigner-Dyson ensemble of Hamiltonians applied generally to classically chaotic systems [40] and that the properties of large random matrices were linked to universal conductance fluctuations in diffusive conductors [53]. These developments and subsequent advances are covered in large part by C. W. J. Beenakker's review paper [30].

Recently RMT has been extended to treat finite temperature and phase-breaking phenomena in electron billiards [54, 55], which has since been experimentally validated in comparison to the correlation field technique [28, 56, 57]. Implementing the RMT-derived method requires the evaluation of the following integral in the universal MCF regime,

$$(\delta G)^2 = \int_0^\infty \int_0^\infty f'(E)f'(E')\frac{\langle G\rangle^2}{(N+N_\phi)^2 + 4\pi^2(E-E')^2/\Delta E_S^2}\,dE\,dE' \qquad (3.4)$$

where $(\delta G)^2$ is the variance of the MCF in the universal regime, $f'(E)$ is the derivative of the Fermi function, and $N = N_1 + N_2$, the total number of conducting modes

in the entering (N_1) and exiting (N_2) quantum point contacts (QPCs)[6]. At zero temperature, the $f'(E)$'s reduce to delta-functions and the need to integrate over a thermal spread of electron energies is removed. Loss of phase coherence in this model is represented by electrons 'escaping' the dot via a fictitious lead attached to a phase-randomizing reservoir. The escape rate is set by the average energy level spacing in the billiard, ΔE_S, and is related to N_ϕ by the expression $N_\phi = 2\pi\hbar/\tau_\phi \Delta E_S$ [58][7]. In the absence of phase-breaking interactions, $(N + N_\phi) \to N$.

As previously mentioned, this integrand must be evaluated in the universal MCF regime. Additionally, similar to the correlation field method, a low-frequency classical background must be subtracted from the MCF to ensure the calculation of $(\delta G)^2$ includes only fluctuations that originate from quantum interference. Figure 3.9 demonstrates these constraints on the same data set used for depicting the correlation method in Figure 3.8. The low end cutoff for the universal regime is the field scale for time-reversal symmetry breaking, $B \sim \Phi_0/A_{dot}$, where A_{dot} is the area of the billiard. This is the field scale at which the weak localization effect should be completely suppressed [59]. The high end cutoff is where the ballistic trajectories in the billiard begin to transition to the skipping-orbit regime, which corresponds to $B \sim \dfrac{\hbar k_F}{er_c}$, where $r_c = (1/2)(L)$ (see Figure 3.9). Once these steps are accomplished, $(\delta G)^2$

---

[6]Quantum point contacts are the narrow openings that connect the billiard to the bulk 2DEG. These are treated as short, 1D wires, which have a strongly-discretized energy spectrum. Each occupied level contributes $2e^2/h$ to the conductance, and the number of occupied levels N can be tuned with an electrostatic gate or magnetic field (see Figure 3.11).

[7]Note that the fictitious lead draws no net current - the electrons that escape to the phase-randomizing reservoir are re-injected at an equal rate, conserving electron number in the device.
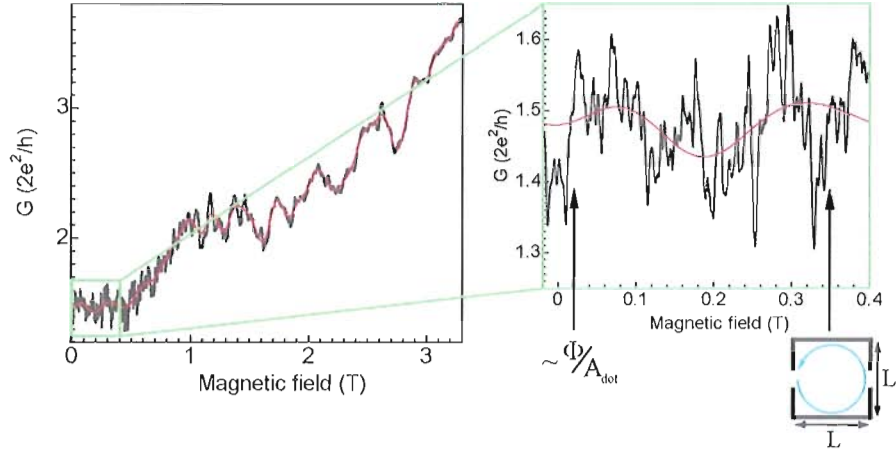
Figure 3.9. Data selection for the RMT τ_ϕ analysis. The full MCF data set is shown (left) with the region of interest shaded. A magnified view of this region (right) indicates the necessary cutoffs in magnetic field to address only the universal regime fluctuations.

can be calculated, and τ_ϕ can subsequently be extracted by evaluating Equation 3.4 numerically.

Device Fabrication and Architecture

The semiconductor billiards studied in this dissertation were made by Dr. Colleen Marlow in collaboration with the Nanometer Consortium at Lund University, Sweden. For more fabrication details, the reader should refer to Dr. Marlow's dissertation [57].

Fabrication

All the devices studied in this dissertation were fabricated in an $Ga_{0.25}In_{0.75}As/InP$ heterostructure, which is shown schematically in Figure 3.10(a). This material system
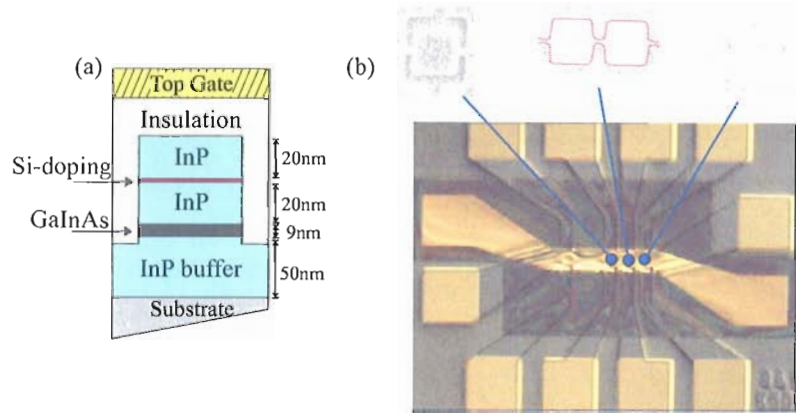
Figure 3.10. (a) The $Ga_{0.25}In_{0.75}As/InP$ heterostructure etched to a narrow channel, (b) SEM images of the one, two, and three billiard arrays, and their locations in the Hall bar (below). The two billiard array has a typical depletion profile indicated in red.

was selected primarily for its very low effective mass, measured to be 0.040 m_e in our wafer, and for its superior fidelity in terms of device geometry. The effective mass is low even compared to the canonical heterostructure used for 2DEG experiments, $Al_xGa_{1-x}As/GaAs$, whose effective mass is $\approx$ 50% greater (0.067 m_e). This low effective mass increases the carrier mobility in the material and the energy level spacings within the billiards, both of which enhance the ability to observe quantum interference phenomena. Further information on the heterostructure can be found in the literature [27, 60].

Device geometry can be particularly well-defined in this heterostructure, because none of the constituent materials are strongly oxidizing, which enables chemical etching for device definition. In contrast, $Al_xGa_{1-x}As/GaAs$ heterostructures cannot be effectively etched due to the presence of aluminum, the oxide of which is an

insulator and forms quickly at atmosphere. Etching our devices creates a confinement potential that is an order of magnitude steeper than the equivalent in surface gate-defined devices [60]. In addition to creating a well-defined device shape, this steeper potential also enables the number of conducting channels in the QPCs to be altered by the top gate without strongly perturbing the billiard geometry.

For our study of coherent transport phenomena in billiard arrays, three separate devices, comprising one, two and three coupled billiards, were defined in the 2DEG confined to the 9 nm $Ga_{0.25}In_{0.75}As$ quantum well. The arrays were patterned using electron beam lithography and chemically etched into the mesa of a Hall bar (see Figure 3.10(b)). The component billiards were defined to be nominally identical squares with lithographic dimensions 0.77 μm $\times$ 0.73 μm ($\pm$0.01 μm) and connected to one another and the surrounding 2DEG by QPCs 100 nm $\pm$ 5 nm in width.

To control the carrier density simultaneously in the Hall bar and all three devices, a uniform Ti/Au electrostatic gate was deposited over the entire structure. Leakage current was eliminated by separating the top gate from the heterostructure surface with a 1 μm insulating polymer (PMMA) layer. In this experiment, a top gate bias of $V_g = 0$ V at temperature $T = 240$ mK resulted in a carrier density $n_s = 6 \times 10^{11}$ cm^{-2} and mean free path $l_t = 3$ μm.
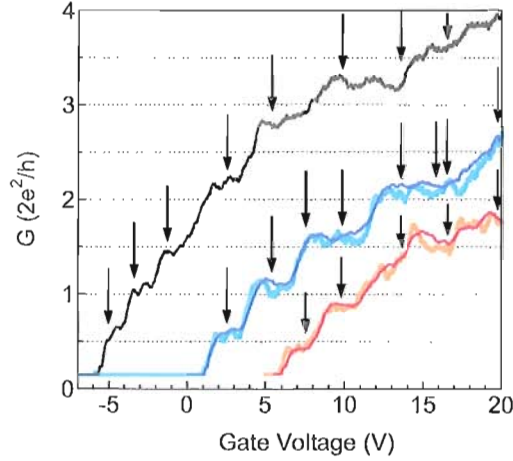
Figure 3.11. Conductance vs. gate voltage for the three billiard array devices. The black arrows indicate the voltages at which MCF were measured.

Hybridization in Electron Billiard Arrays

The Experiment

The arrays were cooled to $T = 240$ mK $\pm$ 5 mK in the Oxford ^{3}He refrigerator and their conductance G was measured using 37 Hz lock-in detection in the four-probe configuration detailed in Chapter II. All measurements were performed at a 1 nA constant current. The MCF were measured at plateaus observed in the conductance of each array vs. top gate voltage (see Figure 3.11). The MCF for each device were measured between -0.6 T and $+3.5$ T. The negative field region is useful for determining a baseline noise amplitude, since field symmetry is expected in the linear regime of transport. The region above ≈ 0.5 T, the so-called 'skipping orbit'
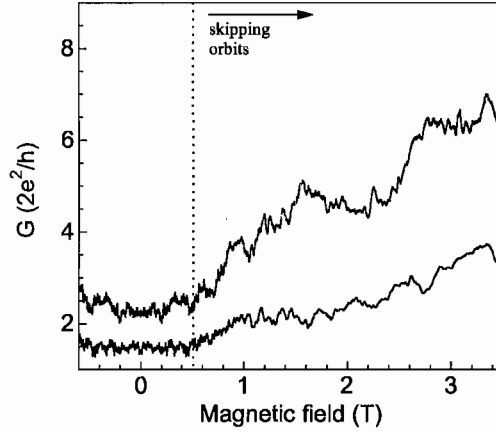
Figure 3.12. Three examples of MCF from the single billiard array. The dotted line approximately indicates the border between the low field universal regime and high field skipping orbit regime.

regime, is required to determine τ_ϕ using the method pioneered by Bird, et al. [46]. A few examples of complete MCF data sets are shown in Figure 3.12.

It is important to note that for our subsequent analyses it is useful to parameterize coupling between billiards within each array using the mean conductance $\langle G \rangle$ of the MCF, which increases as the top gate populates additional modes in the QPCs. $\langle G \rangle$ was calculated at magnetic fields where chaotic electron transport and time-reversal symmetry breaking occur simultaneously, which is in the range $0.02 < B < 0.4$ T for our devices. The MCF in this regime can be analyzed using the RMT analysis, [28] which plays an important role in our technique.
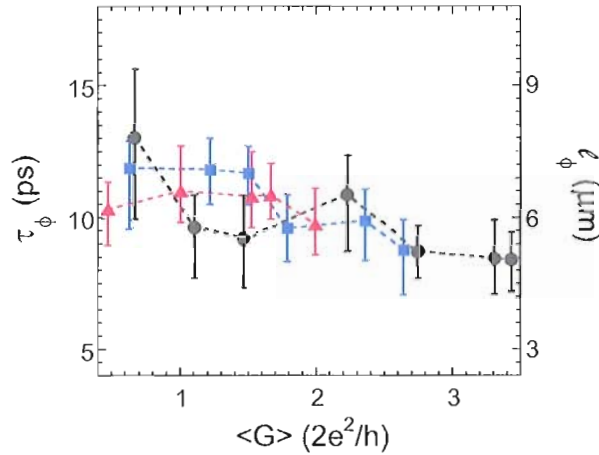
Figure 3.13. Phase coherence time (τ_ϕ) and length (l_ϕ) vs. $\langle G \rangle$ for the three billiard arrays. The single, double, and triple billiard arrays are represented by circles, squares, and triangles respectively.

Establishing Phase Coherence

We use the correlation field analysis (described in detail earlier) to measure τ_ϕ. Figure 3.13 shows τ_ϕ and the equivalent phase-breaking length[8], (l_ϕ) vs. $\langle G \rangle$ for each array. As expected for identical material environments, all three arrays have approximately the same phase coherence length of $l_\phi \approx 6$ μm. This value decreases slightly as the number of coupling modes N increases, which is in line with expectations. The suppression has been explained previously as an effect of the increased exposure of the billiards to the 'bulk' 2DEG environment [61].

---

[8]$l_\phi = v_F \tau_\phi$, where v_F is the electron Fermi velocity. It should be noted that $v_F = \hbar\sqrt{2\pi n_s}/0.040m_e$, and thus changes slightly over the plotted domain of $\langle G \rangle$. However, the change is small - well within the error bars indicated.

Measuring Hybridization

To assess the degree of hybridization occurring in the multi-billiard arrays, we measure the average quantum energy level spacing ΔE_S as determined by combining the two previously discussed methods for extracting τ_ϕ from the MCF: the correlation field analysis [46] and the RMT analysis [56].

Previous research has shown that values of τ_ϕ obtained from Eq. 3.4 and those extracted from the correlation field analysis are consistent [28, 57]. Thus we may extract ΔE_S from Eq. 3.4 by numerical integration[9], using the values of τ_ϕ from the correlation field analysis along with the measured values for N, δG, T, and $\langle G \rangle$ as inputs.

To establish a baseline for this technique, we first examine the results for the single billiard array (Figure 3.14(a), black circles). For comparison, the value of ΔE_S is calculated from the dot's enclosed area A via the relation $\Delta E_S = 2\pi\hbar^2/m^*A$. This simple approximation shows a downward trend with $\langle G \rangle$ caused by the slight increase in A due to decreased electrostatic depletion. Values of ΔE_S measured using Eq. 3.4, though largely commensurate with the approximation, show an even steeper decrease, which we tentatively assign to a combination of reduction in A and also an increase in hybridization between the wavefunctions in the billiard and QPCs.

For the two and three billiard arrays, our technique should produce significantly

---

[9]Calculations were completed using Mathematica's NIntegrate function. Though convenient, the automatic function often uses too coarse a grid for integrating over functions with sharp features. Grid resolution was manually increased for our calculation, and its accuracy was tested against several functions with similarly sharp features and known volume.
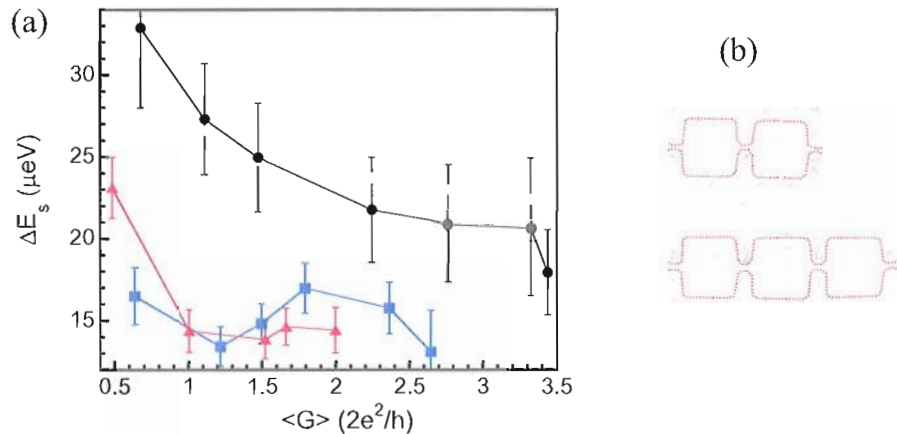
Figure 3.14. (a) displays the result of the ΔE_S analysis for the one, two, and three billiard arrays (circles, squares, and triangles respectively) and a baseline derived from single billiard's lithographic area (gray circles). Minimum perimeter quantum interference loops (b) for two and three billiard arrays (solid white) are superimposed on SEM images of the devices along with typical wall depletions (dotted red).

smaller ΔE_S values if the devices are effectively acting as a single quantum system. Figure 3.14(a) shows the results for the two (squares) and three (triangles) billiard arrays, and a significant drop in ΔE_S is indeed observed. However, the three billiard array shows a degree of hybridization very similar to that of the two billiard array. We propose that this can be understood by examining the characteristic l_ϕ values in Figure 3.13. Recalling the Aharanov-Bohm interpretation of the MCF, we can picture the smallest quantum interference loop as the diamond shapes shown in Figure 3.14(b), the minimum perimeter for a loop spanning the two billiard array is 4.2 μm, while for the triple array it is 6.4 μm. Thus the measured $l_\phi \simeq 6$ μm easily accommodates the minimum perimeter coherent interference loop spanning the two billiard array, but the corresponding loop perimeter in the three billiard array is $\gtrsim l_\phi$

and consequently has a much reduced likelihood of coherent transport over all three dots.

Given these results, we can conclude that the technique produces the proper result for 1) the baseline case of a single billiard, 2) the case of hybridized billiard array, and 3) and finally, the case where lack of phase coherence limits the extent of hybridization between array elements. To further substantiate our method, we present two complementary analyses in the following section.

Supporting Analysis

We first consider the possible scenario in which each dot in an array acts as an isolated quantum system, i.e. the wavefunctions do not couple, but are instead contained within the square geometry of the billiard. If this is the case, then the MCF generated by each dot in the array will be independent of the MCF from neighboring billiards after a subtraction of the low frequency, geometry-dependent features. This will lead to ensemble averaging of the measured MCF, such that $\delta G_{total} = \delta G_{billiard}/\sqrt{N_{billiards}}$. The solid gray lines in Figure 3.15 plot the fitted trend in δG for the single dot and for a two billiard and three billiard array assuming this ensemble averaging. The measured δG are shown for the one, two, and three billiard arrays (circles, squares, and triangles respectively). The gray trend lines do not fit to the measured data for the double and triple arrays, indicating that some
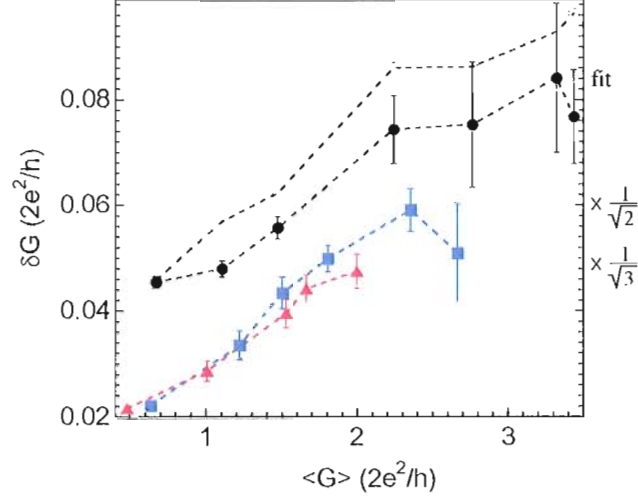
Figure 3.15. δG vs. $\langle G \rangle$ for the one (black circles), two (squares), and three (triangles) billiard arrays. Also shown (in solid gray) are a fit to the one billiard trend, and that trend scaled by $1/\sqrt{2}$ and $1/\sqrt{3}$ to show trends expected from fluctuation ensemble averaging. A theoretical prediction from RMT for the single billiard is also shown (open circles).

wavefunction coupling must be occurring between the dots. The absence of ensemble averaging has also been observed for open dot arrays in GaAs heterostructures [61].

This analysis of δG can also be used to check the applicability of RMT to our devices. Figure 3.15 includes a calculation of $\delta G = N_1 N_2/(N^2 + N_\phi N)$ for the one billiard array based on a zero-temperature prediction from RMT that includes phase decoherence [54]. The number of physical modes in the QPCs are calculated from the mean conductance $\langle G \rangle = [1/N_1 + 1/N_2]^{-1}(2e^2/h)$, [54] while $N_\phi = m^* A/\hbar \tau_\phi$ is calculated using the billiard's enclosed area A obtained from simulations of the confinement potential [60]. The observed reduction in the measured values of δG compared to this theory is expected due to the suppression of the MCF amplitude at non-zero temperature. The reasonably close agreement between the measured and
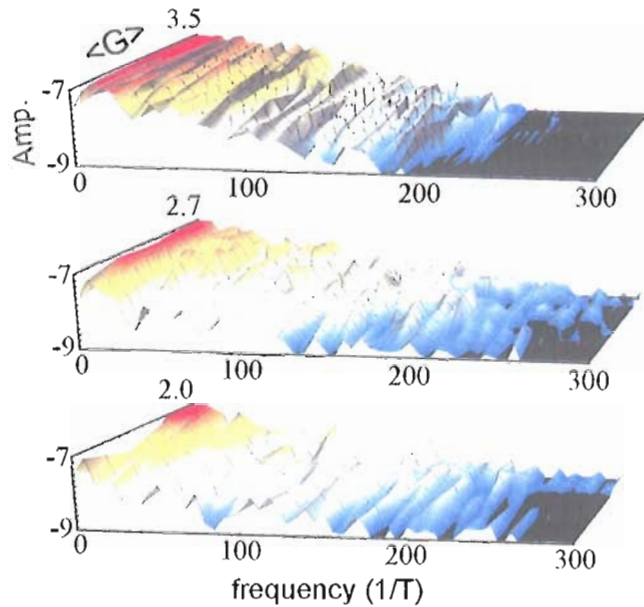
Figure 3.16. Fourier analysis for the one (a), two (b), and three (c) billiard arrays. Plotted frequency and amplitude ranges are fixed for all three devices to aid in their comparison. For the $\langle G \rangle$ axes, the minima correspond to a single conducting mode ($\langle G \rangle \approx 0.5 * 2e^2/h$), and the maxima are indicated.

predicted trends in δG for the single billiard confirms the applicability of RMT to these devices.

Fourier analysis provides a final check on our conclusions. The power spectrum (the modulo-square of the complex Fourier transform) for each data set is shown in Figure 3.16 for the one, two, and three billiard arrays. By inspection, the two billiard array (Fig. 3.16(b)) has significantly more high frequency content than the single billiard (Fig. 3.16(a)). However, the three billiard array shows no appreciable difference compared to the two billiard array, further confirming that the extent of hybridization is limited by de-phasing. Recall that higher frequency fluctuations

correspond to a larger spatial extent of electron quantum interference loops, [62] which we would expect for larger coherent systems like the hybridized arrays [25]. Note that the mild downward trend in ΔE_S observed in Figure 3.14 for the three devices is reflected in the power spectra, with higher frequency structure increasing mildly with coupling strength $\langle G \rangle$.

Conclusions

In summary, we have demonstrated a quantitative method for extracting ΔE_S, which is a direct indicator of wavefunction hybridization in an array of electron billiards. The arrays show hybridization over the entire range of measured coupling strengths ($N_{1,2} \approx 1$ to 4). Although we have concentrated on ballistic transport, the τ_ϕ measurement method (RMT) that forms the basis of our measurement technique has a corresponding expression for the diffusive transport regime [30]. The correlation field method also has a diffusive regime analog, though it is evaluated in the universal rather than skipping-orbit regime [49]. Thus the technique explored here could be expanded to act as a tool across a wide range of coupled quantum coherent devices.

CHAPTER IV

TRANSPORT IN FRACTAL ELECTRONIC DEVICES

Introduction

This chapter will explore the potential for novel, complex functionalities in electronic circuits that are *fractal* in their geometry, i.e. have a fractional, non-Euclidean dimension. For motivation, recall that our research into the statistics of MCF in electron billiards has come to the conclusion that they are fractal over wide range of billiard shapes and material systems [3, 4, 43, 44][1]. Having established fractal behavior in the output of a nominally Euclidean set of devices, the electron billiards, an interesting question is: what functionality might we be able to produce when the device itself has a fractal geometry?

We know that many natural structures have fractal geometry, from trees [1] to coastlines [63] to clouds [64] to galaxy distributions [65] and beyond. Though there are some that are more observational curiosities than anything else, the pervasiveness of fractals in nature can be understood in many cases by considering the advantageous properties that result from the scale-invariant complexity of fractal objects. For

---

[1]The reader may also refer to the MCF subsection in Chapter III for a brief summary of these results.

instance, fractal trees have very high surface-to-volume ratios on account of their fractional dimension. Fractal coastlines tend to be very effective in dispersing the energy of incident waves. Fractal neurons [66] benefit from very high connectivities.

Such properties have made artificial fractal structures the subject of increasing fundamental research (e.g. optical transmission [67], quantum interference [68], and AC electron transport [69]) and technological applications (e.g. capacitor [70] and antennae [71] designs). To begin to answer what functions other fractal electronic devices may have, this chapter presents electrical simulations of fractal resistor networks, which are found to generate novel, nonlinear electrical properties in a simple gating scheme. This is followed by a proposal for implementation of these devices in the form of fractal diffusion-limited aggregates [72] of semimetal atomic clusters[2].

---

[2]This proposal was developed in collaboration with Professor Simon Brown's group at University of Canterbury, whose experimental apparatus and expertise will be integral to future device implementation.

Fractals and Fractal Devices

This section will offer an abbreviated background on fractals, fractal analysis methods, and the artificial fractal devices that have appeared in the literature. The reader is referred to more comprehensive reviews of fractals and fractal analyses for further details [1, 73, 74].

Fractals

A fractal is strictly defined as an object which displays self-similarity at all scales. Hence fractals are often referred to as 'scale-free', appearing the same to examinations over any number of size scales. An example of an exactly self-similar fractal is shown in Figure 4.1. However, this type of fractal can only exist as an ideality, since any physical fractal's scaling will necessarily be cut-off at the small and large size scales by either our ability to observe it or the constraints of the material system. For example, the fractal nature of cloud cover [64] can only be observed as well as the weather satellites can detect it. Furthermore, its absolute minimum size scale is set by the smallest cloud constituent, a water molecule, while its maximum size is set by the surface area of the Earth.

When discussing most natural fractals like clouds, trees, and coastlines, it is also important to note that the property of *exact* self-similarity no longer holds. Instead it is the *statistical* properties of the pattern that repeat over the fractal scaling
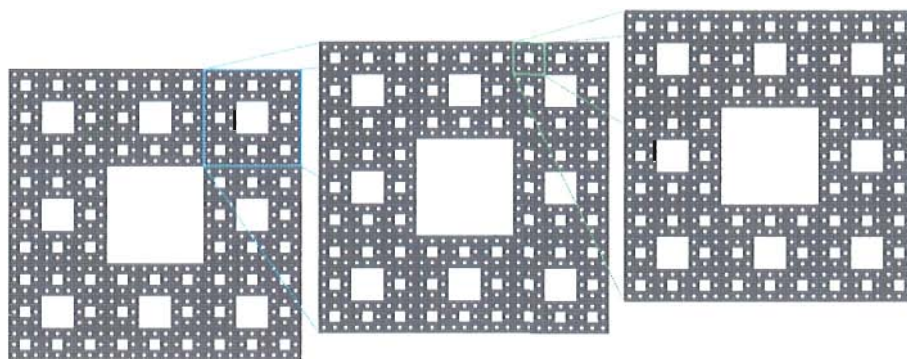
Figure 4.1. An example of exact fractal scaling as found in a Sierpinski carpet pattern.
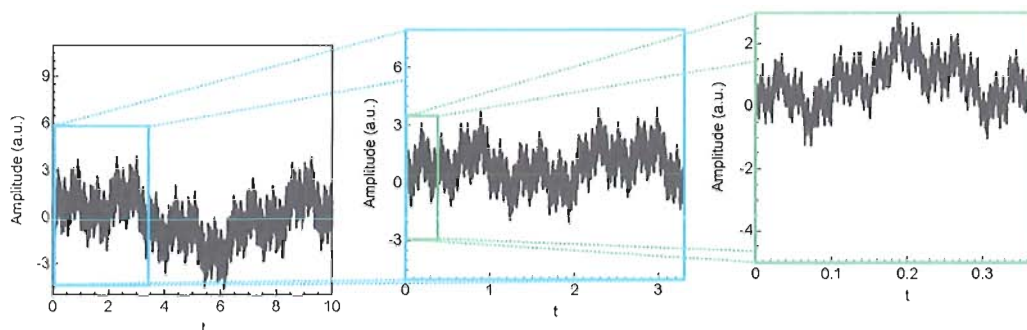
Figure 4.2. An example of statistical fractal scaling as found in one instance of the Weierstrass-Mandelbrot function.

range. In artificial fractals, like the Weierstrass-Mandelbrot (W-M) function [75] depicted in Figure 4.2, variations are included by adding in some random process. For the W-M function, this is accomplished by deliberately randomizing the phase and/or amplitude of the constituent sine waves. For natural fractals, any number of randomizing influences (Brownian motion, for instance) are already present in the environment. This results in, for example, oak trees that vary widely in terms of branch-for-branch correspondence, despite sharing an underlying statistical fractal character.

Statistically self-similar fractals are more difficult to identify than the exactly self-similar variety. In the situation where one does not know whether an object is a fractal, exact self-similarity is relatively easy to pick out by examining the object at different magnifications. Though it can be trickier than the case of the Sierpinski carpet in Figure 4.1, the fractal geometry of such objects can often be identified by inspection. In the statistical case, inspection may suggest self-similarity, but the absence of an exactly repeating pattern makes the characterization qualitative at best. Because statistical fractals are so prevalent in the natural world and are thus studied quite widely, researchers have developed a variety of methods to evaluate the presence and extent of an object's fractal scaling. Two methods will be highlighted here, because of their relevance to our research.

The simplest is known as the box-counting method [73, 76] The technique proceeds as follows: the object (Figure 4.3(a)), which is in this case a modified Koch curve, is covered with a computer-generated mesh of identical squares ('boxes'). The number of boxes, $N(L)$, that contain any part of the object is then counted, and this count is repeated as the size, L, of the squares in the mesh is reduced. $N(L)$ gives a measure of the spatial coverage of the object, and reducing the box size is analogous to looking at this coverage at finer and finer magnifications. For fractal behavior, $N(L)$ scales according to the power law relationship $N(L) \sim L^{-D}$, where $1 < D < 2$. This power law generates the scale-invariant properties that are central to fractal geometry and manifests itself as a straight line in the 'scaling plot' of $log(N(L))$ versus $log(L)$, as
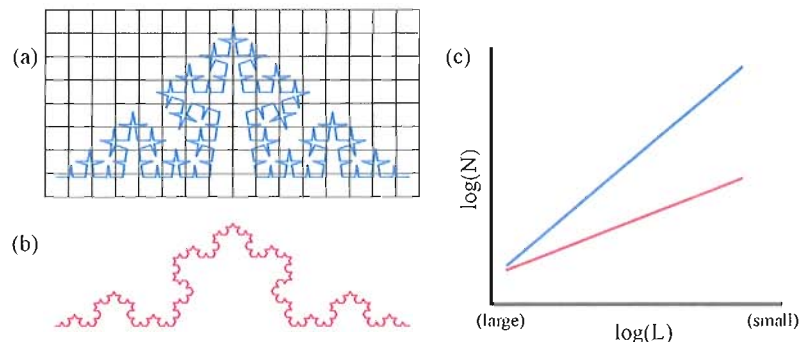
Figure 4.3. A schematic example of the box-counting fractal analysis. The modified Koch curve (a) matches to the line of matching color in (c), the box-counting scaling plot. The standard, lower D Koch curve matches color with the bottom line.

shown schematically in Figure 4.3(c). The gradient of the line is equal to D, which is referred as the object's fractal dimension. For comparison, Koch curve constructed via a different generation rule is also shown (Figure 4.3(b)). It is also a fractal, but possesses a lower D. The two Koch curves have similar size, which means that their box-count at large box sizes is approximately the same. The effect of (a)'s higher D is to fill many more boxes at the smaller scales, implying a greater amount of fine scale structure compared to the smoother, lower D Koch curve (b).

Another method for characterizing fractals is by conducting an analysis of its 'mass' scaling. The analysis is conceptually quite simple. Selecting a central point in an object, draw a circle or box around it, and count the number of elements (say, image pixels) that lie inside a box of that size. Expand the box, and count again. These steps are repeated until the box grows to the size of the object, and one is left with a data set of mass (M) vs. box side length (L) with the general form $M = kL^D$.
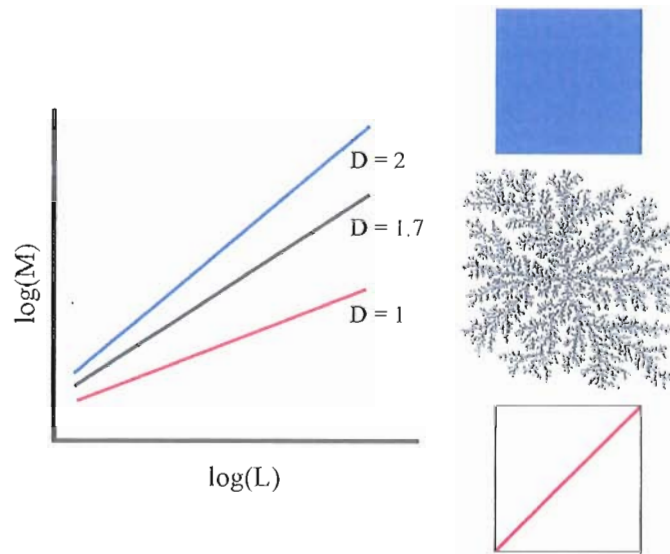
Figure 4.4. Examples of the mass scaling analysis. A square (top curve) and line (bottom curve) reproduce their Euclidean dimensions, but a fractal object (a simulated diffusion-limited aggregate) takes on a fractional dimension.

The results for objects of various geometries are shown in Figure 4.4. A solid square's mass scales as the square of L, giving the expected $D = 2$ result. On the other extreme, a line's mass scales linearly with L, thus $D = 1$. Fractals, like the pictured diffusion-limited aggregate, scale with an exponent $1 < D < 2$ ($= 1.7$ in this case). All this is similar to the box-counting method, the major difference being that the mass analysis counts within each box rather than simply counting it as full or empty. However the result of each, the fractal dimension D, is generally equal, except in the special case of a so-called 'multifractal' object. In this case, the mass dimension is slightly smaller [77, 78].

Though the mass scaling analysis is easy to describe, it can be difficult to implement properly. Consider picking a different central point on the object around

which to examine the mass scaling. Despite being technically no less valid, the mass distribution in its immediate vicinity may be very different than the original point, especially if the object is spatially inhomogeneous. To mitigate this effect, it is advisable to average the results of many instances of the mass analysis, all with different central points. For large ($\sim 1000+$ pixels on a side) images it can become computationally very expensive to arrive at a reliable result, though this problem can be mitigated with some clever programming [72].

Given the analytical equivalence of the two methods for the objects studied in this chapter, we primarily use the box-counting method for its ease of implementation. By way of confirmation, the mass scaling analysis has been applied previously to diffusion-limited aggregates similar to ours [72, 79, 80] and arrived at the same fractal dimension.

Devices with Fractal Geometry

Given the prevalence of fractal geometry in nature and the advantages it brings with it, it is not surprising that there is significant body of research regarding artificial fractal devices. This began with investigations of diffusion in a fractal medium [81–83], which was subsequently applied to the scaling of electrical conduction in random-resistor networks, of which [84] supplies a good review. This theoretical research has in turn lead to applications in bulk disordered semiconductors and granular metals [85, 86].

More recently, devices with engineered fractal geometry have been appearing in the research literature and in application. On the research side, certain aspects of the electrical and optical properties of fractal elements have been considered in some detail. Optically, research has concentrated largely on the infrared transmission spectra of metallic films with fractal patterning [67, 87–89]. These fractal, sub-wavelength aperture patterns (a Sierpinski carpet and a Cayley tree) show plasmon-induced transmission resonances over a broad band of frequencies, which is attributed to their hierarchical, multi-scale structure.

Research into the electronic properties of fractal devices has largely considered the *asymptotic* case, where fractal scaling is assumed to continue over all scales. This approach has been useful in determining the 'bulk' electrical properties of fractal objects. For example, the conductance G of a fractal network is $\propto L^{D-2-\alpha}$, where L is the linear size of the network, D is the fractal dimension, and α is an exponent characterizing the "anomalous diffusion" encountered by an electron on a fractal network [90]. The AC response of fractal networks, particularly the scaling properties of their impedance, have also been considered in a variety of fractal systems [91].

The case of fractal networks or elements with limited scaling ('real' fractals, in other words) has also been considered in some instances. These investigations have lead to the discovery of anomalous electrical properties dependent on the fractal geometry of the device. Calculations involving passive circuit elements on a Sierpinski gasket network reveal log-periodic oscillations of the device impedance

vs. frequency [69]. Experiments on a lithographically defined fractal tree [92] and Sierpinski gasket [93] have found interesting fractal phenomena in the device input impedance and magnetoresistance respectively. On the applied side, research into capacitors with fractal interfaces shows a large increase of capacitance per unit area over conventional designs [70]. Fractal electronic devices have even found their way out of the laboratory in the case of antenna [71], where the fractal's multiscale spatial structure allows greater performance in applications that require multi- or broadband antenna response, like cell phones.

This broad array of interesting and useful phenomena in fractal devices has informed our investigations into the DC electrical properties of fractal electronic devices. In our approach, detailed below, we simulate the response of fractal circuits to structural modification via electrostatic gates.

<p style="text-align:center"><u>Fractal Circuit Simulations</u></p>

<p style="text-align:center">Simulation Details</p>

All the electrical simulations in this chapter were carried out using a Mathematica program that took 4-color images as input and computed the resistance of the 'circuit' using a circuit simulation technique known as modified nodal analysis (MNA) [94]. The basic process for the program is to translate the image into a matrix of current junction rules. Figure 4.5 shows the translation from image pixels to electrical circuit elements. For instance, a black pixel (Figure 4.5(a), 2nd column, 2nd row) with
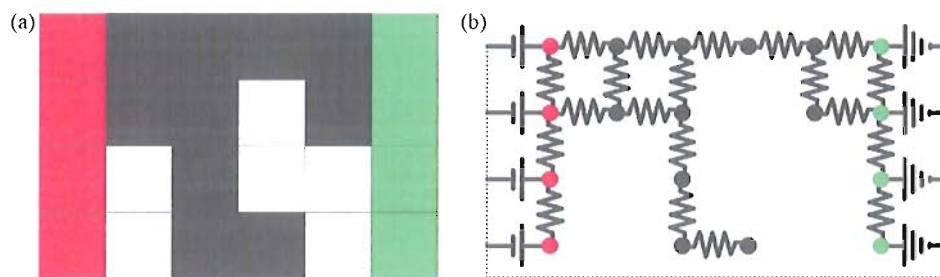
Figure 4.5. An example image to circuit translation. A small (6 × 4) pixel 4-color image, (a), is equivalent to the electrical circuit, (b), with each appropriately colored node (dots) taking the place of each pixel. White pixels, which represent empty space in the model, drop out during the translation.

nearest neighbors of one red pixel, one white pixel, and two black pixels is translated into a junction with connections to two resistors (black) and a DC source (red) (Figure 4.5(b)). The white pixel is interpreted as an infinite resistance with no corresponding connection.

The translation of a circuit to junction rule matrix via MNA essentially involves writing down junction rules to construct an $(n + m) \times (n + m)$ matrix involving m voltage sources (red pixels) and n nodes (junctions). The process for this can be reduced to a few simple rules, but the matrix itself can quickly become very large. For instance, Figure 4.5's circuit translates to a 28 × 28 matrix. Figure 4.6 shows a smaller circuit (a) and its corresponding matrix (b) to illustrate the process. For a more detailed look at the program's contents and MNA, the reader is referred to Appendix A.

This approach yields a simple, relatively flexible method for determining the DC electrical characteristics of circuits with arbitrary geometries. It is thus a good

(a)

(b)

$$
\begin{array}{c} \\ a \\ b \\ c \\ d \\ e \\ source \end{array}
\begin{bmatrix}
\frac{1}{R_1} & \frac{-1}{R_1} & 0 & 0 & 0 & 1 \\
\frac{-1}{R_1} & \frac{1}{R_1}+\frac{1}{R_2}+\frac{1}{R_4} & 0 & \frac{-1}{R_4} & 0 & 0 \\
0 & \frac{-1}{R_2} & 0 & 0 & \frac{-1}{R_5} & -1 \\
0 & \frac{-1}{R_4} & 0 & \frac{1}{R_4}+\frac{1}{R_3} & \frac{-1}{R_3} & 0 \\
0 & 0 & 0 & \frac{-1}{R_3} & \frac{1}{R_4}+\frac{1}{R_3} & 0 \\
1 & 0 & 0 & 0 & 0 & 0
\end{bmatrix}
\begin{bmatrix} v_a \\ v_b \\ v_c \\ v_d \\ v_e \\ I \end{bmatrix}
=
\begin{bmatrix} 0 \\ 0 \\ 0 \\ 0 \\ 0 \\ V \end{bmatrix}
$$
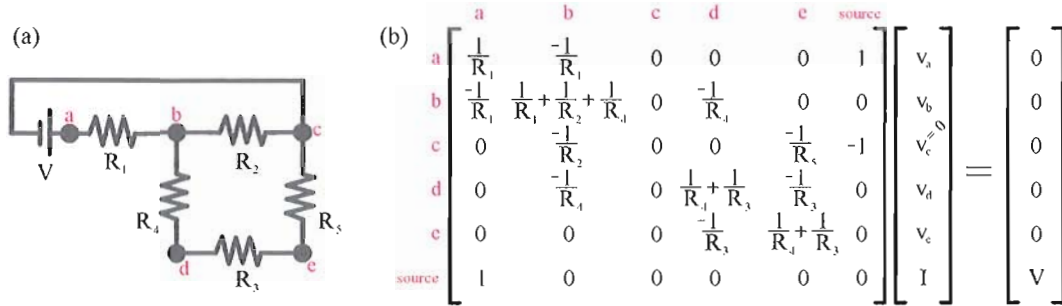
Figure 4.6. A small-scale demonstration of the MNA technique. A circuit with a single DC voltage source (V), resistors (1 - 5), and nodes (a - e) can be written out in terms of its current junction rules as in (b). The voltages at each node (v_a, v_b, etc.) and the circuit's current can be calculated by inverting the matrix shown.

first step toward charting the electrical response of our fractal circuits. Concerning fractals, it is important to note that this technique does become very computationally-intensive once the image is $\sim 10^6$ pixels (nodes) in size[3]. This limits our current simulations to fractals with $\lesssim 3$ orders of magnitude of scaling, but this is fortunately also the regime in which most natural fractals exist.

The Sierpinski Carpet

We begin by examining how to transfer the inherent nonlinearity of the fractal's spatial geometry into a nonlinear response in a device's electrical characteristics. One method for this is to deplete areas of the fractal device with a nearby or overlaid electrostatic gate. Removing features from a conducting pattern in this way will translate into an electrical response.

---

[3]More specifically, this upper limit depends on the number of current-carrying pixels (black, red, green), so larger, but very sparse images can be computed as quickly as smaller, denser images.

First, our focus is on fractals where the pattern repetition at different magnifications is exact. These fractals are relatively simple compared to statistical fractals, such as diffusion-limited aggregates (DLAs), where only the statistical properties of pattern repeat at many scales. This simplicity allows correlations between a circuit's spatial geometry and the resulting gate characteristics to be more easily identified. Nevertheless, the scaling properties of statistical and exact fractals depend on D in the same manner, such that properties identified for exact fractals will be readily transferable to statistical patterns.

Figure 4.7(a) shows an exact fractal known as the Sierpinski carpet [95], which was chosen for this study, because its high D value ($= 1.89$) is similar to that of our proposed DLA-based fractal circuit elements. For the 'Sierpinski circuit', square patterns (shown in white in Figure 4.7(a)) repeat at many size scales, at a rate determined by D. These squares represent insulating regions and therefore create a fractal distribution of conducting channels (black regions). Current passes through these channels from the source (red) to drain (green) electrodes, routed by a pair of narrow side-gates. Two gate architectures are investigated: a pair of symmetric gates positioned to be level with the central square of the circuit (i.e. with positions indicated by blue arrows in Figure 4.7(a)) and a pair of symmetric gates with positions offset from the central square (red arrows).

To simulate the effect of electrostatically depleting the material in line with, for example, the central gate pair, a series of images was produced, each one representing
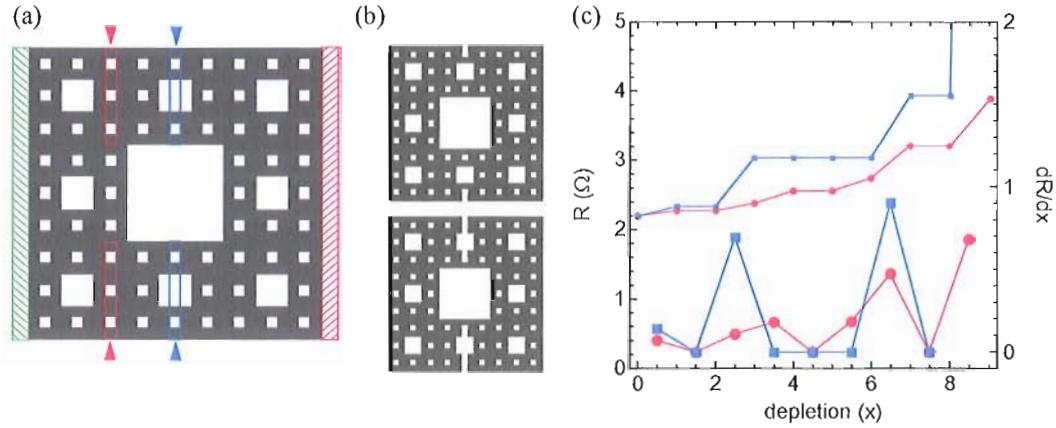
Figure 4.7. Architecture and simulation results for a 2 iteration Sierpinski circuit. The device architecture (a) has broad source (red bar) and drain (green bar) contacts on either side. The positions of the two different gate configurations are indicated with pairs of arrows, and the maximum extent of the gating is shown in matching color. Two simulation instances for the central gate pair (b) correspond to the data points for 1 and 7 pixel depletion in (c). The results of the circuit simulations (c) are shown in terms of resistance R (upper traces) and dR/dx (lower traces) vs. depletion x measured in pixels. The center gate (blue) and offset gate (red) configurations correspond to the appropriately colored traces.

a different 'voltage' applied to the pair of gates. The original pattern (Figure 4.7(a)) represents the situation with no voltage on the gates. The next image in the series has the same pattern except with a single pixel removed from each side along the line of the gate. Figure 4.7(b) shows two simulation instances corresponding to 1 and 7 pixel depletions. The total series of simulated circuits consists of 10 images, one ungated and nine others with 1 - 9 pixels depleted. Figure 4.7(c) shows simulation results for the '2 iteration' Sierpinski circuit[4], where we have calculated the differential

---

[4]Two iterations refers to two steps through the fractal generation process from the original generator, which is a single white box surrounded by black. Each step consists of copying the generator, scaling it by 1/3, making eight copies, and translating them to surround the original pattern. The side length of the generated image is multiplied by 3 for every step, which in this case yields an image 27 pixels on a side.
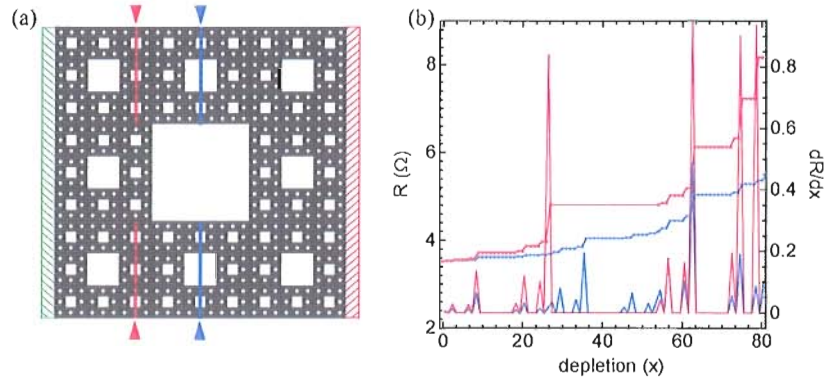
Figure 4.8. Architecture and simulation results for a 4 iteration Sierpinski circuit. The device architecture (a) has broad source (red bar) and drain (green bar) contacts on either side. The positions of the two different gate configurations are indicated with pairs of arrows, and the maximum extent of the gating is shown in matching color. The results of the circuit simulations (b) are shown in terms of resistance R (upper traces) and dR/dx (lower traces) vs. depletion x measured in pixels. The center gate (blue) and offset gate (red) configurations correspond to the appropriately colored traces.

resistance of the circuit as a function of the electrostatic depletion from the side gates.

Depleting the current-carrying channels (black pixels) causes a series of differential resistance responses whose amplitudes are, to first order, determined by the width of the remaining conducting channels, but whose frequency (in x space) is dictated by the fractal geometry of the circuit.

These simulations were repeated on the equivalent Sierpinski circuit featuring 4 iterations (Figure 4.8). The narrow gates have the same positions as before, although now they deplete over cross-sections 81 pixels in length instead of 9. The two additional iterations give this circuit 9 times the area of the 2 iteration circuit and feature sizes ranging from one pixel (the same as before) to 81 pixels. This corresponds to an additional $\sim$ 1 order of magnitude in fractal scaling over the
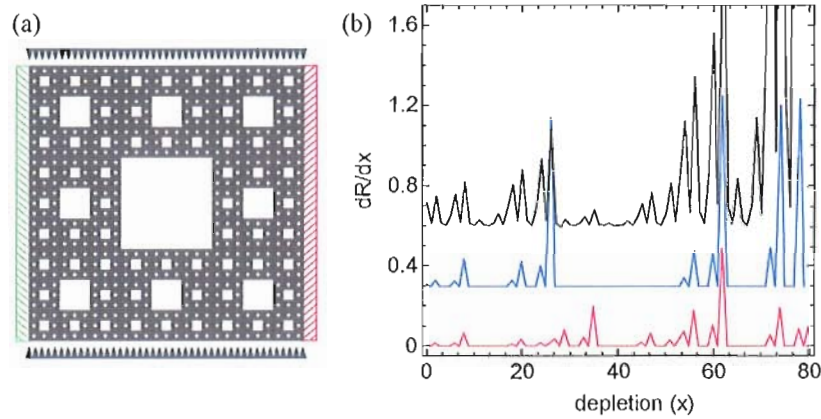
Figure 4.9. Sierpinski circuit (4 iteration) dR/dx vs. depletion for three different gates. The dR/dx curves for the offset line gate (red), centered line gate (blue), and a full width gate (black) on the 4 iteration carpet are shown in (b). The full width gate is shown in schematic (a), and is essentially a superposition of line gates at every pixel position across the pattern.

previous simulation. The frequency (in x space) of the features is once again dictated by the fractal geometry of the circuit. However, the increase in fractal scaling leads to a far more complex differential resistance response (Figure 4.8(b)).

Further complexity in the differential resistance can be induced by considering gates that address the entire width of the carpet. The results of this gate configuration on the 4 iteration carpet are shown in Figure 4.9. A full width gate is equivalent to a superposition of line gates at every pixel position across the image width, which adds significantly to the variety and amplitude of features in the dR/dx curve. The correspondence of features in dR/dx to features in the carpet can still be made without much difficulty, but the well-defined cyclic nature of the line gate curves is complicated somewhat by simultaneously depleting at all positions.
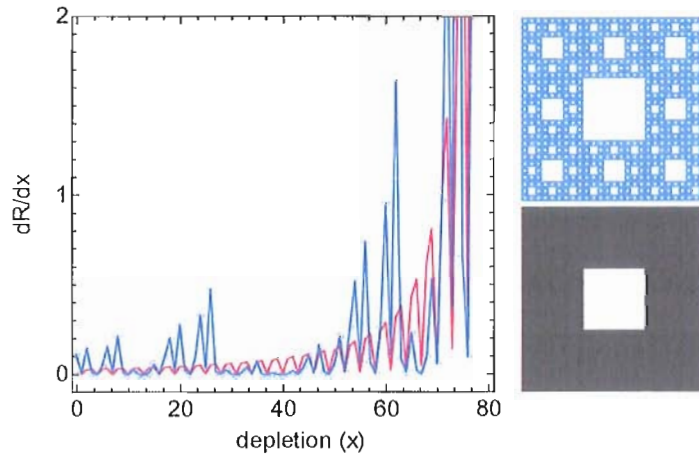
Figure 4.10. dR/dx of a Sierpinski circuit compared to a non-fractal circuit (main panel), and the corresponding patterns that formed the circuit. The Sierpinski Carpet and its dR/dx trace are shown in blue.

Finally, we consider how a non-fractal, but still finely-featured, pattern compares to these fractal patterns. There is clearly a vast variety of patterns that could be considered, but in order for the comparison to be informative, the pattern should match the large scale features of the Sierpinksi carpet. Figure 4.10(bottom right) shows a selected pattern, which retains the large central square of insulating material so that the background increase in dR/dx as the same trend compared to the 4 iteration Sierpinski circuit. The fractal structure around the central square is replaced with a grid of white, single-pixel squares. Simulated dR/dx results for each pattern are shown in Figure 4.10(main panel).

The Sierpinski circuit produces comparatively larger features in dR/dx over intervals of depletion, which translates into a more sensitive response to gating than the grid pattern circuit. Clearly, a carefully selected 'Euclidean' pattern of this type

could produce single dR/dx features in excess of the fractal, but this is largely beside the point. The interesting characteristic of the Sierpinski circuit's response is its cyclic pattern of enhanced and suppressed dR/dx over the whole range of depletions. This sensitivity (or lack of it over certain depletion regions) and its predictability may be of use in application.

The Diffusion-Limited Aggregate

In anticipation of our proposed implementation of a gated fractal circuit element, we also consider simulations of the diffusion-limited aggregate. The locations and shapes of both the electrodes and the gates can be chosen to maximize connections to the fractal circuit element. Figure 4.11 shows two possible configurations where the truncated circle drain connects many branches of a single simulated DLA pattern. Gates adjacent to the source electrode could then be used to incrementally reduce the number of connections to the drain, routing current through the remaining branches. The latter gating scheme (Figure 4.11(b)) was chosen to match the symmetry of the pattern (like the linear gates in the Sierpinski carpet), but not for its ease of implementation. Gating electrostatically around an arc would require a large number of independent gates that could be switched on sequentially, each forming a small linear part of the overall arc shape. Considering the physical size (~ 3 μm in diameter) of the proposed circuit elements, this may prove challenging to achieve. Figure 4.11(a)
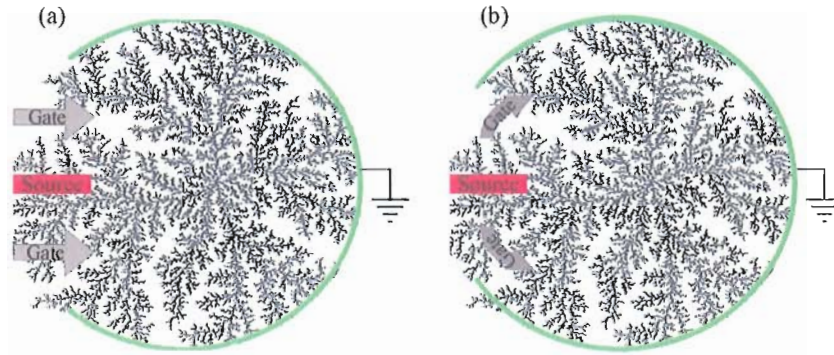
Figure 4.11. Schematics of two gating schemes for a DLA pattern. Current flows through the island from source (red) to drain (green), routed by two electrostatic gates (gray). A simpler, plunger gate system (a) and an arching gate system (b) are two possible gating implementations for this circuit.
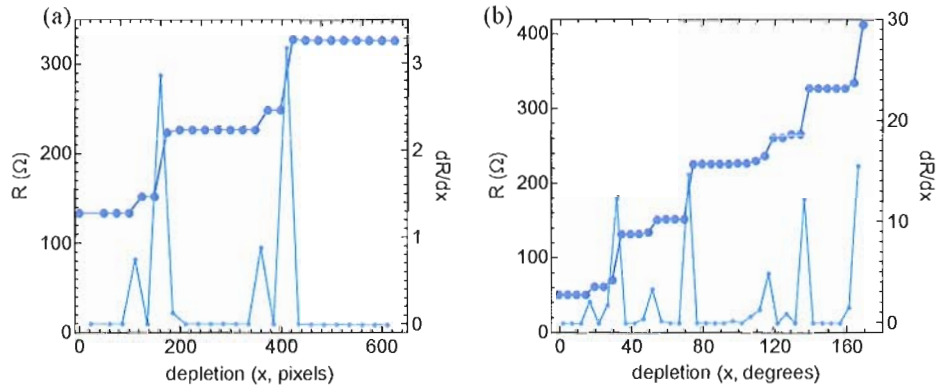
Figure 4.12. Simulation results for DLA circuits in two gating configurations with R (dark blue) and dR/dx (light blue) displayed. The labeling (a, b) is the same as for Figure 4.11.

shows a simpler implementation that sacrifices some of its ability to address as many branches of the pattern as possible.

The simulation results for these patterns are presented in Figure 4.12. The resistance and dR/dx results are reminiscent of the Sierpinski circuit curves, despite the change in geometry. This is encouraging for future device implementations in diffusion-limited aggregate-type devices. However, one consideration will be whether

the predictability of feature positions in the depletion graph is of use. Since DLA is a statistical fractal, only the statistics of the features (average number, average separation, etc) will remain constant between DLA patterns.

Atomic Cluster Aggregates as Fractal Circuit Elements

Motivated by our simulations, we focus on circuits formed from semi-metallic elements that 'self-assemble' on atomically flat surfaces via modified diffusion-limited aggregation. This self-assembly process has the advantage of minimizing the waste of material associated with traditional lithographic fabrication techniques and also enables the generation of whole arrays of complex, multi-scale structures in a single deposition step. The size, shape and fractal properties of these structures can be controlled by the growth conditions, which offers a high degree of flexibility for device fabrication. This section will discuss briefly how the patterns are currently formed, characterize their fractal properties, and outline methods for tuning the fractal properties and implementing the finished fractal electronic devices.

Experimental Background

Self-assembled, fractal patterns have previously been observed in a variety of metallic systems under varied growth conditions [79, 96–98]. Here the focus is on depositing high purity (99.998%) Sb_4 clusters on highly-oriented pyrolytic graphite (HOPG) in an ultra high vacuum, which results in highly branched Sb patterns [99].
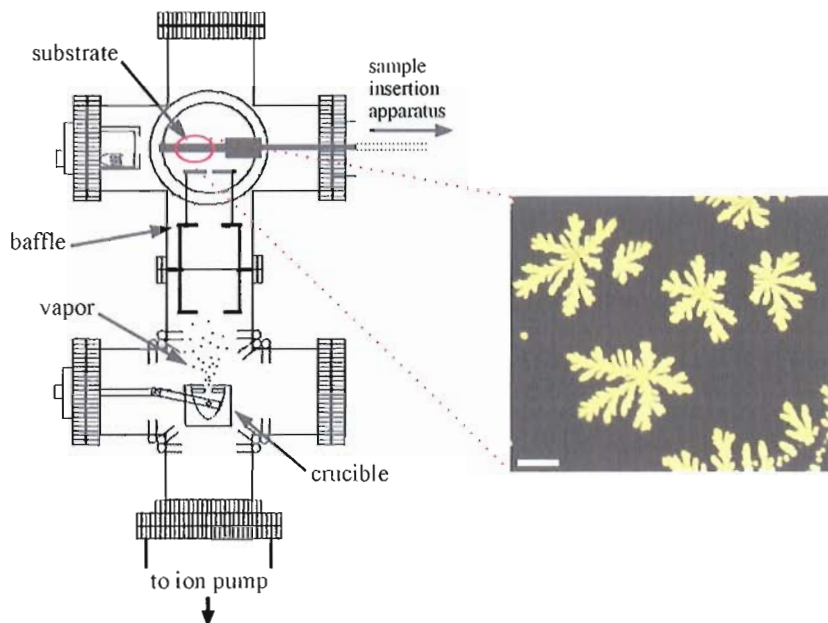
Figure 4.13. Deposition apparatus and SEM image of the Sb islands. The UHV deposition apparatus (a) is used to create islands like those shown in the SEM image (b). The scale bar $= 1\ \mu$m.

Figure 4.13(a) shows a schematic of the fabrication process, which uses thermal evaporation to generate and deposit a beam of atomic clusters on a substrate. Figure 4.13(b) shows a representative SEM image of 10 monolayer-thick[5] Sb 'islands' deposited on the substrate at a rate of 0.2 $\mathring{A}$/s. The apparatus allows control of many experimental parameters. Two that will be key to device fabrication are the substrate temperature and deposition rate for reasons that will be elaborated on later in the section.

---

[5]Note that this refers to the number of monolayers that would be found in an Sb film that uniformly covered the entire area exposed to the beam. This is a common way to measure the amount of material deposited in these experiments, and is calculated from crystal deposition monitor data.

Island Formation and Fractal Analysis

The model for the formation of these islands is based on classical diffusion-limited aggregation of the Sb particles. In DLA models, particles are released from a boundary on the substrate and diffuse freely until they encounter a fixed particle or surface. Once this encounter has occurred, the particle has its position fixed and the process is repeated. Figure 4.14(a) shows the simulated island generated from ≈ 100000 particles. This type of DLA structure has been shown to have statistical fractal properties [72].

To facilitate a visual comparison with the physical Sb islands, in Figure 4.14(c) we have traced out the edge of one of the Sb islands. A red 'backbone' pattern to highlight the coarse scale branching structure is also included. Whereas the coarse scale structure of the Sb island is visually reminiscent of the DLA simulation, the island's edge clearly lacks the simulation's fine structure. This absence of finer structure is due to two phenomena that do not occur in the classic DLA model: particle diffusion along the edge of the island and coalescence of the particles with the existing island. A simulated pattern[6] that incorporates both of these phenomena is presented in Figure 4.14(b). Additionally, this simulation allows multiple particles to impinge anywhere on the substrate (as if from a beam of atomic clusters) rather than single particles released from a boundary. By tuning the relative rates of particle deposition,

---

[6]This simulation program was written by Dr. David McCarthy at University of Canterbury. A kinetic Monte Carlo method, which uses probabilistic (nondeterministic) techniques to evolve a dynamical system. For more information, the reader is referred to [100, 101]
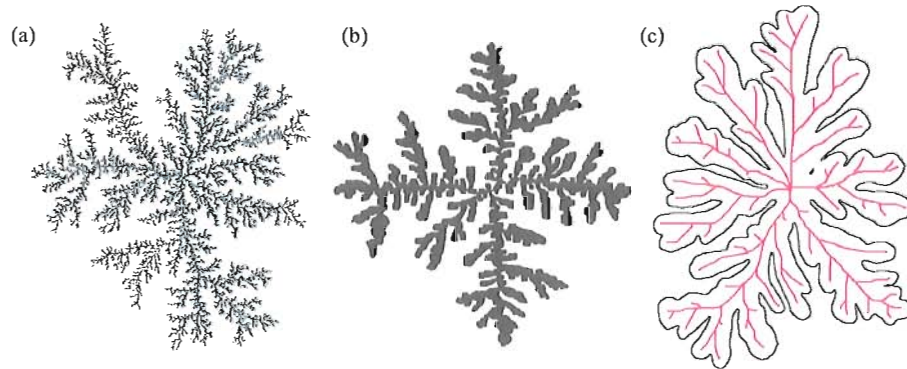
Figure 4.14. (a) A simulated DLA pattern, (b) a simulated island with edge diffusion and coalescence of clusters included in the DLA model, and (c) an Sb island with 'backbone' branching structure. The island width in (c) is $\approx 2.2\mu$m.

island edge and island 'corner' diffusion (which are energetically distinct), and island reordering (coalescence), we can simulate a continuum of island structures. These can range from highly-branched DLA-like patterns to completely compact patterns devoid of branching, e.g. approximately circular islands. The example simulation of Figure 4.14(b) shows one 'intermediate' island that is similar to the physical islands observed in Figure 4.13(b).

How *fractal* are the islands? This question is investigated by applying the box-counting method [73, 76] to the edges of the islands[7]. The results of the box-count are shown in Figure 4.15 for the three patterns of Figure 4.14. To allow direct comparisons between the size scales of the three islands, the L values are normalized using the short axis of the island, L_0.

---

[7]Note that analysis of the filled-in pattern would introduce significant error to this technique by making a large section of the analyzed image two-dimensional. Boxes in this region would always be filled, regardless of box size. Though the features of the pattern would still be captured in the box-count in this case, resolving them in log-log space with a large filled box background proves difficult.
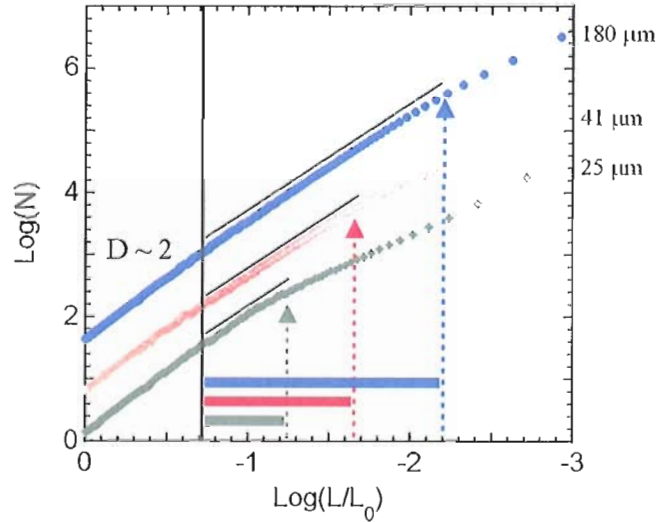
Figure 4.15. The box-counting analysis for the simulated DLA island of Figure 4.14(a) (blue circles), the modified DLA simulated island of Figure 4.14(b) (open red circles), and the physical Sb island of Figure 4.15(c) (green diamonds). The bars and arrows in corresponding colors indicate the extent of each island's fractal scaling range. In those scaling ranges, black lines indicate the $D = 1.7$ gradient. The perimeter of each pattern is also indicated at the fine scale end of the plot.

These scaling plots are important for quantifying the fractal parameters that generate the favorable functional characteristics mentioned earlier in the chapter. In particular, characteristics such as high connectivity, dispersion, and area/volume ratios all arise from the repetition of spatial structure, the extent of which is mapped out by the scaling plots. These characteristics can be enhanced by adjusting two factors. The dimension D describes how the patterns occurring at different magnifications combine to build the resulting fractal shape. Since D corresponds to the gradient of the scaling data, it charts the rate at which structure in a pattern is magnified: a high D value corresponds to a higher rate, which leads to a higher ratio of fine to coarse structure in the pattern. The second factor is the magnification

range over which this fractal scaling occurs and this is set by coarse and fine scale cut-offs.

The scaling plots of Figure 4.15 allow an investigation of how the differing growth conditions of the islands of Figure 4.14 affect their D values and their magnification ranges. The D value for the simulated island of Figure 4.14(a) matches the well-established value for DLA of 1.7 [72]. This scaling 'rate' is preserved for all three islands, indicating that the changing growth conditions have not modified the basic particle dynamics of the fractal generation process - all three islands are formed from a DLA process. However, the changing growth conditions have reduced the magnification range over which the DLA operates, as illustrated by the colored bars at the base of the scaling plot. This corresponds to a gradual suppression of fine scale branching by edge diffusion and cluster coalescence. To emphasize the importance of this reduction of magnification range on functional properties, the perimeter lengths of the three islands are noted in Figure 4.15. The perimeter of the pure (simulated) DLA island of Figure 4.14(a) has a perimeter of 180 μm, reduced to only 25 μm through fine-structure suppression. This reduction will directly impact, for example, boundary to area ratios and also the number of branches available for connections, both of which are potentially useful generic properties for circuit designs.

The Sb island of Figure 4.14(c) scales over approximately 0.5 orders of magnitude, perhaps too small a range to be considered fractal [102, 103]. For our proposed fractal electronic devices, it is therefore informative to consider the potential for increasing

the fractal scaling region. Fortunately, it has been shown that the island growth conditions can strongly affect the structure of the islands, for example by increasing the deposition rate [99]. With further tuning of these growth parameters as well as cluster size [97] and substrate temperature [104], the islands will develop finer structure. This decrease of the fine scale cut-off and associated increase of the fractal scaling region will improve the effectiveness of the islands as fractal electronic circuit elements. Note that the fundamental minimum for feature size is set by the size of the impinging clusters (< 1 nm in the case of Sb_4), though in practice this limit will be difficult to achieve.

Fractal Scaling Enhancements

The fractal scaling range can be extended by increasing the coarse scale cut-off, achieved by growing larger islands (as measured by the island diameter L_0). Depositing more material, as shown sequentially in Figure 4.16(a,b,c) for 5 monolayers (ML), 10 ML, and 40 ML respectively, results in larger, more branched structures. However, when considering island size, it is important to remember that there are physical constraints on both the minimum and maximum values of the island diameter L_0. The minimum value is of interest for applications that may require large packing densities. The minimum size of a *branching* island is dictated by the so-called 'critical radius' (r_c) of the island. r_c is the size at which an island will transition from a compact, circular shape to a branched structure. This transition changes the
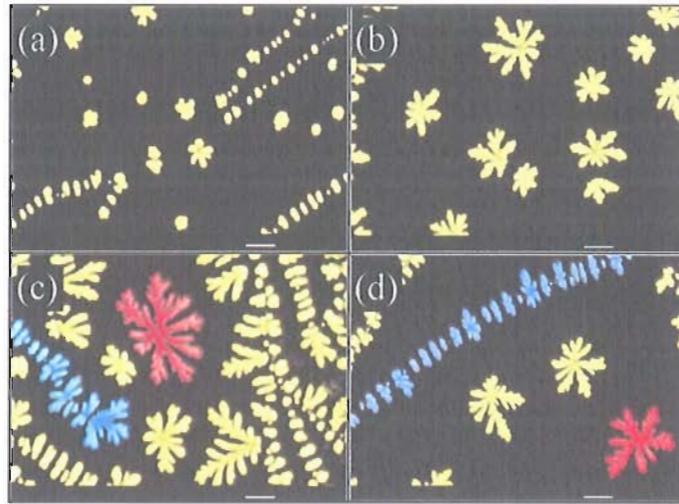
Figure 4.16. Comparing the SEM images in (a), (b), and (c) demonstrates the growth of the islands at a constant (0.03 Å/s) deposition rate with 5, 10, and 40 effective monolayers on the substrate respectively [99]. The images in (c) and (d) show the two types of structure nucleation: at point defects (examples colored red) and step edges (examples colored blue). Scale bars = 1μm.

mathematical relationship between the perimeter of the island and the area that it encloses and can therefore be determined by the analysis shown in Figure 4.17 [96]. The knee in the data shows a transition from circular island geometry (with a smooth perimeter of $D = 1$) to a branched structure (with a perimeter of $D > 1$) at 0.3 μm. This minimum island size can be decreased significantly by depositing material at a faster rate [99].

The maximum island size is set primarily by the distance between neighboring islands. Since islands nucleate on locations of 'roughness' on the substrate surface (e.g. point defects and step edges), the maximum island size can be controlled by the distance between surface features. Figures 4.16(c) and (d) show examples of point defect nucleation (examples are highlighted in red), which produces roughly
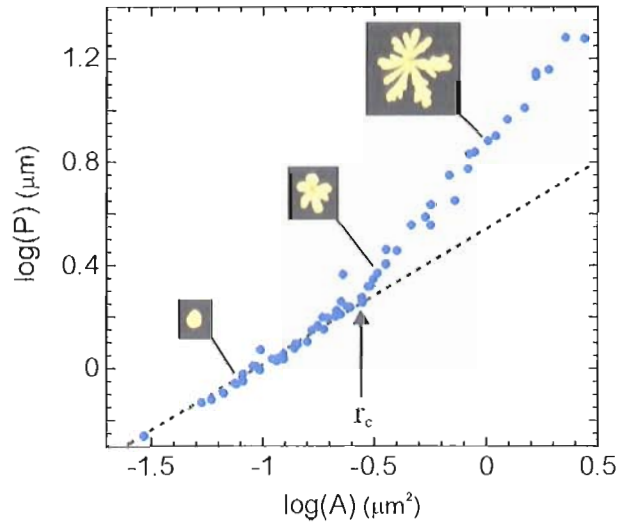
Figure 4.17. Island perimeter vs. island area showing the critical branching radius on log-log axes. Each data point represents an individual island. All islands, of varying sizes, are grown under identical conditions. The dotted line is a guide to the eye, showing the behavior expected for purely Euclidean (ellipsoidal) islands. The critical radius (r_c) represents the point at which the data deviates from this behavior, indicating the formation of branches. Perimeters and areas were measured from SEM images.

symmetric islands, and step edge nucleation (examples are highlighted in blue) which promotes growth radiating from the edge. The ability to manipulate surface features will also be central to future circuit designs: for example, for connecting the islands between source and drain electrodes. Focused ion beam (FIB) milling may be useful for precise patterning, since FIB features have previously been shown to act as artificial nucleation sites for the islands [105]. Standard lithography techniques can also be used to define boundaries restricting the islands to selected substrate regions so that they do not merge with other circuit components.

A final practicality involves the substrate material. HOPG is currently used by Professor Brown's group, which is a conductor ($\approx 4 \times 10^{-7}$ $\Omega \cdot$m) in the plane

parallel to its surface. This is certainly problematic for studying the islands as elements in electrical circuits. Mica is a possible alternative substrate material, because of its low surface defect density and insulating properties. However, the electrostatic and crystalline properties of its surface may not be ideal for observing the cluster diffusion necessary to create DLA-like structures. The cleavage plane of muscovite mica contains randomly distributed K^+ atoms, giving the surface a polar character and perhaps interfering with cluster diffusion [106]. Also, the lattice mismatch between mica and typical metallic materials is $\sim 10\%$ compared to $\sim 50\%$ on HOPG, which will increase the substrate-cluster interaction, also inhibiting free diffusion [107]. Alternatively, the adhesion of the fractal islands to the HOPG surface is quite weak [97], which may enable post-deposition transfer of the islands from the original HOPG substrate to a more strongly attracting insulating substrate.

Conclusions

Fractal geometry is prevalent in a wide variety of natural and manufactured devices and provides many functional advantages over more conventional, Euclidean systems. Electrical simulations demonstrate that novel, non-linear transport behavior can be generated from circuit elements with fractal geometry. Furthermore, increasing the fractal scaling range of the circuit increases the complexity and extent of these non-linearities. We propose extending fractal geometry to micron-scale electronic

circuits and using self-assembled nanocluster aggregates as a platform for such studies. The growth dynamics of these aggregates can be adjusted to tune the 'strength' of their fractal characteristics, which should allow a detailed experimental study of how the extent of fractal scaling affects carrier transport.

CHAPTER V

TUNNELING TRANSPORT IN QUASI-1D NANOPARTICLE ARRAYS

Introduction

The nanoparticle arrays investigated in this chapter were designed as a next step

from the few element limit of the electron billiard system to a quantum system with

hundreds or perhaps thousands of individual elements. As mentioned in Chapter

I, the analogy between the two systems was based on calculations that place gold

nanoparticle arrays with total length = 200 nm and nanoparticle diameter = 3.5 nm

in a similar carrier transport regime as the electron billiards. This transport regime

(the 'semiclassical' regime) requires phase-coherent electron transport as well as a

Fermi wavelength (λ_F) that is a small fraction of the array element size. In the

electron billiard arrays, the phase coherence length, l_ϕ, ≈ 6 μm or between 2 and 6

times the linear extent of the array. In gold, measured l_ϕ values at ≈ 300 mK range

from 3 to 12 μm [108, 109], which are far in excess of the nanoparticle array length.

The λ_F to nanoparticle diameter ratio (0.5 nm to 3.5 nm) is within a factor of 3

compared to the electron billiard's ratio (35 nm to 750 nm)[1]

These simple calculations are encouraging, but transport through the nanoparticle

---

[1]This result assumes a carrier density $= 5.9 \times 10^{22}/cm^3$.
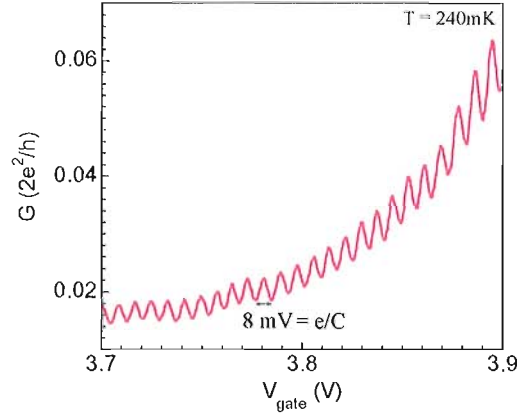
Figure 5.1. Coulomb blockade oscillations in an electron billiard. The period of the oscillations is labeled, and corresponds to the classical charging energy necessary to add an electron to the blockaded billiard.

arrays is dominated by the Coulomb blockade effect at low temperatures. Coulomb blockade occurs in systems where tunnel barriers (often referred to as tunnel junctions) separate the conducting elements from the source and drain electrodes. This results in a 'blockade' of current until a tunneling electron can pay the classical charging energy price of the conducting element (island), which set by its capacitance. The effect can be observed in electron billiards by pinching off the quantum point contacts to create tunnel barriers between the 2DEG and the device. Figure 5.1 shows an example in the weak tunnel barrier regime, where there is a small background tunneling current in addition to the Coulomb oscillations.

In the nanoparticle arrays, the tunnel barriers are formed by the insulating ligand shells on each gold nanoparticle that prevent them from clumping together in solution. This consequently places all transport between array elements in the tunneling regime,

which is quite different than the default electron billiard configuration. As our experiments will demonstrate, this has profound effects on electron transport in the nanoparticle arrays, and is an important consideration for future experiments with these devices.

This chapter will briefly cover the theoretical underpinnings of our experimental results, detail our experimental efforts to fabricate and electrically characterize these nanoparticle tunnel junction arrays, and finally offer a perspective on future experiments for realizing our original research intent.

Transport in Arrays of Tunnel Junctions

This section will present the background for the experimental and analytical details of the following sections. Building on the behavior of a single Coulomb-blockaded metallic island, a brief account of the Coulomb-blockade in many junction arrays will be presented. Finally, a review of the relevant contemporary literature in experiment and modeling will complete the necessary basis for understanding our experiments and analysis. For further reading and more detail, the reader is referred to the citations in the following pages and also some excellent reviews of Coulomb blockade phenomena [110, 111].

Theory of Coulomb Blockade

For the barrier-metal island-barrier system shown schematically in Figure 5.2(a), one's expectation would be for electrons to tunnel from the lefthand electrode to the island and subsequently to the righthand electrode. This would depend on the barrier height, barrier width, and various material parameters. In practice, there is one more, very important consideration: the Coulomb charging energy of the island. This is a classical effect, but manifests itself in the energy spectrum of the island as a gap $= 2 \times \dfrac{e^2}{2C}$, one multiple of the classical charging energy for the electron, and one for the corresponding hole as shown in Figure 5.2(b).

In this case, there is no longer a state in the island at the Fermi energy, E_F, and so current will not flow from one electrode to the other. To induce current to flow, there must be either an applied bias between the two electrodes or the energy levels of the island must be shifted until an energy level is in resonance with E_F, perhaps by a biased gate near the the island. The first of these two situations is shown in Figure 5.2(c). In the case of an applied bias between the source and drain electrodes, once the source chemical potential μ_s is raised at least $\dfrac{e^2}{2C}$, carriers can tunnel freely from the source to the island and to the drain (see Figure 5.2(d)). Increasing the bias increases the rate of tunneling and hence electrical current, since an increasing number of island states become available for transport. The bias required to overcome blockade is called the threshold voltage, V_t, and the ideal case has the I-V behavior shown in Figure 5.2(e).
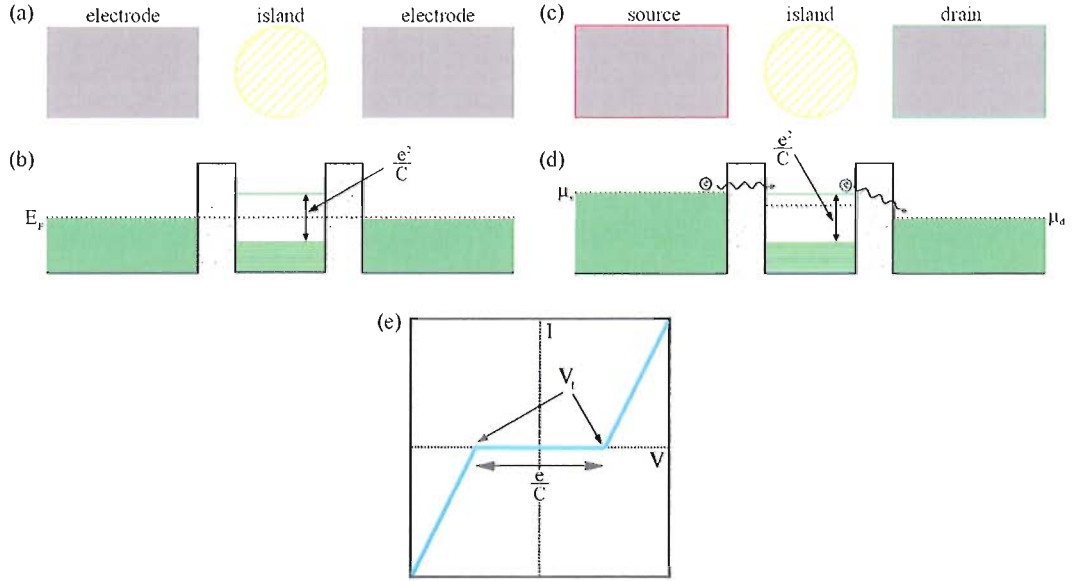
Figure 5.2. Coulomb blockade in a single metallic island. A schematic of the model system (a) has the energy level diagram shown in (b). The island is assumed to be small enough to have a discretized energy spectrum as depicted. An applied bias between the source and drain electrodes (c), suppresses the blockade once the source chemical potential μ_s is raised by $e^2/2C$ (d). This corresponds to the region of (e) above V_t. The result of blockade on the island's current-voltage characteristic is shown in (e).

By instead adjusting the island's energy with a gate (see Figure 5.3(a)), the island can be shifted on- and off-blockade as a function of gate potential, V_g. Formally, the electrostatic energy of charge Q on the island can be represented by

$$E = -QV_g + \frac{Q^2}{2C} = (Q - Q_0)^2/2C + f(V_g, C) \tag{5.1}$$

where C is the capacitance between the island and all the components of the system, and $Q_0 = CV_g$. In the second expression, $f(V_g, C)$ is an additive quantity that is independent of Q. As V_g (and hence Q_0) is changed, it shifts the allowed charge states between two extrema. In the first (Figure 5.3(b)), $Q_0 = Ne$ and an integer
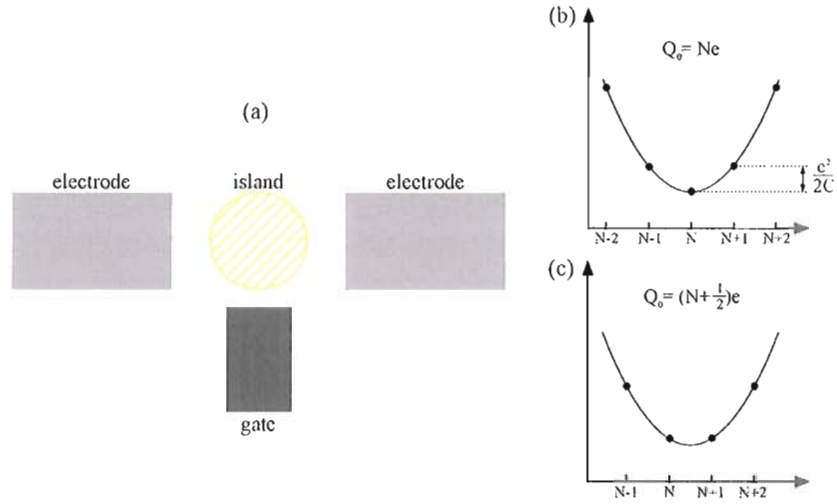
Figure 5.3. The Coulomb blockade effect in a gated single island. A schematic geometry (a) has an energy level diagram like Figure 5.2(b). By shifting the gate voltage V_g ($= Q_0/C$), the energy level spectrum of the island moves cyclically between two states depicted in (b) and (c). See main text for details.

number of electrons minimizes E. This results in the usual $\dfrac{e^2}{2C}$ energy gap and the island is on-blockade. However, when $Q_0 = (N + 1/2)e$, the energies for the island having N electrons and $N+1$ electrons are degenerate and the island is off-blockade. In practice, sweeping V_g will result in a series of peaks in the device conductance, separated by e/C, the voltage required to shift $Q_0 = (N+1/2)e$ to $Q_0 = (N+3/2)e$. This model [110, 112] does not explicitly account for finite temperatures, however the intuitive expectation - that the conductance peaks will shift from zero T delta functions to peaks with width $\propto k_B T$ - is correct.[2]

The situation is further complicated by islands (such as ours) small enough to have energy level spacings $> k_B T$, however this instance will not be of concern to our experiments. Single island and island array gating and the discretized energy

[2]Specifically, the line shape becomes $G/G_{peak} \sim cosh^{-2}(1/k_B T)$ at finite T [111]
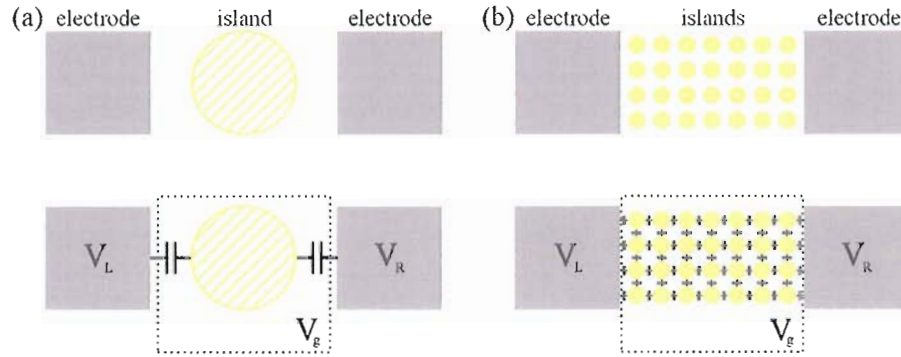
Figure 5.4. A single island (a) vs. an array of islands (b) in the tunneling regime. V_L, V_R, and V_g are the voltages on the left and right electrodes and a gate. Each island is capacitively coupled to the surrounding islands, the electrodes, and the gate.

spectrum of the gold nanoparticles will likely play a role in future experiments. These will be discussed later in the chapter.

Coulomb Blockade in Tunnel Junction Arrays

In view of the expected geometry of our nanoparticle arrays, i.e. a 1D or nearly 1D chain of spherical gold particles aligned along a DNA molecule's backbone [113, 114], it is important to review how the physics of a single pair of tunnel junctions translates to many element arrays of tunnel junctions. The situation is illustrated in Figure 5.4. The electrostatic energy of an arbitrary charge configuration can be calculated (somewhat arduously) after [115] by assuming that all the inter-island capacitances are identical. This model neglects the presence of any gates and assumes a very high degree of uniformity within the tunnel junction array. These constraints are appropriate for some situations [116], but the nanoparticles in our arrays are somewhat poly-disperse (i.e. of varying size), making a model introduced by [117]

more appropriate. That model's general expression for the array's electrostatic energy,

$$E = \frac{1}{2}\sum_{i,j}(Q_i + q_i)C_{ij}^{-1}(Q_j + q_j) + V_L Q_L + V_R Q_R + \sum_i V_i^{ext}Q_i \qquad (5.2)$$

is an extension of Equation 5.1, summing over all the islands in the array. The notation is defined as follows: Q_i is the charge on the i-th island. V_L (Q_L) and V_R (Q_R) are the voltages (charges) on the left and right electrodes respectively. C_{ij} is the capacitance matrix for the array whose diagonal contains the sum of all capacitances associated with the dot and off-diagonals are the negative of the interdot capacitances (capacitance between i-th island (row) and j-th island (column)). V_i^{ext} is the voltage on the i-th island due to elements 'external' to the array, i.e. the left and right electrodes and gate, and $= \sum_x C_x \sum_j^x C_{ij}^{-1}V_x$ where $\sum_j^x$ is a sum over islands j that neighbor the electrode $x = L, R, g$.

This description is nearly equivalent to [115] and makes similar approximations to make subsequent calculations, assuming a constant capacitance C between islands and a constant capacitance C_g between each island and the gate. The most important addition is including *disorder* in the form of a randomized, offset charge q_i, which represents an effective charge on the i-th island due to nearby, static, charged 'defects'. This is a continuous variable, since the distance from defect to island can vary continuously. It is assumed that $0 < q_i < e$, since mobile electrons should be able to compensate for local defects in integer multiples of e. Though this model of disorder doesn't specifically treat the case of varying island size (varying C_{ij}), it has a similar effect in that shifting C_{ij}'s will also offset the energy barriers on each island.

Thinking in terms of a single island (Figure 5.4(a)), an offset charge of this sort would shift the energy necessary to move a charge on to the island (eV_t). Extending this to an array of many islands, the effect of this type of disorder would be to randomize the Coulomb energy barriers of each island. An applied bias to the left electrode less than V_t for the array overcomes a fraction of the energy barriers in adjacent islands. Increasing the applied bias overcomes a larger fraction of barriers until eventually V_t is reached, meaning that there is at least one continuous path of off-blockade islands from source to drain. Raising the bias beyond V_t simply adds more and more paths until (eventually) all of the islands' energy barriers are overcome, and the I-V characteristic resembles that of a single off-blockade island.

However, it generally takes a high bias to accomplish this last situation, and research [117] has found that in the intermediate region between threshold and entirely off-blockade,

$$I \sim (\frac{V}{V_t} - 1)^\zeta \tag{5.3}$$

where ζ takes on the values of 5/3 and 1 for 2D and 1D arrays respectively. In the 2D case, the exponent is calculated using the Kardar-Parisi-Zhang interface model [117, 118], where in this case the interface is defined by how far a mobile charge can move toward the drain electrode for a given V. In the strict 1D case, there is only one pathway from source to drain, meaning that as soon as $V = V_t$, all islands are necessarily off-blockade, and the behavior reverts to the single island (linear response) case. In combination with the prediction that $V_t(T = 0) = \alpha Ne/C_g$ in the limit $C \ll$

C_g, the model sets out a good picture for the zero-temperature I-V characteristics of tunnel junction arrays[3].

Two of this model's limitations, namely the requirements that the thermal energy is much less than the charging energy and the inter-island capacitances are much less than an island's self-capacitance ($C \ll C_g$), are addressed by a recent extension [119]. The main results of this extension are a derivation of the dominant V_t temperature trend,

$$V_t(T) = V_t(0)[1 - p(T)/p_c] \approx V_t(0)[1 - 2bk_BTP(0)/p_c] \qquad (5.4)$$

inclusion of nearest-neighbor, inter-island capacitive coupling, and the prediction that the power-law onset (Equation 5.3) will remain unchanged[4]. Particularly relevant to our experiments are the first and last of these accomplishments. The first (analytical) expression in Equation 5.4 states that V_T will be suppressed from its zero temperature value ($V_t(0)$) as the ratio of $p(T)$ and the percolation threshold p_c, which are the fraction of tunnel junctions with no Coulomb barrier at temperature T, and the minimum fraction of junctions with no Coulomb barrier that guarantees a continuous path of junctions from source to drain. This is illustrated conceptually in Figure 5.5. Starting at zero T (a), when the array has a distribution of Coulomb barriers (ΔE) set by randomly distributed background charges, raising T gradually overcomes a

---

[3]N is the number of elements in the length of the tunnel junction array, and α is a factor dependent on the array dimensionality, $= 0.5$ for 1D and $= 0.338(1)$ for a 2D square lattice.

[4]The complexity and extent of the analytical and numerical calculations that form the basis of this extension are significant and will thus only be covered briefly here. The interested reader is referred to the relevant research papers [8, 119]
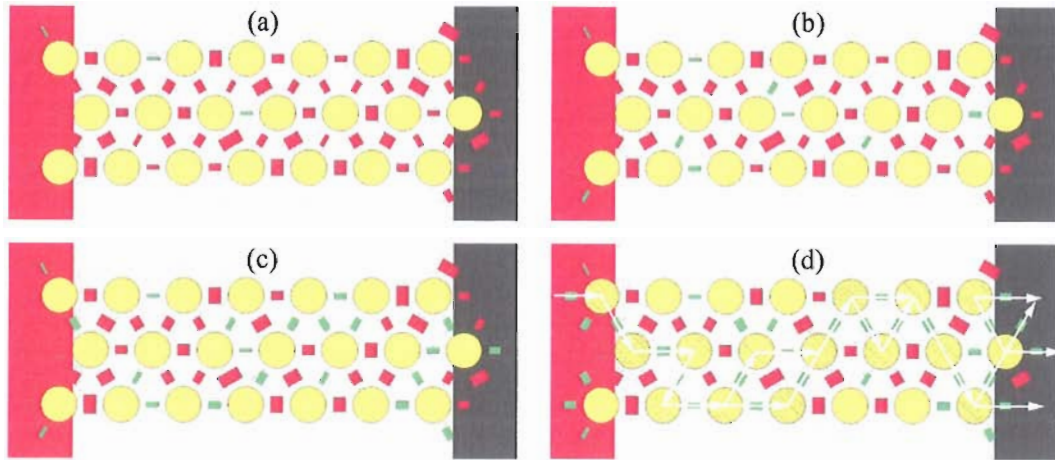
Figure 5.5. An illustration of percolation on a nanoparticle junction lattice. Coulomb barriers on each junction are randomly distributed at zero temperature in (a), fractions of which are overcome by increasing k_BT energy broadening (b, c). $V_t \to 0$ when there is a path (highlighted) with zero energy cost connecting source and drain (d). Red (green) rectangles represent (un)blockaded junctions, and the width of the rectangles represent the magnitude of the Coulomb barrier.

larger (Figure 5.5(b)) and larger (c) fraction of the Coulomb barriers until a single path connects source and drain (d) at p_c.

Assuming a relatively flat distribution of ΔE's in the tunnel junction array, $p(T)$ can be approximated by $2bk_BTP(0)$ (Equation 5.4), where b and $P(0)$ are geometry-dependent constants. Specifically, bk_BT is a measure of the thermal broadening of states above and below E_F in each nanoparticle. Since the tails of the state must be $\approx k_BT$, $b \approx 2$ is a reasonable assumption. The exact value of $b = 1.2$ [119] depends on the density of states in an island (nanoparticle). $P(0)$ is a factor that depends primarily on the ratio of the inter-island capacitance and the total capacitance of an island, and is thus dependent on the nanoparticle and array geometry, but independent of the uniformly random background charges.

The model was developed to extend the zero temperature model developed in [117], and was validated directly [8] and via comparison to experiments in the literature [120, 121]. Because our devices are analogous to these, the model's predictions are expected to apply to our results. The quality of agreement is analyzed later in this chapter.

Nanoparticle Device Fabrication and Architecture

The fabrication of the gold nanoparticle arrays was done in collaboration with the Hutchison Lab in the University of Oregon Department of Chemistry, specifically with Dr. Greg J. Kearns, Dr. Tatiana Zaikova, and Dr. John Miller. Details of the chemical processes used to form the nanoparticles can be found in G. J. Kearns' dissertation [122]. A brief summary of these processes will be presented here in addition to a more detailed treatment of the lithography techniques I employed to create the electrodes contacting the nanoparticle arrays. Lastly, the process for depositing the devices on the electrodes will be presented.

Nanoparticle Synthesis and Characterization

Precursor Au nanoparticles with tetraoctylammonium bromide (TOAB) ligand shells were prepared as detailed in [123], resulting in a deep red solution that is stable for periods ≥ 1 year if stored properly. In order to bind to the anionic backbone of the λ-DNA template molecules, these nanoparticles must be given a

cationic ligand shell. A thiocholine (N,N,N-trimethylaminoethanethiol iodide) ligand, which is known to produce close-packed nanoparticles along the DNA strand [113], was used for our devices. The TOAB ligand was replaced with the thiocholine via a biphasic ligand exchange reaction at room temperature as detailed in [122, 124]. After this process, the nanoparticles were characterized via ultraviolet-visible (UV-Vis) spectroscopy and transmission electron microscopy (TEM) to confirm that the appropriate Au particle diameter was achieved. For the nanoparticles in our devices, UV-Vis confirmed the presence of nanoparticles greater than 2 nm in diameter. TEM image analysis indicated a mean core diameter of 3.5 nm ±1.2 nm with a ligand shell ≈ 0.7 nm in thickness. The stability of these nanoparticles is not well-measured, but is less than that of the precursors. The nanoparticles show some coalescence in solution over a period of a few weeks and sensitivity to extended periods of electron beam irradiation. However, the electrical characteristics of the resultant devices are consistent over the course of the experiment ($\sim$ 1 week), suggesting little degradation over that time scale.

Electrode Construction

In order to electrically interface with nanoscale devices like these nanoparticle arrays, there is generally a need for more 'macro-scale' contacts. Many fabrication techniques deposit the nanoscale objects on the substrate first, e.g. semiconductor nanowires or carbon nanotubes, and use electron beam lithography (EBL) to 'draw'

electrodes to the nanodevices' positions. The process is reversed for our nanoparticle arrays. In addition, the ability to form our narrow nanoparticle arrays reliably is influenced by the electrode geometry, and thus considerable care must be given to electrode construction.

An issue of primary importance is to achieve electrical isolation of the nanoparticle arrays. To this end, we use silicon wafers that have a thick (3 μm) thermal oxide grown on the surface. A back-of-the-envelope calculation using SiO_2's worst-case bulk resistivity, 10^{14} Ω·m, ideal contacts, etc, etc, estimates the minimum resistance path to 'short' the device to be $\sim$ 10 TΩ. This estimate gives a reasonable expectation of effectively complete electrical isolation from the Si substrate and between the electrode pairs with no connecting nanoparticle array. Experimental results confirm this, and in fact suggest that the estimate for the minimum resistance path is quite low.

Starting with these thick oxide wafers, the lithography process to produce finished electrodes is as follows. Photolithography is the first step (Figure 5.6). Beginning with the bare wafer, a photoresist layer (Shipley 1818) is spun on and exposed to UV radiation through a mask pressed to its surface. The substrate is then submerged in a developer chemical (Microposit 351) that strips away the portions of the photoresist layer previously exposed to UV. After baking the remaining photoresist to make it relatively insensitive to heat and light, a metal bilayer $(Cr/Au)^5$ is evaporated over the

---

[5]Chromium (3 nm) is required to make the gold layer (50 nm) stick to the SiO_2 substrate. Without it, the gold can easily be scraped off with a fingernail.
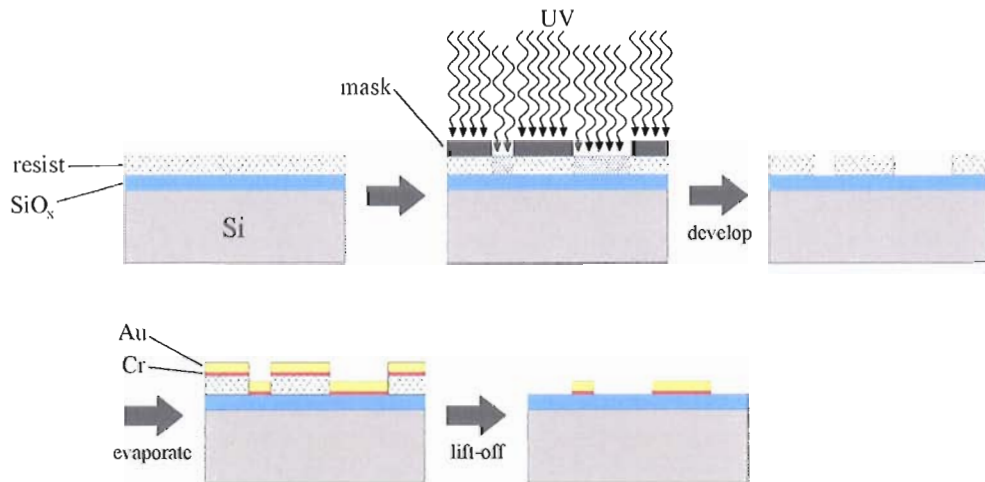
Figure 5.6. A step-by-step schematic of the photolithography process. See text for details.

entire pattern. The substrate is then placed in an acetone bath for ~ 12 hours, during which the acetone eats away the photoresist underneath the unexposed portions of the film. This results in (ideally) everything except the desired pattern 'lifting off'. This waste material can be washed away with a stream of acetone and/or mild ultrasonication.

A similar process is followed for EBL (Figure 5.7). The substrate, with finished photolithography-defined electrodes, is first cleaned and then spin-coated with an electron beam resist, polymethyl methacrylate (PMMA) 950 at 3% concentration. The resist layer is then hard-baked to drive off the polymer solvent. At this point, the substrate is placed on a scanning electron microscope stage and the desired pattern is exposed by rastering the 20 kV electron beam over PMMA layer.[6] The exposed

---

[6]Though the raster process is itself computer-automated, preparation of the substrate (cleanliness, selection of PMMA weight and concentration, PMMA layer thickness) and preparation of the electron beam (quality of focus, correction for variable lens and aperture alignment effects,
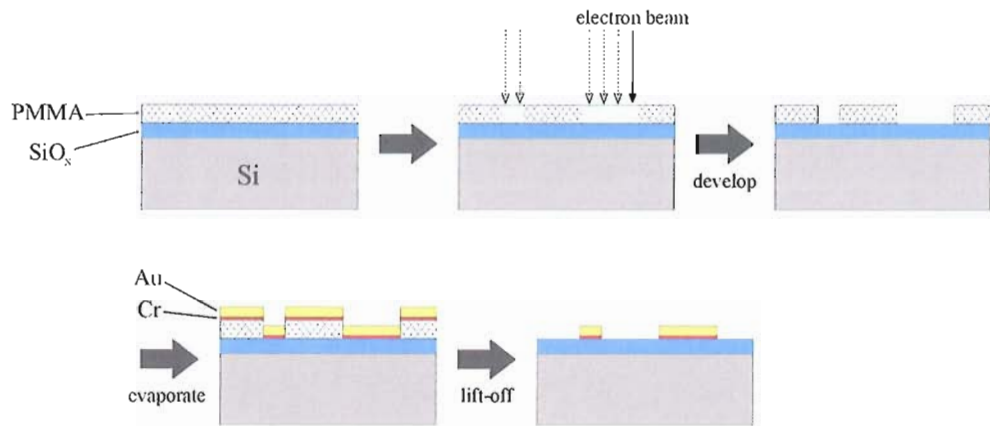
Figure 5.7. A step-by-step schematic of the electron beam lithography process. Dotted arrows indicate past postions of the beam as it is rastered over the surface. See text for details.
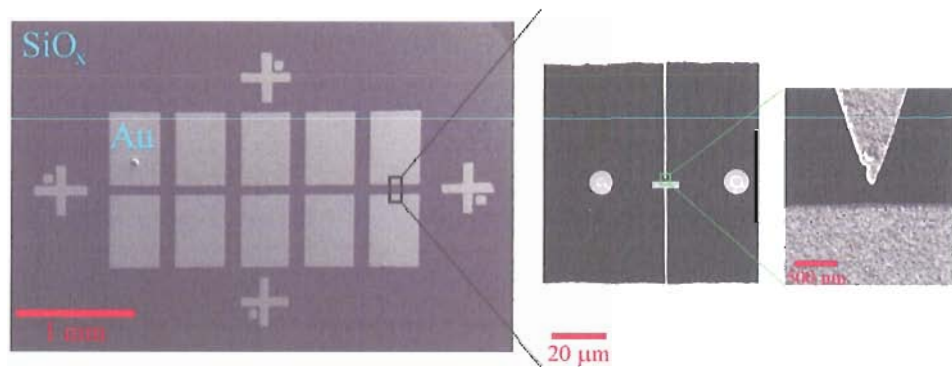
Figure 5.8. Scanning electron microscope images of a set of electrode pairs (a), a zoom-in of a single pair (b), and a detail image of the electrode gap (c), which is ≈ 200 nm wide.

pattern is then stripped away in a solution of MIBK:IPA (1:3). The final steps (evaporation and lift-off of the metal layer) to create electrodes with a ≈ 200 nm gap are the same as with the photolithography process. Figure 5.8 shows a set of finished electrodes (a) and more detailed images ((b) and (c)) of a single pair.

---

choice of accelerating voltage, measurement of beam current) are nontrivial processes. Details will be left on file with Professor Taylor's laboratory.

Device Completion

The outline of the fabrication process is illustrated in Figure 5.9. Figure 5.9(a) shows a schematic representation of the electrode pair array geometry. The array of parallel pairs of electrodes enables the deposition of multiple devices in a single step, which is both useful for measurement purposes and perhaps for future application. The surface is silanized to adjust the hydrophobicity of the surface appropriately and drawn at ≈ 0.35 mm/s from a solution containing λ-DNA (Figure 5.9(b)). The DNA are aligned along the axis of the electrode pairs by the meniscus at the solution-substrate interface. The concentration of the DNA is tuned such that on average a single DNA strand will span each pair of electrodes, i.e. ≈ 1 DNA strand per 1 μm^2 area of the substrate.

The substrate is then rinsed with nanopure water and floated face-down in a solution containing the thiocholine-stabilized Au nanoparticles (Figure 5.9(c)) at high concentration. The nanoparticles preferentially adhere to the DNA backbone via electrostatic interaction and close-pack along its length. The face-down orientation reduces the number of nanoparticles that errantly adhere to other parts of the substrate, perhaps due to quenched charges associated with substrate defects or contamination. After a thorough rinsing with nanopure water and N_2 blow-dry, the devices are complete. Ideally, they would have a single strand, 1D character like the schematic in Figure 5.9(d), but in practice come out in a variety of quasi-1D configurations (Figure 5.9(e)) that likely consist of one to several DNA strands
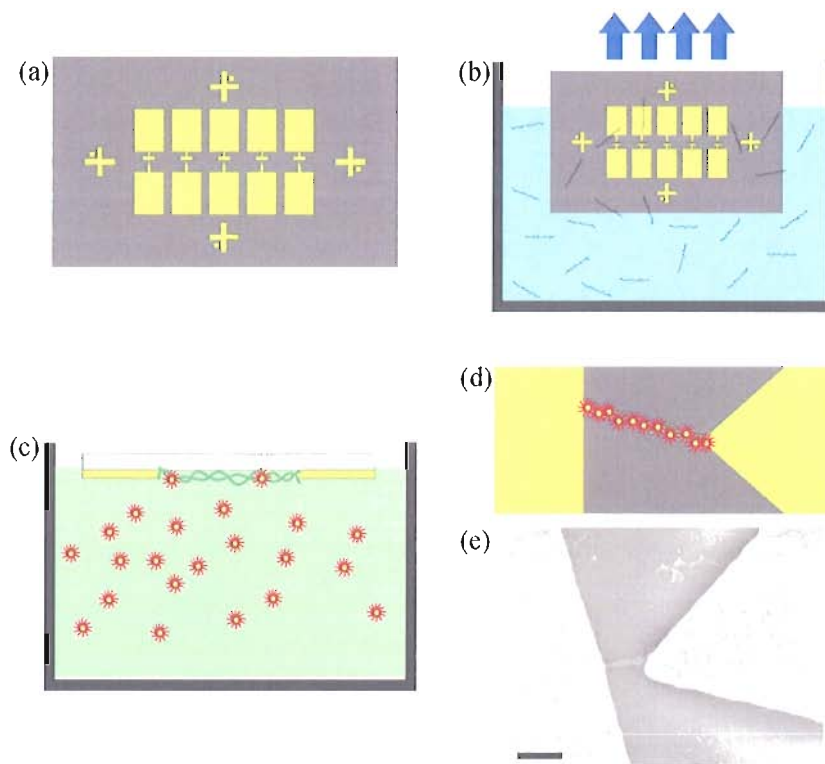
Figure 5.9. Schematics of the process steps for completing the nanoparticle devices (a-d), and an SEM image of a completed device (e). See text for process step details. The scale bar in (e) = 200 nm.

bundled together. Figure 5.9(e) shows an SEM image of an example where ~ 4 strands

bundled together best explain the width of the array (≈ 20 nm).

<u>Electrical Measurements</u>

The Experiment

A large number of potential devices were measured on a room temperature setup,

both in air and in vacuum, for testing purposes prior to the measurements described

below. These tests were performed by Dr. G. J. Kearns and myself as a simple method
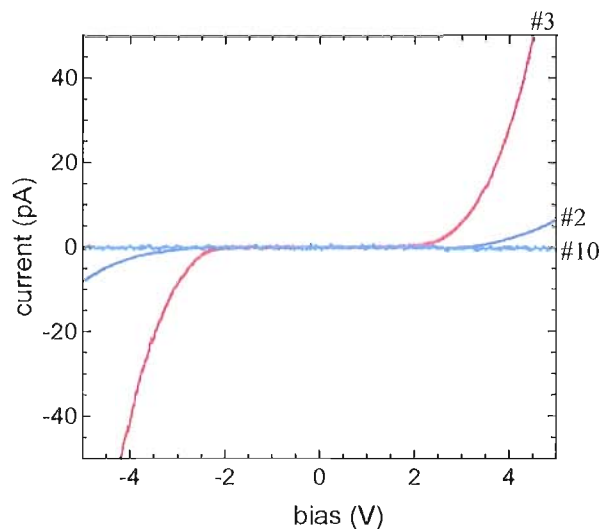
Figure 5.10. Preliminary current-voltage curves for the three electrode pairs at 240 mK.

to determine the presence of nanoparticle arrays between a given pair of electrodes[7].

The measurement circuit was similar to the cryostat measurement circuit for these devices (see Figure 2.3), with the voltage source, pre-amp, and multimeter replaced by a Keithley 236 source-measure unit.

One set of completed devices was mounted on the cold finger of the ^{3}He cryostat with silver epoxy and three pairs of electrodes were contacted via ultrasonic wire bonding. The measurement setup is shown in Figure 2.3. Sourcing voltage, I-V curves were taken at 240 mK to establish the presence of nanoparticle arrays between each electrode pair. The results of these tests are shown in Figure 5.10. Two out of the three contacted devices (#2 and #3) passed detectable current. #10 passed

---

[7]Dr. Kearns also used the in-vacuum configuration of this setup to measure a series of devices at room temperature. Intriguingly, one particularly narrow device exhibited Coulomb blockade at room temperature. The reader is referred to [122] for more detail.
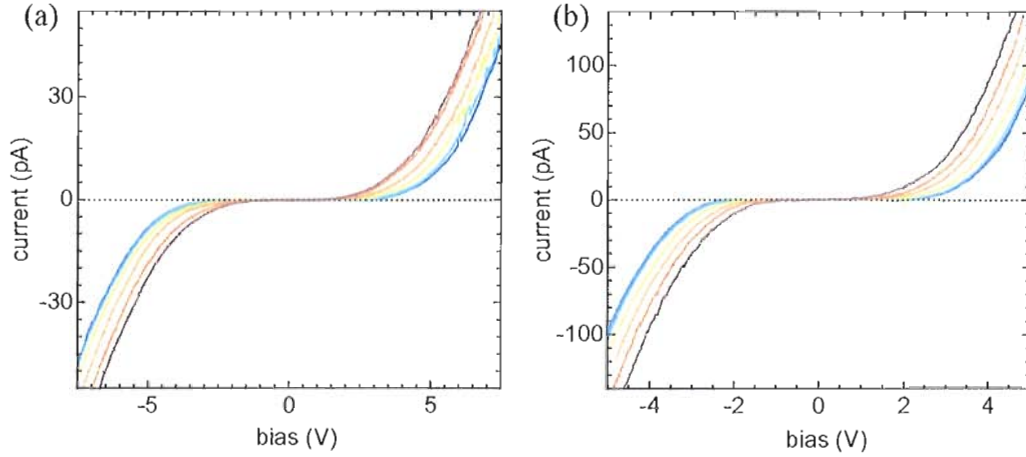
Figure 5.11. Current-voltage curves for the measured nanoparticle devices. I-V curves for devices #2 (a) and #3 (b) are shown for temperatures ranging from ≈ 240 mK to 80 K.

no current, and a post-experiment SEM inspection showed that no nanoparticle array bridged the gap. To ascertain the stability of the devices, and to compare to experimental and theoretical results in the literature (covered in the previous section), a series of I-V curves were measured as a function of temperature, 240 mK $< T \leq 80$ K.

The measured data for the #2 and #3 devices is shown in Figure 5.11, (a) and (b) respectively. Their appearance, in both cases, is consistent with theory and experiment describing arrays of tunnel junctions - a blockaded region, symmetric in voltage, where no current passes through the device followed by a power law rise in current after V_t is reached. The data has a noise level that is typically ± 0.2 pA, though this varies a little trace to trace. The maximum noise level was ± 0.4 pA,
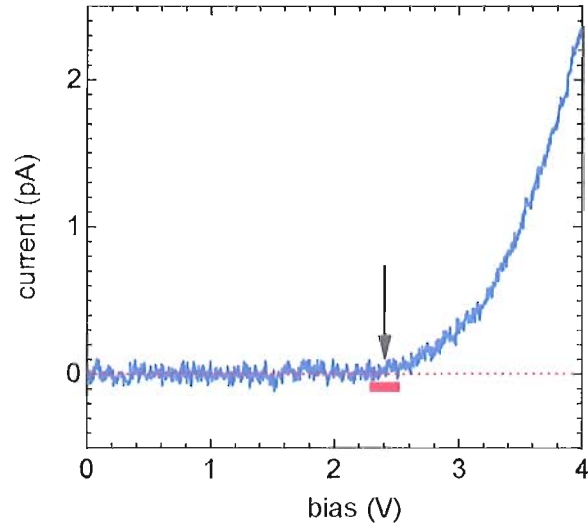
Figure 5.12. An example of the V_t extraction procedure. The arrow indicates the assigned V_t for this 240 mK data set. The red bar centered on the arrow's position indicates a conservative estimate of the error associated with the analysis.

and it went as low as ± 0.1 pA. Its magnitude does not correlate well with cryostat temperature. It may be a result of ground loop noise.

Current-Voltage Data Analysis

Two standard parameters of interest, the threshold voltage V_t and the power law exponent ζ were extracted from the I-V curves. V_t is determined systematically from inspection of the I-V data. An example illustrating this process is shown in Figure 5.12. Essentially, once the average current rises above zero and over the noise level of the data set, the threshold is said to be overcome. Another method, which involves plotting $I \times dV/dI$ vs. V and charting the V intercept [7], yields the same result within error.
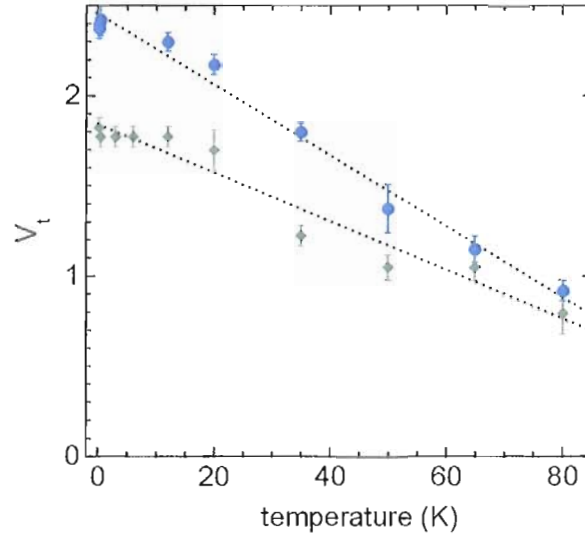
Figure 5.13. V_t vs. T for the nanoparticle devices. Device #2 corresponds to the upper data (blue), and device #3 is the lower data (green). Dotted lines are fits to each data set.

This procedure was applied to both the positive and negative bias halves of the curve. According to theory, the curves should be symmetric in voltage and thus symmetric in V_t. However, the values did differ slightly (approximately ± 0.05 V), which was factored into the final error estimate for V_t at each temperature. The complete results of the V_t analysis are shown in Figure 5.13. Qualitatively, the results look sensible - starting with some maximum value at low temperature, then falling off with increasing temperature.

Quantitatively, Equation 5.4 predicts a linear dependence between V_t and T. Fitting linear trends to the measured V_t values yields the dotted lines shown in Figure 5.13. If these are extrapolated up to ambient temperature, the expected temperature at which each device no longer exhibits Coulomb blockade is 125 K and

135 K for devices #2 and #3 respectively. This can be compared to a calculation of these temperatures from Equation 5.4. $P(0)$, the lattice geometry-dependent term, is determined from the ratio of the nanoparticle center-to-center spacing and nanoparticle radius, which $= 2.8$ for the average nanoparticle in our devices. This ratio informs the magnitude of the inter-nanoparticle capacitances. The percolation threshold, p_c, is known for 1D chains ($= 1$) and large 2D networks (dependent on lattice connectivity), but for objects with intermediate geometry like our devices, it must be calculated[8]. Device #2 has $p_c = 0.80$ and device #3 has $p_c = 0.65$, which reflect their relative narrowness, ≈ 4 particles vs. ≈ 7 particles respectively. Using these simple calculations, the predicted linear slopes coming down from $V_t(0)$ are $\approx 0.002(2)$ (device #2) and $0.002(7)$ (device #3), which translate into blockade disppearing at ~ 450 K (#2) and ~ 370 K (#3). This differs from the observed trends by a factor of ~ 3.

The correspondence between the model and the observed V_t behavior is clearly not very good, but it is important to note a few caveats in these calculations. The dielectric constant of the ligand shell is not known to high accuracy, which could affect the $P(0)$ calculation somewhat. The value used here is 3 after research on a similar ligand material [125]. Also, the percolation threshold is difficult to calculate accurately, because our nanoparticle arrays appear to have an amorphous

---

[8]These calculations were made using a custom Mathematica routine that allowed for lattices of arbitrary length and width. A fraction of sites were turned on randomly, and the lattice was checked for percolation. This was repeated for 2000 lattice instances for a particular fraction. This was repeated for 'filling' fractions 0.0 to 1.0, charting the probability of finding a percolating path vs. fraction filled. The the middle of the transition from probability 0 to 1 determines p_c.

lattice geometry, variable array width, and variable individual size. This makes percolation simulations, which depend strongly on the number of nearest neighbors in the lattice, imprecise. Along these same lines, the expression for P(0) assumes identical inter-nanoparticle capacitances on a fixed lattice. The nanoparticle's size variation, which approaches $\sim 30\%$, will make these capacitances vary significantly. Finally, the limited extent of these quasi-1D arrays makes them more susceptible to local variations in the background charge distribution, which the model takes as uniform.

Despite these complicating issues, the linear suppression of $V_t(T)$ is retained (Figure 5.13) in our observations, which suggests that the basis of the model is quite robust. Future calculations examining the effect of nanoparticle lattice and size perturbations ('amorphizing' the lattice) may result in better quantitative agreement with experiment for this device type.

Analysis of the power law exponent ζ is carried out as illustrated by Figure 5.14(a), fitting a line to a log-log plot of current vs. voltage. The voltage axis was re-scaled relative to the measured V_t to match the theoretical power law form (Equation 5.3). In the selected example, $V_t = 1.375$ (the average of the positive and negative V_t's). Note that the fit was made to those points above zero on the x-axis. Below that, the current through the device is above threshold, but is less than approximately
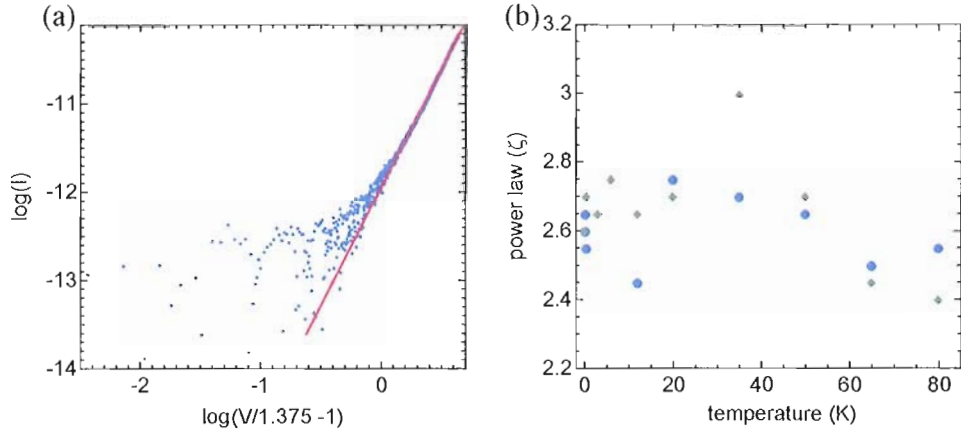
Figure 5.14. Power law exponent (ζ) analysis and T dependence for the measured nanoparticle devices. ζ is determined from the slope of the fit line in (a). ζ for devices #2 and #3 (blue and green symbols respectively) is plotted vs. temperature (b).

2 pA. Since the noise is then comparable to the signal magnitude, the data becomes somewhat unreliable for fitting purposes.

The spread in the measured ζ's (shown vs. temperature in Figure 5.14(b)) is significant - approximately equal to 0.3 for both devices with a couple of exceptional cases for the #3 device. Their values are also considerably higher than those predicted by [117] (1 and 5/3 for one and two dimensions respectively). However, they are well-aligned in both instances with the power law characteristics of similar experimental systems in the literature [7–9, 121]. All of these experiments find power laws in excess of the theoretical values for their system's dimensionality, though [121] do find a few of their carbon nanoparticle chains close to $\zeta = 1$.

The spread in power laws for the most directly comparable system [9], which studies strips of nanoparticles defined by EBL, is very close to what we observe. Additionally, other quasi-1D nanoparticle structures [121, 126] show evidence for even

greater variability. A plausible explanation for this phenomenon is the sensitivity the devices have to the local configuration of quenched background charges. The limited width of the nanoparticle arrays allows for only a few current-carrying pathways. A re-configuration of local fixed charges changes the energy thresholds for particles in the array, thus shifting the manner in which the array responds to increasing bias. For our devices, ζ has no apparent dependence on temperature, however the spread in the the base temperature data sets' ζ (see Figure 5.14(b)) suggests a temporal and/or temperature dependence for the re-configuration of background charges. Further experiments would be required to determine which (time or temperature) is the dominant effect for our devices.

Other Points of Interest

An obvious concern with these novel devices is how stable they are. Unlike, for instance, the semiconductor electron billiards, these devices are not encapsulated. They sit directly on the surface of the wafer, and are at least briefly exposed to atmosphere before insertion into the cryostat. These exposures could translate into device volatility, especially given the partially organic nature of the device structure. While there are many aspects to stability, and thus many ways of characterizing it, we have taken a first step by charting these devices' stability with regards to the duration of the experiment. Figure 5.15 shows base temperature I-V curves for each device before and after raising the devices up to 80 K for the temperature
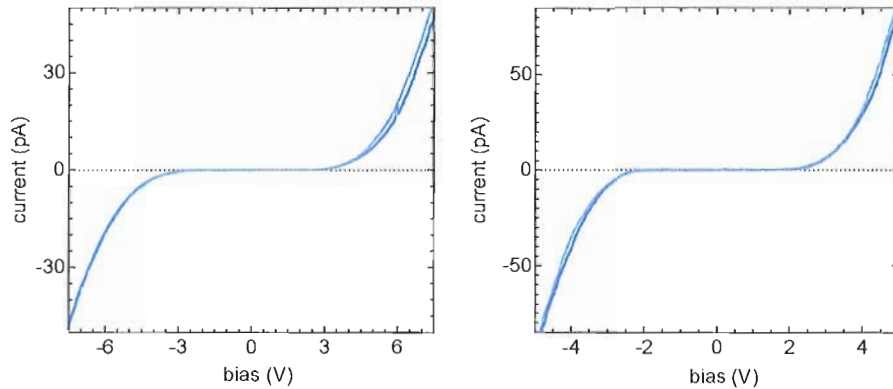
Figure 5.15. Two current-voltage curves at base temperature for each device, separated by ≈ 1 week and a slow temperature cycle up to 80 K. Device #2 and #3 correspond to (a) and (b) respectively.

dependent measurements, which corresponds to a temporal separation of ≈ 1 week. The differences between the two curves are small in both cases, indicating that at least in response to the noted stimuli, the devices are reasonably stable.

An interesting point can be observed in positive bias side of device #2's curves. There is a small jump in the bottom curve at ≈ 6 V that takes it briefly up to the level of the top curve before reverting to its previous behavior. A closer look at this occurrence is shown in Figure 5.16(a). This is interesting, because while the bottom curve has switched upwards, it appears to follow the top curve's power law. This switching behavior is prevalent in device #2 data sets up to and including the 35 K trace (Figure 5.16(b)).

The intervals of 'on' and 'off' appear random, though the jump height in current ≈ 2 pA in all cases. It is difficult to draw any good conclusions from this limited set of observations, however we speculate that the current carrying pathway through
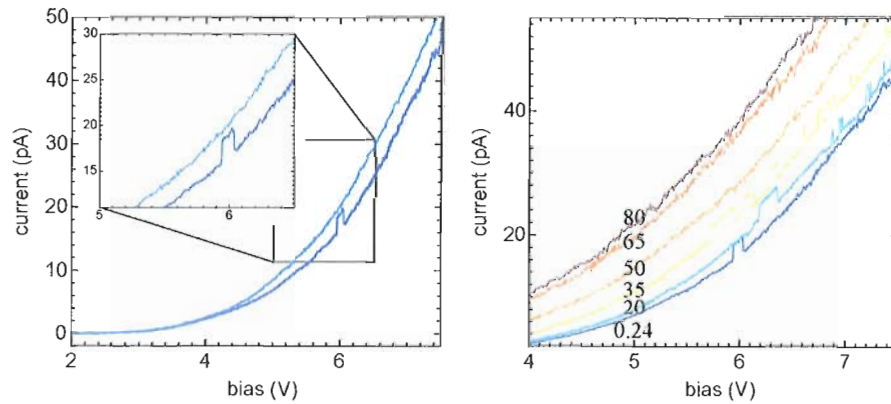
Figure 5.16. 'Switching' behavior in nanoparticle device #2. A comparison of base temperature data sets shows a single feature (a), but the switching behavior is apparent in data sets below 50 K (b). The numbering on the righthand graph indicates the cryostat temperature for each I-V curve.

the nanoparticle array is switching between two routes that are energetically nearly the same. The switching between them could occur due to charging/discharging of a nanoparticle or quenched substrate charging site near the pathway, which would minutely shift the energy of one path vs. the other. In this scenario, raising the temperature would eventually make the two routes effectively identical, suppressing the switching behavior. This is consistent with our observations. Similar telegraph-like switching was observed as a function of time at fixed bias in [9], also with quasi-1D chains of nanoparticles. They offer a similar explanation for their origin.

Future Experiments

The experiments and current-voltage curve analysis presented in this chapter show good correspondence with existing theoretical models and experimental results from analogous devices. It would be a mistake, however, to say that this novel class of nanoparticle devices is well-understood overall. For instance, the device finishing step remains a very sensitive process, as evidenced by the limited number of devices measured in our experiments. There are also basic questions regarding the extent of device-to-device variability, device stability under temperature and bias cycling, and the effects of nanoparticle size variation that remain unanswered. Further study along the lines set out in this chapter should bring answers to some of these and inform refinements in our fabrication process, perhaps allowing us to achieve truly one-dimensional nanoparticle arrays.

More ambitious are experiments based on the original intent of this project, to observe phase-coherent electron interference through a many element (nanoparticle) array. Rough calculations (see the introduction for this chapter) suggest that electron phase coherence lengths should be well in excess of the nanoparticle array length ($l_\phi \sim 5~\mu m \gg 200$ nm), and that the λ_F to nanoparticle size ratio is similar to that of the electron billiards, nominally placing carriers in the 'semiclassical' regime[9] of transport when moving within each nanoparticle.

---

[9]The electron billiards of Chapter III operate in this regime. In short, because λ_F is only a fraction of the device size, the dynamics of carriers at E_F can be modeled classically, but must obey quantum-mechanical Fermi-Dirac statistics.

Taking these calculations as motivation, a relatively simple experiment would be to move the nanoparticle array off-blockade and proceed similarly to the electron billiards - applying a varying magnetic field while monitoring current through the device - with the goal of observing MCF. This is certainly worth an attempt (because of its simplicity), but there are issues with this straightforward approach. The first is detection of the MCF. Even well beyond V_t, the resistance of these nanoparticle arrays is on the order of GΩ, which precludes standard AC lock-in detection. Also, the amplitude of MCF due to quantum interference is limited theoretically to e^2/h or ≈ 25 kΩ, making the fluctuations a 1 part in 100,000 modulation on the measured current. This is approximately an order of magnitude below the measurement circuit's best detection limit.

Outside of this considerable technical challenge, there is a variety of physical differences from the electron billiard system that may prove to be important in observing phase coherent phenomena. Even in the off-blockade regime there is still a tunnel barrier between each island. Electrons can still move coherently through the array via elastic tunneling from one island to the next, but the transmission probability for any one tunneling 'attempt' may be very low. Depending on the number of reflections the electron endures within each island before moving on to the next, its total path length may exceed l_ϕ before traversing the array.

A more crucial practical consideration is the magnetic field required to place a nanoparticle into the MCF field regime. According to semiclassical theory, no

experimentally accessible field will be able to remove the nanoparticles from the weak localization field regime, $0 < B < \Phi_0/A_{dot}$ or $0 < B \lesssim 400$ T(!), which means MCF may be completely suppressed.

The issues with observing MCF in the nanoparticle arrays are not limited to those discussed here, but these should convey the significant challenges that remain in realizing the original intent of this research project. A more modest and experimentally realizable goal for these arrays may be to modify the devices such that a gate could be positioned near each one. This would be only a small change of the lithographic processes detailed earlier in the chapter, and would allow electrostatic tuning of the nanoparticles' energy spectra[10] with potentially interesting results [129].

Finally, in a direction that broadly complements the research presented in Chapter IV, the DNA/nanoparticle system could be deposited between contacts without the molecular combing step. Doing this with higher concentrations of DNA and larger electrode gaps may allow the deposition of disordered nanoparticle networks which may have a fractal geometry[11] as shown schematically in Figure 5.17(b). Because transport in tunnel junction systems is strongly dependent on their

---

[10]A single nanoparticle has average energy level spacings $\approx \dfrac{2\pi^2\hbar^2}{m^* k_F r^3} \approx 23$ meV neglecting electron-electron interactions and using $m^* = m_0$ [127, 128]. This is well in excess of $k_B T$ at cryogenic temperatures.

[11]This is based on a fractal analysis of the AFM image in [125] of gold nanoparticle/poly-L-lysine fractured films, and research on the 2D packing statistics of DNA molecules [130]
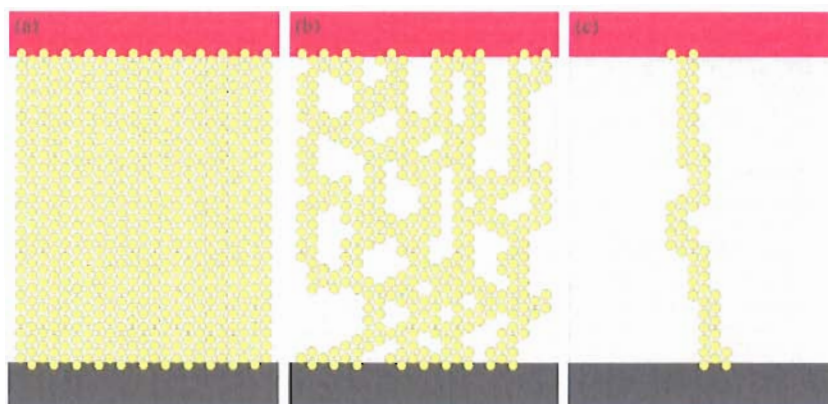
Figure 5.17. Nanoparticle networks of differing dimension. The 2 (a) and quasi-1 (c) dimensional networks

dimensionality [117], devices with a fractional dimension should exhibit behaviors

distinct from one (Figure 5.17(c)) and two dimensional (Figure 5.17(a)) systems.

APPENDIX

CIRCUIT SIMULATIONS USING MODIFIED NODAL ANALYSIS

The electrical simulations in Chapter IV were completed using a technique called "modified nodal analysis" (MNA), which is a commonly used and flexible circuit analysis method [94]. The described implementation takes a 4-color image as input and computes the resistance of the 'circuit' that corresponds to the image's pixel arrangement. This Appendix offers a more detailed look at the method and programming that goes into these simulations.

At its heart, MNA is simply the usual Kirchoff's rule circuit analysis modified to systematically produce a matrix of equations that is more easily solved by computer than by hand. This is pointless for small circuits, but is required for circuits of the size considered in Chapter IV ($\sim 10^3 \rightarrow 10^6$ nodes per circuit). The analysis technique was advanced in 1974 to eliminate some of the disadvantages of (unmodified) node analysis, which included the inability to process voltage sources and current-dependent circuit elements in a time efficient manner [131]. It was subsequently integrated into SPICE2 (Simulation Program with Integrated Circuit Emphasis 2), which went on to become the de facto standard circuit simulator for the integrated circuit industry for a time, and is still used widely today.

For the simulations in this dissertation, MNA is used to solve for the DC electrical characteristics of large resistor networks. Using a custom-written Mathematica routine, a 'circuit' is input in the form of a 4-color (black, white, red, and green) image, translated into a matrix of circuit equations, and solved for the voltages at each node (pixel) and the currents going into each drain node. Figures 4.5 and 4.6 and the surrounding text describe the process of translating a circuit into the corresponding matrix of equations. For completeness, Figure A.1 shows the process start-to-end for a small circuit with 6 nodes. Each pixel translates to a node (Figure A.1(b)), which is in turn translated into a matrix row that contains the node's current junction rule equation (Figure A.1(c)). Note that the color of each pixel signals how to connect it to its neighbors, not what type of circuit element to place in its position. The rules implemented here are: a white pixel accepts no electrical connections, a black pixel connects to any non-white pixels with a resistor, a green pixel has a connection to ground, and a red pixel has a connection to a DC voltage source. The present implementation also uses a constant voltage at all source (red) pixels, a fixed value resistor between each connected node ($R_1 = R_2 = R_3 = ...$), and nearest neighbor connections only.

This procedure produces the $(n+m) \times (n+m)$ matrix in Figure A.1(c), which has a size dictated by the number of nodes (n) and the number of source pixels (m), and consists only of known quantities. The upper left $n \times n$ matrix contains the passive electrical elements' information (i.e. no voltage sources, etc.). Elements connected to

(a)

(b)

(c)

The matrix equation:

	a	b	c	d	e	f	source
a	$\frac{1}{R_1}+\frac{1}{R_2}$	$\frac{-1}{R_1}$	$\frac{-1}{R_2}$	0	0	0	0
b	$\frac{-1}{R_1}$	$\frac{1}{R_1}+\frac{1}{R_4}$	0	$\frac{-1}{R_4}$	0	0	1
c	$\frac{-1}{R_2}$	0	$\frac{1}{R_2}+\frac{1}{R_3}$	$\frac{-1}{R_3}$	0	0	0
d	0	$\frac{-1}{R_4}$	$\frac{-1}{R_3}$	$\frac{1}{R_3}+\frac{1}{R_4}+\frac{1}{R_5}$	0	0	0
e	0	0	0	0	0	0	0
f	0	0	0	0	0	0	0
source	0	1	0	0	0	0	0

$$\begin{bmatrix} v_a \\ v_b \nearrow^V \\ v_c \\ v_d \\ v_e \nearrow^0 \\ v_f \nearrow^0 \\ I \end{bmatrix} = \begin{bmatrix} 0 \\ 0 \\ 0 \\ 0 \\ 0 \\ 0 \\ V \end{bmatrix}$$
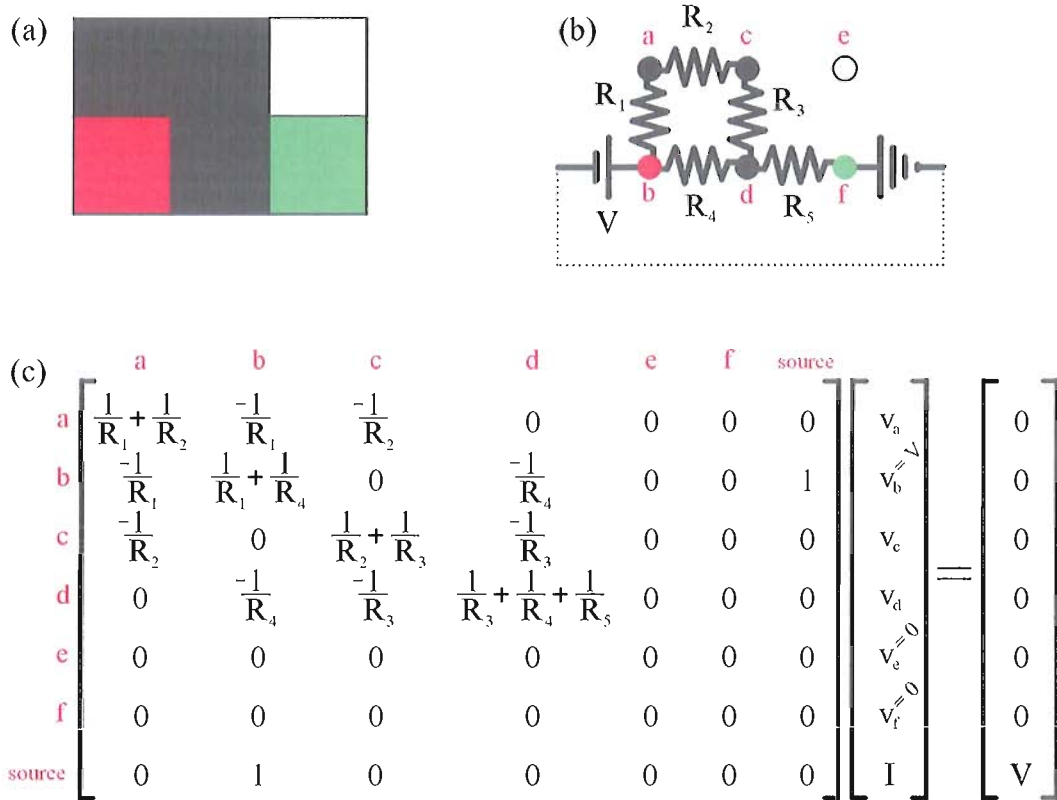
Figure A.1. The complete MNA program process showing a simple image (a), its translation into a resistor network (b), and the linear set of equations that describe that resistor network (c).

ground appear only on the diagonal, while others appear in both the diagonal and off-diagonal positions. The remainder of the matrix indicates node connections to voltage sources. For an example, take row b in Figure A.1. Its current junction is:

$$-I + \frac{V - v_a}{R_1} + \frac{V - v_d}{R_4} = 0 \qquad (A.1)$$

where I equals the total current in the circuit, and v_b has been replaced by V of the voltage source. After separating out the unknown quantities (v_d, I) into the
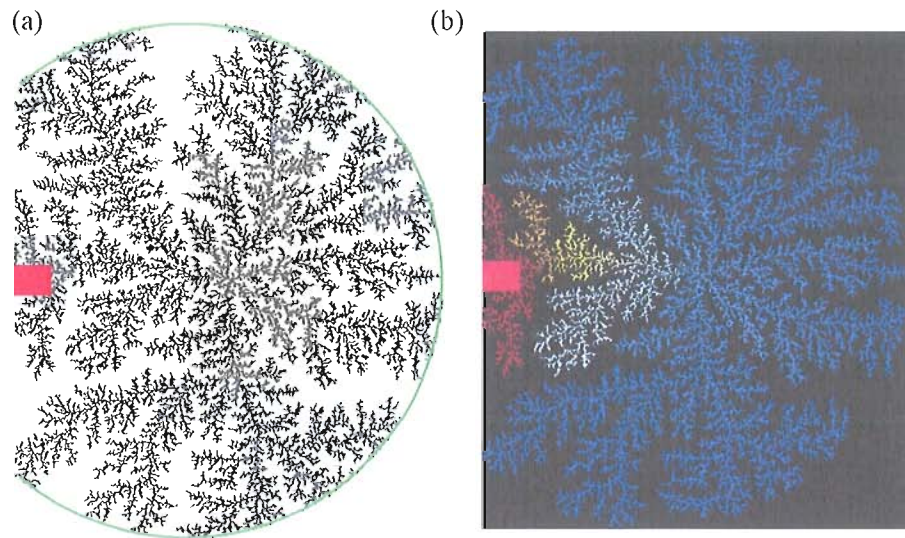
Figure A.2. A sample large scale simulation (a) and its voltage map (b). The color gradient in (b) ranges from red to blue, which represent the source voltage V and $V = 0$ respectively. See Chapter IV for a further explanation of the resistor network in (b).

vector multiplying the matrix and the known quantities (sum of current flows = 0) into the righthand vector, the correspondence of row b to Equation A.1 is clear.

Solving this linear set of equations gives the voltage at every node as well as the total current in the circuit. This last quantity allows the resistance of the circuit to be calculated. The voltage information can allow an intuitive grasp of the current flow patterns in the devices (see Figure A.2 for an example), and may have more direct uses in future applications of this technique.

Finally, MNA and this implementation are extensible. MNA can handle simulations of AC circuit characteristics by using the complex impedances Z of whatever elements are included [94, 131]. For our program, AC circuit implementation would require a different set of translation rules from pixel to circuit element, but in principle could

represent any type of reactive circuit element. For instance, the white pixel translation rule could connect any white node to adjacent nodes via a capacitor, which would produce a more realistic AC response than the present rule. A concern with added translation rules is the size of the resultant matrix of equations and hence computation time. The present white pixel rule produces a significant number of zero columns and rows, which quickly drop out of the calculation. The new rule (just discussed) would put an equation in every row, adding significant computational complexity. For this reason, any rule modifications may further limit the size of the images that can be used.

BIBLIOGRAPHY

[1] B. B. Mandelbrot, *The Fractal Geometry of Nature* (W. H. Freeman, 1982).

[2] M. F. Barnsley, *Fractals Everywhere* (Academic Press, 1993), 2nd ed.

[3] C. A. Marlow, R. P. Taylor, T. P. Martin, B. C. Scannell, H. Linke, M. S. Fairbanks, G. D. R. Hall, I. Shorubalko, L. Samuelson, T. M. Fromhold, et al., Physical Review B **73**, 195318 (2006).

[4] A. P. Micolich, R. P. Taylor, T. P. Martin, R. Newbury, T. M. Fromhold, A. G. Davies, H. Linke, W. R. Tribe, L. D. Macks, C. G. Smith, et al., Physical Review B **70**, 085302 (2004).

[5] B. C. Scannell, R. P. Taylor, M. S. Fairbanks, C. A. Marlow, and H. Linke, submitted to PRL (2010).

[6] R. Ketzmerick, Physical Review B **54**, 10841 (1996).

[7] M. G. Ancona, S. E. Kooi, W. Kruppa, A. W. Snow, E. E. Foos, L. J. Whitman, D. Park, and L. Shirey, Nano Letters **3**, 135 (2003).

[8] R. Parthasarathy, X.-M. Lin, K. Elteto, T. F. Rosenbaum, and H. M. Jaeger, Physical Review Letters **92**, 076801 (2004).

[9] K. Elteto, X.-M. Lin, and H. M. Jaeger, Physical Review B **71**, 205412 (2005).

[10] M. M. Fogler, S. V. Malinin, and T. Nattermann, Physical Review Letters **97**, 096601 (2006).

[11] L. W. Shubnikov and W. J. de Haas, Proceedings of the Royal Netherlands Academy of Arts and Sciences **33**, 130 (1930).

[12] L. J. van der Pauw, Philips Research Reports **13**, 1 (1958).

[13] R. H. Blick, D. Pfannkuche, R. J. Haug, K. v. Klitzing, and K. Eberl, Physical Review Letters **80**, 4032 (1998).

[14] E. A. Laird, J. R. Petta, A. C. Johnson, C. M. Marcus, A. Yacoby, M. P. Hanson, and A. C. Gossard, Physical Review Letters **97**, 056801 (2006).

[15] A. Bertoni, P. Bordone, R. Brunetti, C. Jacoboni, and S. Reggiani, Physical Review Letters **84**, 5912 (2000).

[16] P. Zanardi and F. Rossi, Physical Review Letters **81**, 4752 (1998).

[17] J. M. Taylor, J. R. Petta, A. C. Johnson, A. Yacoby, C. M. Marcus, and M. D. Lukin, Physical Review B **76**, 035315 (2007).

[18] T. H. Oosterkamp, T. Fujisawa, W. G. van der Wiel, K. Ishibashi, R. V. Hijman, S. Tarucha, and L. P. Kouwenhoven, Nature **395**, 873 (1998).

[19] D. S. Duncan, M. A. Topinka, R. M. Westervelt, K. D. Maranowski, and A. C. Gossard, Physical Review B **63**, 045311 (2001).

[20] F. R. Waugh, M. J. Berry, D. J. Mar, R. M. Westervelt, K. L. Campman, and A. C. Gossard, Physical Review Letters **75**, 705 (1995).

[21] D. T. McClure, L. DiCarlo, Y. Zhang, H.-A. Engel, C. M. Marcus, M. P. Hanson, and A. C. Gossard, Physical Review Letters **98**, 056801 (2007).

[22] W. G. van der Wiel, S. De Franceschi, J. M. Elzerman, T. Fujisawa, S. Tarucha, and L. P. Kouwenhoven, Reviews of Modern Physics **75**, 1 (2003).

[23] C. A. Marlow, R. P. Taylor, M. Fairbanks, I. Shorubalko, and H. Linke, Physical Review Letters **96**, 116801 (2006).

[24] M. Elhassan, J. P. Bird, A. Shailos, C. Prasad, R. Akis, D. K. Ferry, Y. Takagaki, L. H. Lin, N. Aoki, Y. Ochiai, et al., Physical Review B **64**, 085325 (2001).

[25] N. Aoki, D. Oonishi, Y. Iwase, Y. Ochiai, K. Ishibashi, Y. Aoyagi, and J. Bird, Applied Physics Letters **80**, 2970 (2002).

[26] I. V. Zozoulenko, A. S. Sachrajda, G. C., K.-F. Berggren, P. Zawadski, Y. Feng, and Z. Wasilewski, Physical Review Letters **83**, 1838 (1999).

[27] P. Ramvall, N. Carlsson, I. Maximov, P. Omling, L. Samuelson, W. Seifert, Q. Wang, and S. Lourdudoss, Applied Physics Letters **71**, 918 (1997).

[28] B. Hackens, S. Faniel, C. Gustin, X. Wallart, S. Bollaert, A. Cappy, and V. Bayot, Physical Review Letters **94**, 146802 (2005).

[29] C. W. J. Beenakker and H. van Houten, Solid State Physics **44**, 1 (1991).

[30] C. W. J. Beenakker, Reviews of Modern Physics **69**, 731 (1997).

[31] Y. Alhassid, Reviews of Modern Physics **72**, 895 (2000).

[32] J. H. Davies, *The Physics of Low-Dimensional Semiconductors* (Cambridge University Press, 1998), 1st ed.

[33] J. P. Bird, *Electron transport in quantum dots* (Kluwer Academic Publishers, 2003), 1st ed.

[34] T. Heinzel, *Mesoscopic Electronics in Solid State Nanostructures* (Wiley-Verlag GmbH and Co., 2007), 2nd ed.

[35] W. T. Sommer, Physical Review Letters **12**, 271 (1964).

[36] T. Ando, A. B. Fowler, and F. Stern, Reviews of Modern Physics **54**, 437 (1982).

[37] R. Dingle, H. L. Stoermer, A. C. Gossard, and W. Wiegman, Applied Physics Letters **33**, 665 (1978).

[38] H. Hardtdegen, R. Meyer, M. Hollfelder, T. Schäpers, J. Appenzeller, H. Loken-Larsen, T. Klocke, C. Dieker, B. Lengeler, H. Lüth, et al., Journal of Applied Physics **73**, 4489 (1993).

[39] P. Ramvall, N. Carlsson, P. Omling, L. Samuelson, W. Seifert, Q. Wang, K. Ishibashi, and Y. Aoyagi, Journal of Applied Physics **84**, 2112 (1998).

[40] O. Bohigas, M. J. Giannoni, and C. Schmit, Physical Review Letters **52**, 1 (1984).

[41] M. Büttiker, Physical Review Letters **57**, 1761 (1986).

[42] Y. Aharonov and D. Bohm, Physical Review **115**, 485 (1959).

[43] R. P. Taylor, R. Newbery, A. S. Sachrajda, Y. Feng, P. T. Coleridge, C. Dettmann, N. Zhu, H. Guo, A. Delage, P. J. Kelly, et al., Physical Review Letters **78**, 1952 (1997).

[44] A. P. Micolich, R. P. Taylor, A. G. Davies, J. P. Bird, R. Newbury, T. M. Fromhold, A. Ehlert, H. Linke, L. D. Macks, W. R. Tribe, et al., Physical Review Letters **87**, 036802 (2001).

[45] A. G. Huibers, M. Switkes, C. M. Marcus, K. Campman, and A. C. Gossard, Physical Review Letters **81**, 200 (1998).

[46] J. P. Bird, K. Ishibashi, D. Ferry, Y. Ochiai, Y. Aoyagi, and T. Sugano, Physical Review B **51**, 18037 (1995).

[47] J. P. Bird, R. Akis, D. K. Ferry, A. P. S. de Moura, Y.-C. Lai, and K. M. Indlekofer, Reports on Progress in Physics **66**, 583 (2003).

[48] P. A. Lee and A. D. Stone, Physical Review Letters **55**, 1622 (1985).

[49] P. A. Lee, A. D. Stone, and H. Fukuyama, Physical Review B **35**, 1039 (1987).

[50] J. Hajdu and G. Landwehr, in *Strong and Ultrastrong Magnetic Fields and Their Applications*, edited by F. Herlach (Springer-Verlag, Heidelberg, 1985).

[51] E. P. Wigner, in *Proceedings of the Canadian Mathematical Congress* (University of Toronto, 1957).

[52] F. J. Dyson, Journal of Mathematical Physics (N.Y.) **3**, 140 (1962).

[53] B. L. Altschuler and B. I. Shklovskii, Soviet Physics JETP **64**, 127 (1986).

[54] P. W. Brouwer and C. W. J. Beenakker, Physical Review B **55**, 4695 (1997).

[55] P. W. Brouwer, J. N. H. J. Cremers, and B. I. Halperin, Physical Review B **65**, 081302(R) (2002).

[56] B. Hackens, J. P. Minet, S. Faniel, G. Farhi, C. Gustin, J. P. Issi, J. P. Heremans, and V. Bayot, Physical Review B **67**, 121403(R) (2003).

[57] C. A. Marlow, Ph.D. thesis, University of Oregon, Eugene, Oregon (2005).

[58] C. M. Marcus, R. M. Westervelt, P. F. Hopkins, and A. C. Gossard, Physical Review B **48**, 2460 (1993).

[59] H. U. Baranger, R. A. Jalabert, and A. D. Stone, Physical Review Letters **70**, 3876 (1993).

[60] T. P. Martin, C. A. Marlow, L. Samuelson, A. R. Hamilton, H. Linke, and R. P. Taylor, Physical Review B **77**, 155309 (2008).

[61] M. Elhassan, J. P. Bird, R. Akis, D. K. Ferry, T. Ida, and K. Ishibashi, Journal of Physics: Condensed Matter **17**, L351 (2005).

[62] R. P. Taylor, M. L. Leadbeater, G. P. Whittington, P. C. Main, L. Eaves, S. P. Beaumont, I. McIntyre, S. Thoms, and C. D. W. Wilkinson, Surface Science **196**, 52 (1988).

[63] B. Mandlebrot, Science **156**, 636 (1967).

[64] S. Lovejoy, Science **216**, 185 (1982).

[65] P. J. E. Peebles, Physica D **38**, 273 (1989).

[66] F. Caserta, H. E. Stanley, W. D. Eldred, G. Daccord, R. E. Hausman, and J. Nittman, Physical Review Letters **64**, 95 (1990).

[67] Y.-J. Bao, B. Zhang, Z. Wu, J.-W. Si, M. Wang, R.-W. Peng, X. Lu, J. Shao, Z.-F. Li, X.-P. Hao, et al., Applied Physics Letters **90**, 251914 (2007).

[68] F. Carlier and V. M. Akulin, Physical Review B **69**, 115433 (2004).

[69] R. Burioni, D. Cassi, and F. M. Neri, Journal of Physics A: Mathematical and General **37**, 8823 (2004).

[70] H. Samavati, A. Hajimiri, A. R. Shahani, G. N. Nasserbakht, and T. H. Lee, IEEE Journal of Solid State Circuits **33**, 2035 (1998).

[71] N. L. Cohen, Communications Quarterly **1995**, 9 (1995).

[72] T. A. Witten and L. M. Sander, Physical Review B **27**, 5686 (1983).

[73] M. F. Barnsley, R. L. Devaney, B. B. Mandebrot, H.-O. Peitgen, D. Saupe, and R. F. Voss, *The Science of Fractal Images* (Springer-Verlag, 1988).

[74] K. J. Falconer, *Techniques in Fractal Geometry* (Wiley, 1997), 1st ed.

[75] M. V. Berry and Z. F. Lewis, Proceedings of the Royal Society London: A **370**, 459 (1980).

[76] B. Dubuc, J. F. Quiniou, C. Roques-Carmes, C. Tricot, and S. W. Zucker, Phys. Rev. A **39**, 1500 (1989).

[77] J.-F. Gouyet, *Physics and Fractal Structures* (Springer-Verlag, 1996), chap. 1, 1st ed.

[78] T. Vicsek, F. Family, and P. Meakin, Europhysics Letters **12**, 217 (1990).

[79] L. Bardotti, P. Jensen, A. Hoareau, M. Treilleux, and B. Cabaud, Physical Reviews Letters **74**, 4694 (1995).

[80] C. Brechignac, P. Cahuzac, F. Carlier, C. Colliex, J. Leroux, A. Masson, B. Yoon, and U. Landman, Physical Review Letters **88**, 196103 (2002).

[81] I. Webman, Physical Review Letters **47**, 1496 (1981).

[82] Y. Gefen, A. Aharony, and S. Alexander, Physical Review Letters **50**, 77 (1983).

[83] M. B. Isichenko, Reviews of Modern Physics **64**, 961 (1992).

[84] S. Redner, *Fractal and multifractal scaling of electrical conduction in random resistor networks*, arXiv:0710.1105.

[85] M. Ben-Chorin, F. Möller, F. Koch, W. Schirmacher, and M. Eberhard, Physical Review B **51**, 2199 (1995).

[86] J. C. Dyre and T. B. Schrøder, Reviews of Modern Physics **72**, 873 (2000).

[87] Y.-J. Bao, H.-M. Li, X.-C. Chen, R.-W. Peng, M. Wang, X. Lu, J. Shao, and N.-B. Ming, Applied Physics Letters **92**, 151902 (2008).

[88] W. Wen, L. Zhou, B. Hou, C. T. Tran, and P. Sheng, Physical Review B **72**, 153406 (2005).

[89] W. Wen, Z. Yang, G. Xu, Y. Chen, L. Zhou, W. Ge, C. T. Chan, and P. Sheng, Applied Physics Letters **83**, 2106 (2003).

[90] S. Havlin and D. Ben-Avraham, Advances in Physics **36**, 695 (1987).

[91] J. P. Clerc, G. Giraud, J. M. Laugier, and J. M. Luck, Advances in Physics **39**, 191 (1990).

[92] T. C. Haba, G. Ablart, T. Camps, and F. Olivie, Chaos, Solitons, and Fractals **24**, 479 (2005).

[93] B. Doucot, W. Wang, J. Chaussy, B. Pannetier, R. Rammal, A. Vareille, and D. Henry, Physical Review Letters **57**, 1235 (1986).

[94] R. A. DeCarlo and P.-M. Lin, *Linear Circuit Analysis: Time Domain, Phasor, and Laplace Transform Approaches* (Oxford University Press, 2001).

[95] J.-P. Allouche and J. Shallit, *Automatic sequences: theory, applications, generalizations* (Cambridge University Press, 2003), chap. 30 - 32.

[96] A. Lando, N. Kebaili, P. Cahuzac, A. Masson, and C. Brechignac, Physical Review Letters **97**, 133402 (2006).

[97] F. Carlier, S. Benrezzak, P. Cahuzac, N. Kebaili, A. Masson, A. K. Srivastava, C. Colliex, and C. Brechignac, Nano Letters **6**, 1875 (2006).

[98] P. Jensen, Reviews of Modern Physics **71**, 1695 (1999).

[99] S. A. Scott and S. A. Brown, The European Physics Journal D **39**, 433 (2006).

[100] D. N. McCarthy, Ph.D. thesis, University of Canterbury, Christchurch, New Zealand (2008).

[101] S. Glasstone, K. J. Laidler, and H. Eyring, *The Theory of Rate Processes* (McGraw-Hill, 1941), 1st ed.

[102] D. Avnir, O. Biham, D. Lidar, and O. Malcai, Science **279**, 39 (1998).

[103] B. B. Mandlebrot, Science **279**, 783 (1998).

[104] Z. Zhang, X. Chen, and M. G. Lagally, Physical Review Letters **73**, 1829 (1994).

[105] P. Melinon, A. Hannour, L. Bardotti, B. Prevel, J. Gierak, E. Bourhis, G. Faini, and B. Canut, Nanotechnology **19**, 235305 (2008).

[106] P. A. Campbell, L. J. Sinnamon, C. E. Thompson, and D. G. Walmsley, Surface Science **410**, L768 (1998).

[107] N. Vandamme, E. Janssens, F. Vanhoutte, P. Lievens, and C. V. Haesendonck, J. Phys. Cond. Mat. **15**, S2983 (2003).

[108] S. Friedrichowski and G. Dumpich, Physical Review B **58**, 9689 (1998).

[109] V. Chandrasekhar, R. A. Webb, M. J. Brady, M. B. Ketchen, W. J. Gallagher, and A. Kleinsasser, Physical Review Letters **67**, 3578 (1991).

[110] M. A. Kastner, Reviews of Modern Physics **64**, 849 (1992).

[111] H. Grabert and M. H. Devoret, *Single Charge Tunneling: Coulomb phenomena in nanostructures*, vol. 294 of *NATO ASI Series* (Plenum Press, 1992), 1st ed.

[112] H. van Houten and C. W. J. Beenakker, Physical Review Letters **63**, 1893 (1989).

[113] M. G. Warner and J. E. Hutchison, Nature Materials **2**, 272 (2003).

[114] G. J. Kearns, E. W. Foster, and J. E. Hutchison, Analytical Chemistry **78**, 298 (2006).

[115] U. Geigenmueller and G. Schoen, Europhysics Letters **10**, 765 (1989).

[116] L. J. Geerligs, V. F. Anderegg, C. A. van der Jeugd, J. Romijn, and J. E. Mooij, Europhysics Letters **10**, 79 (1989).

[117] A. A. Middleton and N. S. Wingreen, Physical Review Letters **71**, 3198 (1993).

[118] M. Kardar, G. Parisi, and Y.-C. Zhang, Physical Review Letters **56**, 889 (1986).

[119] K. Elteto, E. G. Antonyan, T. T. Nguyen, and H. M. Jaeger, Physical Review B **71**, 064206 (2005).

[120] M. G. Ancona, W. Kruppa, R. W. Rendell, A. W. Snow, D. Park, and J. B. Boos, Physical Review B **64**, 033408 (2001).

[121] A. Bezryadin, R. M. Westervelt, and M. Tinkham, Applied Physics Letters **74**, 2699 (1999).

[122] G. J. Kearns, Ph.D. thesis, University of Oregon, Eugene, Oregon (2007).

[123] J. Fink, C. J. Kelly, D. Bethell, and D. J. Schiffrin, Chemistry of Materials **10**, 922 (1998).

[124] M. G. Warner, S. M. Reed, and J. E. Hutchison, Chemistry of Materials **12**, 3316 (2000).

[125] C. A. Berven, L. Clarke, J. L. Mooster, M. N. Wybourne, and J. E. Hutchison, Advanced Materials **13** (2001).

[126] L. Clarke, M. N. Wybourne, M. Yan, S. X. Cai, and J. F. W. Keana, Applied Physics Letters **71**, 617 (1997).

[127] N. W. Ashcroft and N. D. Mermin, *Solid State Physics* (Thomson Learning, Inc., 1976), chap. 2, pp. 38 – 44.

[128] D. C. Ralph, C. T. Black, and M. Tinkham, Physical Review Letters **74**, 3241 (1995).

[129] L. S. Kuzmin, P. Delsing, T. Claeson, and K. K. Likharev, Physical Review Letters **62**, 2539 (1989).

[130] B. Maier and J. O. Rädler, Physical Review Letters **82**, 1911 (1999).

[131] C.-W. Ho, A. Ruehli, and P. Brennan, IEEE Transactions on Circuits and Systems **22**, 504 (1975).